QUANTITATIVE SEISMIC INTERPRETATION AND RESERVOIR CHARACTERIZATION OF AKÇAKOCA PRODUCTION FIELD AT WESTERN BLACK SEA, TURKEY

A THESIS SUBMITTED TO
THE GRADUATE SCHOOL OF NATURAL AND APPLIED SCIENCES
OF
MIDDLE EAST TECHNICAL UNIVERSITY

BY

SUAT AKTEPE

IN PARTIAL FULFILLMENT OF THE REQUIREMENTS
FOR
THE DEGREE OF DOCTOR OF PHILOSOPHY
IN
GEOLOGICAL ENGINEERING

JUNE 2015

Approval of the thesis:

QUANTITATIVE SEISMIC INTERPRETATION AND RESERVOIR CHARACTERIZATION OF AKÇAKOCA PRODUCTION FIELD AT WESTERN BLACK SEA, TURKEY

submitted by **SUAT AKTEPE** in partial fulfillment of the requirements for the degree of **Doctor of Philosophy in Geological Engineering Department, Middle East Technical University** by,

Prof. Dr. Gülbin Dural Ünver
Dean, Graduate School of **Natural and Applied Sciences, METU** _____

Prof. Dr. Erdin Bozkurt
Head of Department, **Geological Engineering Dept., METU** _____

Prof. Dr. Nurkan Karahanoğlu
Supervisor, **Geological Engineering Dept., METU** _____

Assist. Prof. Dr. Atilla Arda Özacar
Co-supervisor, **Geological Engineering Dept., METU** _____

Examining Committee Members:

Prof. Dr. Nurkan Karahanoğlu
Geological Engineering Dept., METU _____

Prof. Dr. Serhat Akın
Petroleum and Natural Gas Engineering Dept., METU _____

Prof. Dr. Nuretdin Kaymakçı
Geological Engineering Dept., METU _____

Prof. Dr. Ahmet Tuğrul Başokur
Geophysical Engineering Dept., AÜ _____

Prof. Dr. Selma Kadıoğlu
Geophysical Engineering Dept., AÜ _____

Date: **26.06.2015**

I hereby declare that all information in this document has been obtained and presented in accordance with academic rules and ethical conduct. I also declare that, as required by these rules and conduct, I have fully cited and referenced all material and results that are not original to this work.

Name, Last name : SUAT AKTEPE

Signature :

ABSTRACT

QUANTITATIVE SEISMIC INTERPRETATION AND RESERVOIR CHARACTERIZATION OF AKÇAKOCA PRODUCTION FIELD AT WESTERN BLACK SEA, TURKEY

Aktepe, Suat
Ph.D., Department of Geological Engineering
Supervisor : Prof. Dr. Nurkan Karahanoğlu
Co-Supervisor: Assist. Prof. Dr. Attila Arda Özacar

June 2015, 150 pages

Located in Western Black Sea, Turkey, Akcakoca Field is characterized by a deep water turbidite system, whose multiple reservoir sands represent the Kusuri Formation of Eocene aged and include a gas field of economic interest. Conducting seismic reservoir characterization and its integration with seismic based quantitative methods is the major challenge in these highly heterogeneous reservoirs. Therefore, a detailed 2D/3D seismic interpretation and 3D reservoir characterization are conducted in the Akçakoca Production Field. In order to constrain the reservoir model with secondary data, several quantitative techniques are applied such as well-log rock physics, Amplitude Versus Offset (AVO) and impedance inversions. A probabilistic link between facies, rock properties, and seismic can be obtained by using statistical techniques to account for heterogeneity within and between facies. This approach allows to predict the most likely facies distribution and to determine petrophysical properties from the seismic data. The applied methodologies ultimately improve the ability to delineate subtle traps and to characterize multiple reservoirs in complex depositional systems from seismic data. Furthermore, the way of integration of the secondary data is also important. For this reason, two main geostatistical simulation algorithms are applied and then tested one of which is Sequential Indicator Simulation (SIS) for facies, and other one is Sequential Gaussian Simulation (SGS) for petrophysical properties. Results of the seismic interpretation suggest that timing of the Eocene compression in the region significantly affects reservoir facies. Moreover, geostatistical modeling of reservoirs helps to delineate spatially correlated and stochastically constrained gas bearing sandstone facies from surroundings.

Key words: Turbidites, Eocene Clastics, Rock Physics, AVO, Inversion, Simulation.

ÖZ

AKÇAKOCA ÜRETİM SAHASININ KANTİTATİF SİSMİK YORUMU VE REZERVUAR KARAKTERİZASYONU BATI KARADENİZ, TÜRKİYE

Aktepe, Suat
Doktora., Jeoloji Mühendisliği Bölümü
Tez Yöneticisi : Prof. Dr. Nurkan Karahanoğlu
Ortak Tez Yöneticisi : Yrd. Prof. Dr. Attila Arda Özacar

Haziran 2015, 150 sayfa

Ekonomik bir gaz sahası olmasının yanı sıra Eosen yaşlı Kusuri Formasyonunda yer alan çoklu kumtaşı rezervuarlarıyla temsil edilen ve derin deniz türbiditik sistemi ile karakterize edilmiş olan Akçakoca sahası Türkiye'nin Batı Karadeniz kıyısında yer almaktadır. Heterojen yapıdaki rezervuarların sismik rezervuar karakterizasyonu ve sismik tabanlı sayısal metotların entegrasyonu en temel problemdir. Bu sebeple, Akçakoca üretim sahasında detaylı 2B/3B sismik yorum ve 3B rezervuar karakterizasyonu çalışması yürütülmüştür. Rezervuar modelinin ikincil veri ile sınırlandırılması amacıyla, kuyu logu kaya fiziği, genlik-offset ve empedans ters çözümü çalışması yapılmıştır. Fasiyes, kayaç özellikleri ve sismik arasındaki olası ilişki istatistiksel teknikler kullanılarak fasiyesler arası ve fasiyes içerisindeki heterojen yapıyı anlamak için kullanılabilir. Bu yaklaşım bize en olası fasiyes dağılımı ve petrofizik özellikleri sismikten tahmin etmemize olanak sağlar. Uygulanan metotlar temelde çözümü zor kapanları tariflemedeki ve karmaşık çökelim sistemlerindeki çoklu rezervuarları sismik yardımıyla karakterizasyonundaki yeteneğimizi arttırır. Bununla birlikte ikincil datanın nasıl ilişkilendirildiği de oldukça önemlidir. Bu sebeple iki temel jeo-istatistik simülasyon algoritması uygulanmış ve test edilmiştir. Bunlardan ilki fasiyesler için Ardışık İndikatör Simülasyonu (AİS) ve diğeri ise petrofizik özellikler için Ardışık Gaussian Simulasyonu (AGS). Sismik yorum sonuçları, bölgedeki Eosen sıkışmasının zamanlaması reservoir fasiyeslerini doğrudan etkilediğini göstermektedir. Rezervuarların jeo-istatistiksel modellenmesi sismik veri ile ilişkilendirilmiş stokastiksel olarak sınırlandırılmış gazlı kumtaşı fasiyeslerinin tariflenmesine yardım etmiştir.

Anahtar kelimeler: Türbiditler, Eosen kırıntılı istif, Kaya Fiziği, AVO, Ters Çözüm, Simülasyon.

ACKNOWLEDGEMENTS

There are many people that I would like to express gratitude towards. Of those people, I would first like to dedicate a tremendous amount of appreciation to my supervisor Dr. Nurkan Karahanoğlu for his leadership, guidance, and more importantly, patience. Secondly, I would like to thank my co-advisor Dr. Arda Özacar. He has played an important role in shaping my thesis. He has provided insightful and positive feedback during the incremental stages of my research. I would like to express my sincere thanks to Dr. Serhat Akın for his contribution to this study. I am also grateful to Dr. Nurretdin Kaymakçı, Dr. Ahmet T. Başokur and Dr. Selma Kadıoğlu for agreeing to be examiners of my defense.

I am very grateful Turkish Petroleum Corporation (TP) that generously provided my thesis data.

I would like to thank Dr. Özgür Sipahioğlu for his useful discussions and comments. He was very kind to spend his valuable time reading and editing my thesis. I would also like to thank Dr. Zühtü Batı for his support from very early stage to the end of this study.

I will remember having discussions with my colleagues Emre Bengü, Özge Karaman, Sarp Karakaya, Derya Kılıç Demirci, Özbil Yapar and anyone else who I may have missed.

Finally, I am most indebted to my wife, Arzu Aktepe, for her patience and encouragement. Without her endless support, the completion of my study would not be possible. My son Göktuğ deserves special thanks for letting me complete this thesis instead of having more play time with me.

DEDICATION

To my wife Arzu and my son Göktuğ

TABLE OF CONTENTS

ABSTRACT…….. IV

ÖZ ……..… V

ACKNOWLEDGEMENTS……..…. VI

DEDICATION…….……. VII

TABLE OF CONTENTS…….….. VIII

LIST OF FIGURES……..…….. X

LIST OF TABLES…….……. XXI

LIST OF SYMBOLS……..…….XXI

CHAPTERS

1 INTRODUCTION…… 1

1.1 Purpose and Scope……. 1

1.2 Location of the Study Area ……. 3

1.3 Data Sets …….. 3

2 GEOLOGY OF THE STUDY AREA…….…… 10

2.1 Introduction …… 10

2.2 Tectonic Settings ……..……. 10

2.3 Stratigraphy…… 14

2.4 Petroleum System of the Akcakoca Basin…… 15

3 METHODS……..…….. 18

3.1 Seismic Reflection……..….. 18

3.2 Conventional Seismic Interpretation……. 24

3.2.1 Surface Interpretation and Attributes …… 25

3.2.2 Well-tie and Correlation……..….. 26

3.2.3 Velocity Analysis and Modeling……... 26

3.2.4 Petrophysical Log Calculation and Evaluation…… 27

3.3 Quantitative Seismic Interpretation (QSI)…… 28

3.3.1 Rock Physics Analysis……... 28

3.3.2 Amplitude versus Offset (AVO)……. 33
3.3.3 Seismic Amplitude Inversion ……. 36
3.3.4 Forward Modeling …… 41
3.4 Deep Water Facies……. 42
3.5 Geostatistical Simulation …….…….. 47
4 RESULTS OF THE STUDY …… 52
4.1 Conventional Seismic Interpretation…..……. 52
4.1.1 Surface Interpretation and Attributes…… 52
4.1.2 Well-tie and Correlation…… 67
4.1.3 Velocity Analysis and Modeling…… 71
4.1.4 Petrophysical Log Calculation and Evaluation……. 73
4.2 Quantitative Seismic Interpretations…….. 79
4.2.1 Rock Physics …….. 79
4.2.2 AVO…… 86
4.2.3 Seismic Inversion ……. 88
4.2.4 Forward Modeling for the Blind Test Well Location……. 99
4.3 Facies Definition…… 101
4.4 Geostatistical Modeling……. 102
4.4.1 Data conditioning…… 104
4.4.2 Facies Modeling……. 111
4.4.3 Petrophysical Modeling ……. 117
5 CONCLUSIONS AND DISCUSSIONS……. 124
REFERENCES …… 135
VITA……..... 147

LIST OF FIGURES

FIGURES

*Figure 1 : Location map of the 2D and 3D seismic acquisition survey areas. Red dots represent well locations within the 3D area. .....**Error! Bookmark not defined.***

Figure 2: Common front end processing and fast track processing flow for Akçakoca-3D seismic survey (Courtesy of TPAO). 5

Figure 3: Kirchhoff PSTM migration processing flow for Akçakoca-3D seismic survey (Courtesy of TPAO). 6

Figure 4: Wells in the study area and available electrical logs. "√" represents the availability of the log and "X" represents that the data is not available for the listed well. 7

Figure 5: Left is a 2D Seismic section in time perpendicular to the shoreline and right is the same line with interpretation and its base map (time slice at 2100 ms). Black lines show the interpreted thrust faults and associated antithetic faults. Green horizon is water bottom. Blue horizon is top of Miocene. Purple horizon is top of Oligocene. Orange horizon is top of Sürmeli member of Kusuri Formation, yellow horizon is top of Akçakoca member of Kusuri Formation, red horizon is top of Akveren Formation and light blue horizon is top of Erikli member of Akveren Formation. Reflection geometries of the Erikli look undulating due to compressional deformation. Undulation intensifies and thickens towards the basin. These are interpreted as a series of thrust faulting with a basinward increasing throw amount. Red dash line on the base map indicates the major strike slip fault. 13

Figure 6: Generalized stratigraphic section for offshore Akçakoca gas field (courtesy of TPAO). 17

Figure 7: Snell's law for plane waves propagating in a two-layer medium. 20

Figure 8: Geologic model and related compressional sonic, shear sonic and density logs respectively from right to left. Acoustic impedance and reflection coefficient logs are calculated logs in depth. Reflectivity function is derived from acoustic impedance

and reflection coefficient logs. Convolution of reflectivity function with a wavelet (Ricker 50Hz) gives a seismic response of geologic model in time which is called synthetic trace represented by red wiggles. Recorded seismic traces shown in black and white are overlain by synthetic traces in red for comparison. *21*
Figure 9 : Minimum-zero phase wavelet and their amplitude and phase spectra. *23*
Figure 10: A group of seismic traces displayed in wiggle only (W), variable area (VA), variable density (VD) and variable density with wiggle (VDWG). *24*
Figure 11: Vertical resolution and the depth versus frequency, velocity and wavelength which are specifically modified for Akçakoca 3D. *25*
Figure 12: P-wave velocity versus porosity cross plot for several water saturated sediments starting from ocean bottom sandstone to consolidated sandstone (Avseth et al., 2005). *31*
Figure 13: Seismic amplitude inversion methodologies. *39*
Figure 14: The Bouma sequence and its 'depositional cone' (from Bouma, *1962)(from Mutti et. al. 2009).* *44*
Figure 15 : Schematic diagram of the architectural elements of fine-grained deepwater depositional systems. (Stratigraphic Reservoir Characterization, Slatt, 2006). *45*
Figure 16 : Generalized submarine-fan model of Walker (1978) (From Stratigraphic Reservoir characterization by R.M. Slatt). *47*
Figure 17 : Sürmeli Top a. depth structure map, b. time structure map, c. azimuth map, d. coherence map, e. dip map, f. instantaneous velocity map, g. dip azimuth map, h. interpreted seismic section,. Top reservoir laterally picked with purple line. Faults are drawn with thick black line at maps. Contours are in depth with 250 meters increment except time structure map which is in time with 400 millisecond increment and each of them drawn as thin black line. Thick red line indicates the location of the seismic section shown at 1h. *55*
Figure 18 : Thickness map of the Sürmeli member (left) and interpreted seismic which indicates Sürmeli interval (right). Change in thickness is minimum, only thickening is seen at the fault zone due to shortening. Southern boundary of the survey area is interpreted as erosional front due to uplifting. *56*

Figure 19 : AA Sand Top a. depth structure map, b. time structure map, c. azimuth map, d. coherence map, e. dip map, f. instantaneous velocity map, g. dip azimuth map, h. interpreted seismic section,. Top reservoir laterally picked with green line. Faults are drawn with thick black line at maps. Contours are in depth with 250 meters increment except time structure map which is in time with 100 millisecond increment and each of them drawn as thin black line. Thick red line indicates the location of the seismic section shown at 3h. 58
Figure 20 : F Sand Bottom a. depth structure map, b. time structure map, c. azimuth map, d. coherence map, e. dip map, f. instantaneous velocity map, g. dip azimuth map, h. interpreted seismic section,. Top reservoir laterally picked with light blue line. Faults are drawn with thick black line at maps. Contours are in depth with 250 meters increment except time structure map which is in time with 100 millisecond increment and each of them drawn as thin black line. Thick red line indicates the location of the seismic section shown at 4h. 59
Figure 21 : Thickness map of the Akcakoca member on the left and interpreted seismic which indicates Akcakoca interval on the right. Thick red line on the map indicates the location of the seismic section shown on the left. Folding at the hanging wall of the thrust faults is in maximum when the fault plane is close to the shoreline. Maximum folding is related to the shorting, and it shows the maximum increment of thickness at the southern boundary. Between the fault planes thickness is almost constant through the east west direction which may imply the sediment fairway is in south north direction. Overview of the thickness map shows general thinning towards the basin due to deposition. 60
Figure 22 : Top of Akveren formation a. depth structure map, b. time structure map, c. azimuth map, d. coherence map, e. dip map, f. instantaneous velocity map, g. dip azimuth map, h. interpreted seismic section. Top Akveren laterally picked with yellow line. Faults are drawn with thick black line at maps. Contours are in depth with 250 meters increment except time structure map which is in time with 100 millisecond increment and each of them drawn as thin black line. Thick red line indicates the location of the seismic section shown at 6h. 61

Figure 23 : Thickness map of the Akveren formation on the left and interpreted seismic which indicates Akveren interval on the right. Thick red line on the map indicates the location of the seismic section shown on the left. Thickness change at the fault zones are in maximum. Scale is relatively small and thickness is changing from 300 meters to 400 meters. 62
Figure 24 : RMS amplitude map of the D Sand. High amplitudes are in white and dim amplitudes are in black. Channelized geometries shown in white are the indication of relatively higher sand-shale ratio. Continuous black colored area is considered to be shale prone flood plain where the turbidite channels transport their sediment loads into the basin. 63
Figure 25 : Amplitude map of a channelize system at several frequency bands ranging from 5Hz to 45Hz. 65
Figure 26 : Spectrally decomposed (15x25x35Hz, RGB color coded) maps of a. A Sand, b. B Sand, b. B Sand, c. C Sand, d. D Sand, e. E Sand, and f. F Sand. 67
Figure 27 : Coherence map showing well locations which are classified with respect to their prospect positions. Field-1, 2 and 3 are the group of gas producing well locations. Field-4 is a single well location which is used for blind well test and interpreted separately. 68
Figure 28 : Well tie representation from Field-1 production area. Sonic, Density, Reflection Coefficients (RC), Impedance (IMP), Observed seismic inline section with 5 synthetic traces in red color and the extracted wavelet used at convolution. More than 60 % correlation exists between observed data and generated synthetic. It is in acceptable range. 69
Figure 29 : Well correlation 5 wells from the Field-3 production field with facies, density (RHOZ), porosity (EM_NPHI) and water saturation (SwA) logs. AA, A, B, and C sand top can be seen. Low density high porosity crosses from the logs are colored to yellow which indicates gas bearing sands. Water saturation (SwA) is colored to blue. 70
Figure 30: Well correlation at Field-2 location. A-Sand lithotype definition. Generated facies curve is plotted next to composite log and onto gamma log. Density, porosity curves are also plotted and any crossing area colored with yellow as an

indication of gas charge. Sand package is underlain by a gas water contact (GWC). 71
Figure 31: Velocity model building schemes. a. A simple constant velocity section x-line 3060 which is collected by matching formation top and interpreted surface and its time slice at 940 ms b. Velocity section x-line 3060 which is produced by a single time depth function distributed through surface and its time slice at 940 ms. c. Velocity section x-line 3060 which produced by multiple time depth functions interpolated through the surfaces and its time slice at 940 ms. d. Stacking velocities shown as section in x-line 3060 and its time slice at 940 ms. e. Inversely weighted interpolation of all the available velocity functions shown as section in x-line 3060 and its time slice at 940 ms. f. Least square tomographic solution for all velocity inputs and its time slice at 940 ms. 73
Figure 32: Permeability vs. porosity cross-plot shows comparison of the empirical permeability estimations with laboratory measurements of permeability (derived from the formula shown in figure 34) from core and outcrop samples (Data set is courtesy of TPAO). 75
Figure 33: Permeability vs. porosity cross-plot shows exponential relationship which can be formulized as shown. (Data set is courtesy of TPAO). 75
Figure 34: Amplitude map (high amplitudes are colored white) of A-Sand with wells represented by circles which colored and sized in order to emphasize a) depth of reservoir, b) average density, c) average gamma, d) average permeability, e) average porosity, f) average P wave velocity, g) average S wave velocity and h) average volume of shale. Min and max average log values are listed. 76
Figure 35: Amplitude map (high amplitudes are colored white) of DE-Sand with wells colored and resized in order to emphasize a) depth of reservoir, b) average density, c) average gamma log values, d) average permeability, e) average porosity, f) average P wave velocity, g) average S wave velocity and h) average volume of shale. Min and max average log values are listed as well. 79
*Figure 36 : a. Density versus gamma ray, b. Vp/Vs ratio versus gamma ray, c. lambda*rho versus gamma ray and d. mu*rho versus gamma ray from well logs. .. 81*

Figure 37 : P wave velocity vs. porosity for an interval between AA sand and DE sand. Black lines show Voigt and Reuss bounds. Color bar indicates the lithology defined by composite logs for the same interval. *82*
Figure 38 : P wave sonic versus S wave sonic crossplot combined with facies, effective porosity and density logs for fluid substitution brine case simulation, gas case simulation and in situ responses. Castagna's mud rock line and Greenberg-Castagna's sandstone line have been drawn for each cross-plot. *83*
Figure 39: Fluid discrimination using sonic log responses. a. Set of logs (P-wave, S-wave, Gamma ray, Density/Porosity). b. P-wave sonic vs. S-wave sonic cross-plot with facies log. Castagna et.al. 1993 mud rock line and Greenberg Castagna sandstone lines are drawn on to the cross-plot. c. Set of logs shown in figure 18a and colors in red for gas zone, green for water saturated zone and yellow for shale dominated zone are the responses of polygon shown in figure 18d. d. Same cross-plot shown in figure 18b except colors are transformed to color of polygons. Any sample that falls within drawn polygons is either gas-saturated, water-saturated or shale-dominated. Red arrows indicate good fit with the gas responses of density-porosity crossing. *85*
Figure 40 : Set of logs; facies (white), gamma (green), compressional sonic (white), shear sonic (white), density (purple), porosity (blue), lambda-rho (cyan) and mu-rho (green) are displayed respectively. Cross at density-porosity logs is colored with yellow in order to discriminate the gas saturated sandy reservoir. Cross-plot of lambda-rho-mu-rho is displayed with 3 polygons, green one represents gas saturated sand, yellow one represents shaly sand and red one showing water-saturated shaly sand. Each sample lying inside the polygons are drawn at vertical scale with proper color along the logs in order to show the correlated facies and fluids. Regression lines of polygons are shown with the related formula. Each formula is used while distributing the discriminated facies information through the 3D survey area. Grey scale seismic shows the well location, and red points are the distributed points from lambda-rho vs. mu-rho operation. *86*
Figure 41 : Density vs. porosity within the interval between AA sand and DE sand for all wells. There is a distinctive porosity density trend shown with red line for sandy

reservoirs. Color bar indicates the lithology defined by composite logs for the same interval at each well location. *87*
Figure 42 : METU-4 well, P-wave, S-wave, Gamma, Density, Porosity, and HC Saturation logs. Normal incidence synthetics and offset synthetics generated by using electrical logs. Offset synthetics are compared with observed Pre-stack gathers and full stack. Amplitude versus offset for gas saturated reservoir interval drawn with blue dots and it is underlain by a shaly interval which is drawn with green dots. Clearly amplitude response of the reservoir level gives class III AVO response which is identified by its increasing negative amplitude values with increasing offset. *88*
Figure 43 : Spectral Decomposition map shows a clear channelized system with two well locations, one is drilled and another one is considered as a prospect location. First well has tested one gas saturated sandy reservoir at the top, and it gives clear AVO response. However, same well has tested another deep interval which is represented by high amplitude reflections at the seismic, and it does not give a class III AVO response. Similarly, braided looking channelize system gives high amplitude zone at the south which is also considered as a prospect area, and it does not give a clear class III AVO response. Therefore, high amplitude zones in this particular prospect location are interpreted as lithology related amplitude anomalies rather than fluid. *89*
Figure 44 : A CDP gather before preconditioning and after band pass filter, radon and trim static applied. Angles are overlaid on to the gather as color coded. *91*
Figure 45 : Gradient analysis. a. a CDP gather before pre-conditioning. b. a CDP gather after band pass filter, radon filter and trim static applications. c. Gradient curves, amplitude vs. angles. Red line is plotted by using cdp gather before pre-conditioning and blue line is plotted by using cdp gather after conditioning. *91*
Figure 46 : CDP gathers. a. Pre-conditioned offset gathers. b. Pre-conditioned angle gathers. *92*
Figure 47 Estimated wavelets a. Statistical wavelet. b. Near, mid and far offset wavelet estimation. *93*
Figure 48 : Initial P-wave impedance model used for post, pre-stack inversions. *93*

Figure 49 : QC of inversion result. P wave impedance at a well location colored in blue and inversion result at the same location colored in red. An offset synthetic is generated by inversion results and correlation between synthetic and observed seismic is in satisfactory level (Corr=0.971322). Error is plotted in red for further QC. 95
Figure 50 : Pre-stack simultaneous inversion results. a. P wave impedance b. S wave impedance c. Vp/Vs ratio d. Density horizon slice at A Sand. 96
Figure 51 : Band limited, model based and spark spike post stack inversions at the top row and simultaneous P-wave, lambda-rho and mu-rho pre-stack inversion results are at the bottom row..... 97
Figure 52 : Frequency spectrum of the initial model, post stack and pre-stack inversion impedance results. a. Comparison of the different inversion algorithms b. Simplified representation of the initial model, post stack and pre-stack inversions. Initial model fits the low frequency gap which seismic in general does not have. Pre-stack inversion offers more high frequency content than post stack inversion. Thus, Pre-stack inversion is superior to the post stack inversion. 99
Figure 53 : Logs of the blind-well vs. simulated well log results between A sand top and DE sand bottom. P-wave, S-wave, density and calculated AI are colored in black for input logs. SGS reservoir property results are in red for P wave, yellow for sonic, cyan for density and blue for AI respectively.Simulation results show quite good fit tothe input curves eventhough the welland its logs were not gotinto the simulation. 100
Figure 54 : Walker's (1978) conceptual model for submarine fan. 102
Figure 55 Facies codes with their sample counts and proportions shown for each interval. 103
Figure 56 : Earth modeling work flow. 104
Figure 57 : a. A section view of 3D grid and b. A 3D view of 3D grid which indicates related faults and reservoir surfaces. 104
Figure 58 : Gamma values versus wells. Variety of gamma log responses indicates that it is hard to be drawn a common constant shale line on these logs. 105

Figure 59 : Gamma values versus MD, TVD and TIME function. Purple line shows original gamma log and green line indicates highly smoothed or filtered gamma log and finally cyan line shows subtracted gamma..... 106
Figure 60 : Residual gamma values versus wells. Scaled gamma ray values are between values of zero to 100. Any value smaller than 40 represents pure sand lithology and any value bigger than 60 represents pure shale lithology. In order to crosscheck these newly generated residual gamma ray logs, they are plotted together with effective porosity curves and any zone which has high porosity and low gamma ray values colored as yellow. Yellow zone indicates sandy lithology. These yellow zones overlay onto the composite log in order to compare them at close up view.. 107
Figure 61 : a. Histogram of density log values at all zones and wells. Green bars indicate sandstone density values b. Histogram of facies log values which simply sand=1, tuff=2, siltstone=3, claystone=4, marl=5, and shale=6. c. Histogram of density values for tuff only. d. Histogram of density values for claystone only. e. Histogram of density values for sand only. f. Histogram of density values for shale only. g. Histogram of density values for marl only. h. Histogram of density values for siltstone only. 108
Figure 62 : a. Density histogram of all logs before outlier analysis. b. Density histogram of all logs after outlier analysis. c. Multi-well outlier analysis of density. d. Multi facies outlier analysis of density. 109
Figure 63 : a. Q-Q plot for all porosity values. b. Q-Q plot only for porosity values of sandstone reservoirs. c. Q-Q plot only for porosity of sandstone reservoirs after outlier analysis. Each plot has its own chi test results, and none of them passes the chi test which simply indicates that porosity values are not normally distributed. 110
Figure 64 : a. Vertical variogram modeling of facies. It is an exponential model and red square shows the position of sill and range. Yellow circles are the log values in vertical direction and blue line is the vertical semi variogram model. b. Horizontal variogram modeling. It is an exponential model and red square shows the position of sill and range. Yellow circles are the log values in horizontal direction and blue line is the semi variogram model. c. Areal correlation of sandstone facies. 111

Figure 65 : Vertical variogram modeling of porosity. It is an exponential model and red square shows the position of sill and range. Yellow circles are the porosity values in vertical direction and blue line is the vertical semi variogram model. b. Horizontal variogram modeling of porosity. It is an exponential model and red square shows the position of sill and range. Yellow circles are the porosity values in horizontal direction and blue line is the semi variogram model. c. Areal correlation of sandstone porosities. 112

Figure 66 : Correlation of the secondary data which has been used at simulations. Yellow color represents sand facies, green color is shale, light green is shaly sand and orange is tuff. a. Probability of colored facies for a range of lambda-rho values at AA sand interval. b. Probability of colored facies for a range of mu-rho values at AA sand interval. c. Probability of colored facies for a range of Rho values at AA sand. d. Probability of colored facies for a range of Vp/Vs values at AA sand interval. 114

Figure 67 : a. Known channelized proportion curves are copied and distributed through the amplitude map which clearly indicates channel geometries and pre-define grid is in white. b. one of the proportion curve at well location. 115

Figure 68 : Lithology proportion map (LPM) and related proportion maps for each facies color bar shows red for 100 percent and blue for none. 116

Figure 69 : a. Sequential indicator simulation background model at AA Sand, b. Sequential indicator simulation calibrated with acoustic impedance at AA Sand and c. Sequential indicator simulation updated with lithology proportion map at AA Sand. 117

Figure 70 : Multi-histogram plot for facies. Blue for SIS background model, green for SIS calibrated with inversion, yellow for SIS updated with LPM and purple for input blocked lithotype log. Data range "1" is represents sandstone facies, "2" is shale, "3" is shaly sandstone, "4" is tuff. 118

Figure 71 : a. Sequential Gaussian Simulation (SGS) porosity model calibrated background facies model at AA Sand, b. SGS porosity model calibrated with impedance facies model at AA Sand and c. SGS porosity model calibrated updated with lithology proportion map facies model at AA Sand. 119

Figure 72 : Cross-plot of reservoir property simulation results (Porosity vs. Permeability). Samples are color-coded to facies and for the simplicity; it is divided into three facies type.Sandstone is in yellow,shale in green and shaly sand incyan. 120
Figure 73 : Well log correlation vs. simulation results a. Facies log correlation b. SIS facies model calibrated with impedance c. Permeability log correlation. d. SGS permeability model calibrated with impedance e. Density log correlation. f. SGS density model calibrated with impedance. g. Basemap of top reservoir. Blue line indicates the lineofsection and the position of projected wells..... 122
Figure 74 : Lithology curves for pre-defined blind test well. a. Observed lithology from cuttings and log interpretation b. Simulated lithology from SIS background trend c. SIS calibrated with seismic pre-stack inversion (Rho) d. SIS calibrated with seismic pre-stack inversion (Vp/Vs) e. SIS calibrated with seismic pre-stack inversion (MuRho) f. SIS updated with LPM. Location of the blind test well is at Field 4. It is a single well in that location (figure 28). 123
Figure 75: Left is the (i-iv) sequential line drawings of inversion steps which were taken through the transparent sidewalls of sand box model generated by (Gomes et al., 2010). E1-E3 are structures formed during extensional steps; F1 and F2 are forethrusts, and B1 and B2, backthrusts. Dashed and continuous lines represent extensional and contractional structures, respectively. Right is an Akçakoca field 2D seismic section in time perpendicular to the shoreline with interpretation and its base map (time slice at 2100 ms). Black lines show the interpreted thrust faults and associated antithetic faults. Green horizon is water bottom. Blue horizon is top of Miocene. Purple horizon is top of Oligocene. Orange horizon is top of Sürmeli member of Kusuri Formation, yellow horizon is top of Akçakoca member of Kusuri Formation, red horizon is top of Akveren Formation and light blue horizon is top of Erikli member of Akveren Formation. Reflection geometries of the Erikli look undulating due to compressional deformation. Undulation intensifies and thickens towards the basin. These are interpreted as a series of thrust faulting with a basinward increasing throw amount. Results of the sand box model of Gomes et al., 2010 (specifically, 40% shortening case iii) and the 2D interpretation at Akçakoca are conformable and

support each other. Faults within Akçakoca are named as F1, F2, F3, F4, and F5 for the trust faults which are at the same direction with the compressional forces. Back-trust faults are named B1 and B2. Finally, A1 is low angle compressional deformation related trust fault. Red dash line on the base map indicates the major strike slip fault..... 129

LIST OF TABLES

Table 1 : Summary of calculated logs with derived formulas, constants and input logs with names and units. 28

LIST OF SYMBOLS AND ABBREVIATIONS

Symbols / Abbreviations :		Definition
API	:	*American Petroleum Institute*
AVO	:	*Amplitude versus offset*
BVW	:	*Bulk volume of water*
ccdf	:	*Conditional cumulative density function*
CDP	:	*Common depth point*
Ch	:	*Channel*
DT	:	*Compressional sonic log (slowness)*
DT2	:	*Shear sonic log (slowness)*
DTC	:	*Compressional sonic*
DTfld	:	*Compressional sonic for fluid*
DTma	:	*Compressional sonic for matrix*
DTS	:	*Shear sonic*
GR	:	*Gamma ray log*
gr/cc	:	*Gram/cubic centimeters*
GRcln	:	*Gamma ray clean sand*
GRshl	:	*Gamma ray shale*
GWC	:	*Gas water contact*
HC	:	*Hydrocarbon*
Hz	:	*Hertz*
IK	:	*Indicator Krigging*
IMP	:	*Impedance*
i	:	*Layer*
K	:	*Bulk modulus*
Kdry	:	*Bulk modulus for saturation*
Kfluid	:	*Bulk modulus for fluid*
km	:	*Kilometer*
km2	:	*Square kilometer*
Kmineral	:	*Bulk modulus for mineral*
Ksat	:	*Bulk modulus for saturation*
LC	:	*Leveed channel*
LPM	:	*Lithology proportion map*

m	:	*Meter*
M	:	*Matrix*
max	:	*Maximum*
MD	:	*Measured depth*
mD	:	*MilliDarcy*
min	:	*Minimum*
ms	:	*Millisecond*
NMO	:	*Normal move out*
NPHI	:	*Neutron porosity*
OK	:	*Ordinary Krigging*
p	:	*Ray parameters*
P	:	*Parameter matrix*
Pdf	:	*Probability density function*
PERM	:	*Permeability*
PGS	:	*Plury Gaussian simulation*
PHIA	:	*Average porosity*
PHIE	:	*Effective porosity*
PI	:	*P-wave impedance*
Q-Q	:	*Quantile quantile plot*
QSI	:	*Quantitative Seismic Interpretation*
R0	:	*Resistivity*
RC	:	*Reflection coefficient*
RGB	:	*Red green blue*
RHOB	:	*Density*
Rhof	:	*Density fluid*
Rhom	:	*Density matrix*
RMS	:	*Root mean square*
Rp	:	*Reflected P-wave*
Rpp	:	*P-wave reflectivity*
Rs	:	*Reflected S-wave*
RT	:	*Resistivity*
Rw	:	*Water resistivity*
S	:	*Sheet sand*
S(Θ)	:	*Source at angle*
SEG	:	*Society of Exploration Geophysicist*
SGS	:	*Sequential Gaussian simulation*
SI	:	*S-wave impedance*
SIS	:	*Sequential indicator simulation*
SK	:	*Simple Krigging*
SoPhi	:	*Hydrocarbon pore volume*

SwA	:	*Archie water saturation*
SwIrr	:	*Irreducible water saturation*
TGS	:	*Truncated Gaussian simulation*
Tp	:	*Transmitted P-wave*
Ts	:	*Transmitted S-wave*
TVD	:	*True vertical depth*
TVDSS	:	*True vertical depth from subsea*
VA	:	*Variable area*
VD	:	*Variable density*
VDWG	:	*Variable density with wiggle*
Vp	:	*P-wave velocity*
Vpore	:	*Pore volume*
Vs	:	*S-wave velocity*
Vshl	:	*Volume of shale*
W	:	*Wiggle*
W(Θ)	:	*Wavelet at angle*
Z	:	*Acoustic Impedance*
%	:	*Percent*
λ	:	*Incompressibility*
μ	:	*Rigidity*
μ_{dry}	:	*Rigidity for dry rocks*
μ_{sat}	:	*Rigidity for saturated rocks*

CHAPTER 1

INTRODUCTION

1.1 Purpose and Scope

Conventional seismic interpretation aims to identify geologic structures, stratigraphy and reservoir architecture from seismic. The main goal of the conventional seismic interpretation in oil and gas exploration can be summarized as (1) detecting possible structures which may contain hydrocarbon accumulations, (2) delineating their areal extensions, and (3) calculating their volumes. The geometrical expression of seismic reflectors is mapped in space and travel time. However understanding of seismic amplitude, magnitude of amplitude and its variations along the reflection surface is subjected to quantitative seismic interpretation methods.

Contrasts in elastic properties for an interface are the source of seismic amplitude which help interpreter to understand lithology, porosity and saturation behavior as well as pore-fluid type. Commonly applied quantitative methods can be listed as (1) post-stack amplitude analysis, (2) offset-dependent amplitude analysis, (3) impedance inversion, and (4) forward seismic modeling. Presence of hydrocarbons can be validated by these quantitative methods during prospect evaluation, and extra information can be gained during reservoir characterization. The quantitative seismic interpretation and reservoir characterization require application of integrated techniques, and the final product of this integrated techniques are the spatial probability maps of reservoir fluids, facies and also stochastic realization of the reservoir properties.

Akcakoca field is a deep water turbidite system located in Western Black Sea, Turkey, whose reservoir sands represent the Kusuri formation of Eocene age and include a gas field of economic interest.

The aim of this study is to present results of detailed seismic reservoir characterization constrained by well-log rock physics, Amplitude Versus Offset (AVO) and impedance inversion which have been conducted and applied to Akçakoca 3D within the Akçakoca Field. A probabilistic link between facies, rock properties, and seismic response can be obtained by using statistical techniques to account for heterogeneity within, and between facies. This probabilistic approach allows us to predict the most likely facies and conditional probabilities of facies from seismic data. The applied methodologies ultimately improve the ability to delineate subtle traps and characterize reservoir units in complex depositional systems from seismic data.

The ultimate goal of this study was to obtain reliable quantitative estimates, with their uncertainties, for relevant reservoir rock and fluid parameters.

The four major components of the study are as follows:

1) Well-log analysis to define different seismic facies, rock physics analysis including fluid effects and seismic AVO analysis for different lithofacies and pore fluids.

2) Post and pre-stack seismic amplitude inversions to obtain 3D cubes of impedances and elastic parameters. Moreover, determine which inversion product offers the best discrimination of gas saturated reservoirs from water saturated reservoirs.

3) Nonparametric multivariate probability density estimation of facies and seismic impedances from wells and co-located seismic inversion.

4) Geostatistical classification of the 3D seismic impedance cubes to predict most likely facies and petrophysical properties, and obtain the spatial distribution of probabilities of occurrence by geostatistical framework (variogram-based co-kriging, simulation) for different lithofacies and petrophysical properties.

The obtained results are the most probable facies or property maps of the reservoirs which are linked to the rock physics, AVO and impedance inversion results. Moreover, high frequency content which is obtained by well-logs is preserved and stochastically constrained by simulation algorithms.

1.2 Location of the Study Area

The study area is located in the blocks “AR/TPO- TWY-FNV-POŞ/4990,4991” and “AR/TPO-POŞ-TWY-FNV/3499-3500/4877” in the Turkish Western Black Sea, which is densely covered by several 2D and a 3D seismic surveys. Having an area of 223 sq. km, Akçakoca 3D seismic is located to the north of the town of Akçakoca on the Black Sea coast of northwestern Turkey. The town of Ereğli is situated to the east of the survey area (figure 1).

1.3 Data Sets

The data set used in this study includes several 2D and a 3D seismic survey which cover an area of 223 km^2. 3D seismic was acquired by WesternGeco, an oilfield service company principally involved in providing geophysical services, between October 25 and November 18, 2004. The seismic survey vessel MV GECO TOPAZ towed 8 Q streamers with a streamer separation of 75 m giving a total width of 525m. The active length of each streamer was 4500 m long, towed at a depth of 6 m and with an average vessel speed of 4.5 knots. Dual source flip/flop of 1737 cubic inch arrays were used during the survey. 3D seismic data is recorded up to 4500 ms with a 2 ms sampling rate. The 2D lines used in regional interpretation have been shot at 2011. Total number of lines is 32 and total survey length is 1350 km. The active length of streamer is 6000 m. Each 2D seismic line has been recorded up to 6000 ms with a 2 ms sampling rate.

Akçakoca 3D seismic survey has been processed to obtain a product which is true amplitude preserved. Thus, AVO, inversion and stratigraphic analysis could be done based on responses of true amplitude behavior of the Earth at survey location. Processing flows of the “Fast Track Processing and Kirchhoff Pre-Stack Time Migration” are summarized in figure 2 and figure 3.

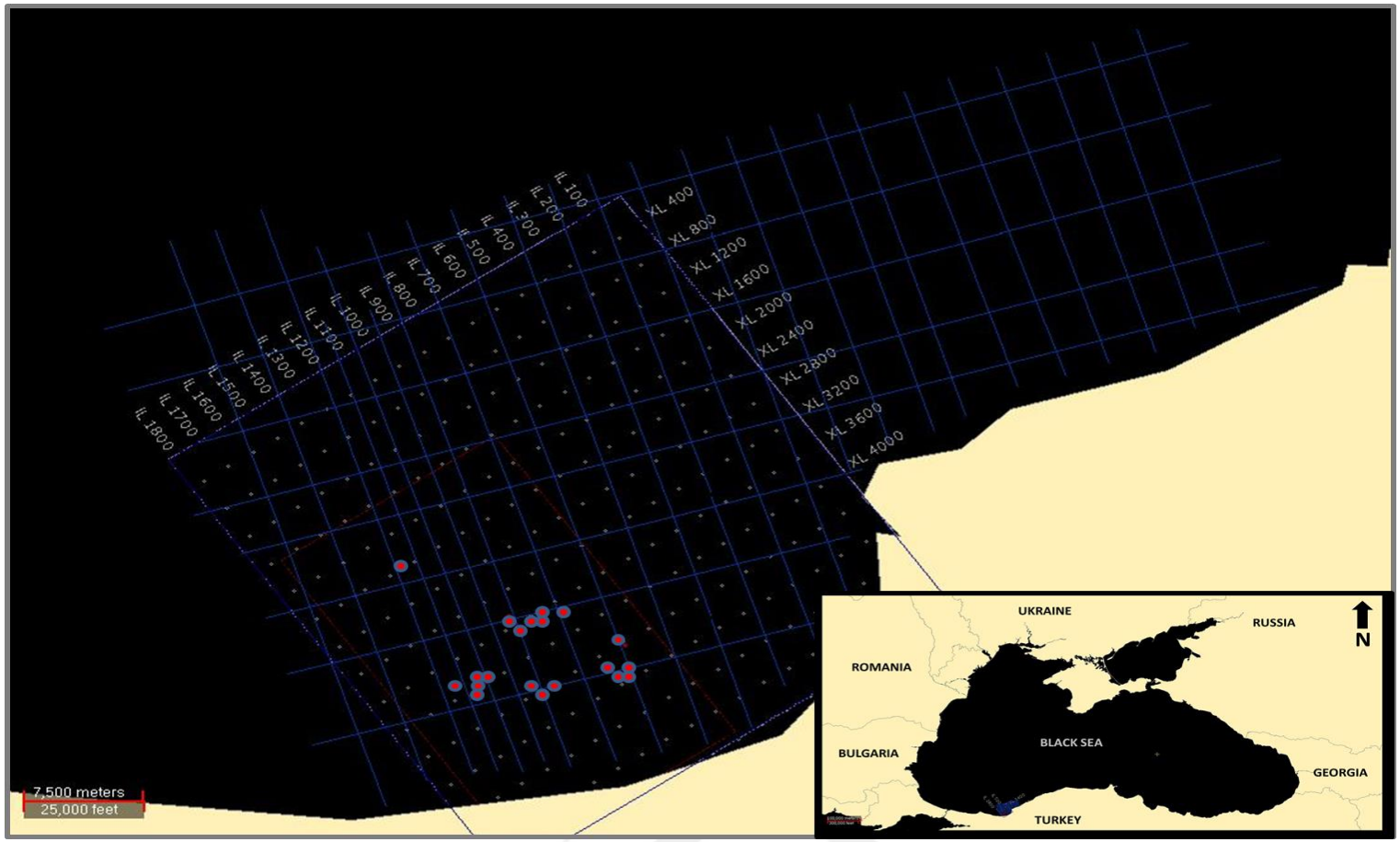


Figure 1: Location map of the 2D and 3D seismic acquisition survey areas. Red dots represent well locations within the 3D area.

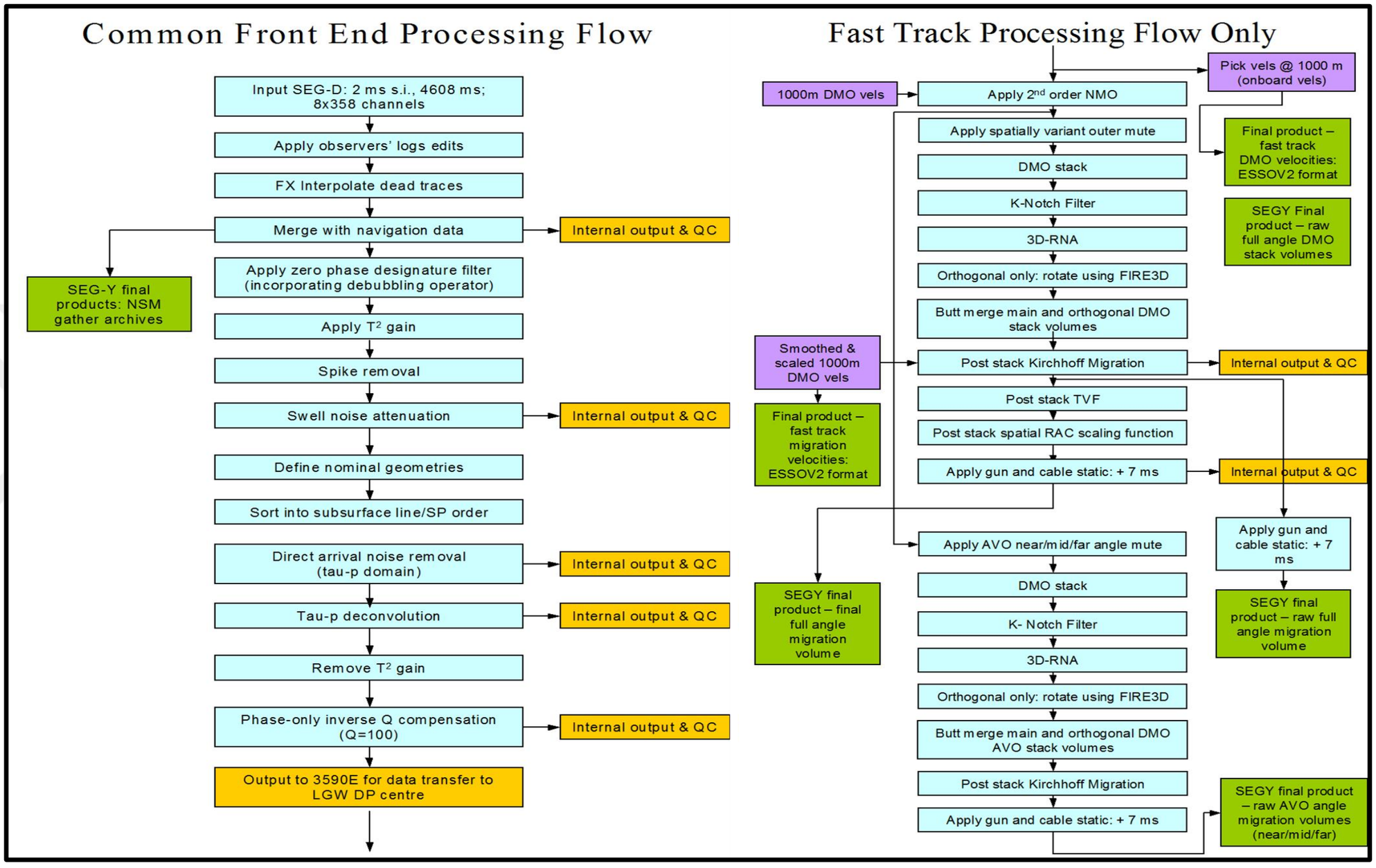


Figure 3: Common front end processing and fast track processing flow for Akçakoca-3D seismic survey (Courtesy of TPAO).

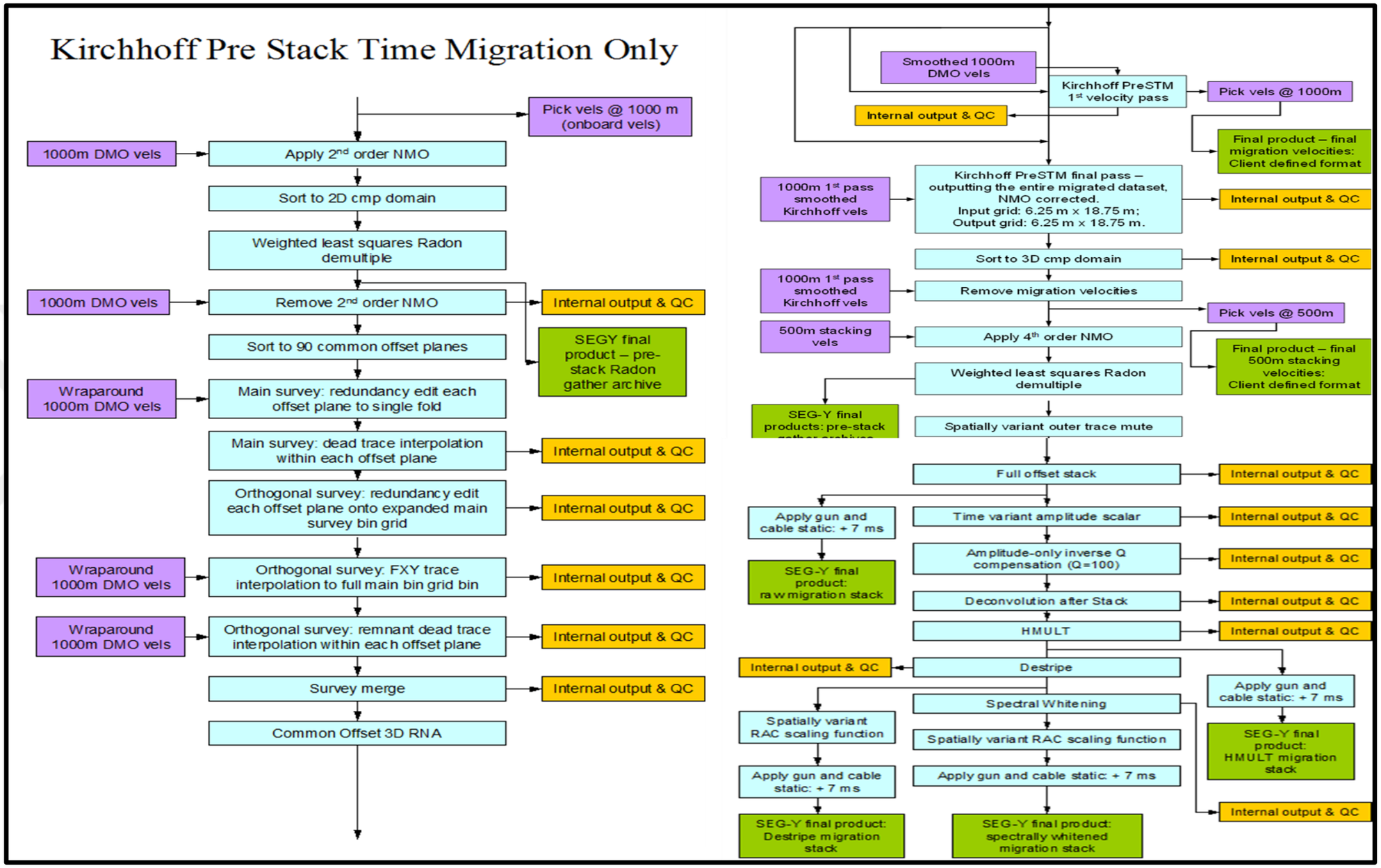


Figure 4: Kirchhoff pre-stack time migration processing flow for Akçakoca-3D seismic survey (Courtesy of TPAO).

In the study area, early exploration activities started at 1970's. Therefore, hydrocarbon potential of the Akçakoca field had long been recognized before the Akçakoca 3D seismic survey was acquired. During late 1990s to early 2000s, aggressive development plan for the Akçakoca field was designed, and therefore several exploration, appraisal and development wells drilled in the area. Since the wells were drilled for different purposes, their designs and logging configurations vary as well. Figure 4 shows list of wells together with available logs for each well which are used in this study.

Well Name	CALI (Caliper) in	DT (P-Wave) us/ft	DT2 (S-Wave) us/ft	GR (Gamma) API	LLD (Resistivity) ohm-m	LLS (Resistivity) ohm-m	MSFL (Resistivity) ohm-m	NPHI (Neut. Porosity) %	PIGE (Frac Porosity) %	RHOB (Density) g/cc	SP (Potential) mV
WELL-01	√	√	X	√	√	√	√	√	√	√	√
WELL-02	√	√	X	√	√	√	X	√	√	√	√
WELL-03	√	√	√	√	√	√	√	√	√	√	X
WELL-04	√	√	X	√	√	√	√	X	√	√	√
WELL-05	√	√	X	√	√	√	√	√	X	√	√
WELL-06	√	√	√	√	X	X	√	√	√	√	√
WELL-07	√	√	X	√	√	√	√	√	X	√	√
WELL-08	√	√	√	√	√	√	√	√	√	√	√
WELL-09	√	√	√	√	√	√	√	√	√	√	√
WELL-10	√	√	√	√	√	√	√	√	X	√	√
WELL-11	√	√	X	√	√	√	√	√	√	√	√
WELL-12	√	√	√	√	√	√	√	√	√	√	√
WELL-13	√	√	X	√	√	√	√	√	√	√	√
WELL-14	√	X	X	√	√	√	√	√	√	√	X
WELL-15	√	√	X	√	√	√	√	√	√	√	√
WELL-16	√	√	X	√	X	X	X	√	X	√	√
WELL-17	√	√	√	√	√	√	√	√	√	√	X
WELL-18	√	√	√	√	√	√	√	√	X	√	√
WELL-19	√	√	√	√	√	√	√	√	X	√	√
WELL-20	√	√	√	√	√	√	√	√	√	√	√
WELL-21	√	√	√	√	√	√	√	√	√	√	√
WELL-22	√	√	√	√	√	√	√	√	√	√	X
WELL-23	√	√	√	√	√	√	√	√	X	√	√

Figure 5: Wells in the study area and available electrical logs. "√" represents the availability of the log and "X" represents that the data is not available for the listed well.

In addition to the listed material, there are extensive well reports such as daily geological reports, positioning and survey reports, the end of well reports, and paleontology/palynology reports internally prepared by TPAO or the related service companies. These reports were at the background during the study and will be referred as courtesy of TPAO.

CHAPTER 2

GEOLOGY OF THE STUDY AREA

2.1 Introduction

The Black Sea is located between the north of Turkey and the south of Ukraine and Russia, bordered to the west by Romania and Bulgaria and to the east by Georgia (Figure 1). The general geological setting of the Black Sea basin has been known for many years (Ross et al., 1974; Letouzey et al., 1977; Zonenshain and LePichon, 1986; Manetti et al., 1983; Okay, 1994). This chapter aims to summarize the researches previously done in the Black Sea basin in order to understand origin of the Akçakoca Basin in global tectonic concept and its stratigraphy which is supported by wells drilled at the Akçakoca basin. Furthermore, elements of petroleum system of Akçakoca basin are explained in short.

2.2 Tectonic Settings

The Black Sea is generally considered to be a result of back-arc extension associated with northward subduction of the Tethyan plate in late Early Cretaceous times (Finetti et al., 1988; Robinson, 1997; Nikishin et al., 2003; Muntenau et al., 2013). Even though it is shaped by extensional deformation at the beginning, subsequent compressional deformation during later stages is responsible for the recent shape of the most of the Black Sea margins (Spadini et al., 1997). The Pontides along the northern shoreline of Turkey, the Greater Caucasus and Gorni-Crimea mountain belts in Russia and Ukraine are the examples seen today. Present day basin floor is about 2200 m deep flat abyssal plain, acting as a blanket hiding two adjacent basins called Western and Eastern Black Sea basins. Opening of the Western Black Sea Basin (WBSB) is a result of the separation of the western and central Pontides from the Moesian Platform (Finetti et al., 1988; Görür, 1988; Görür, 1997; Robinson, 1997;

Nikishin et al., 2003; Muntenau et al., 2013). Middle Baremian age rifting is followed by post rift subsidence and oceanic crust emplacement in the Cenomanian (Belousov et al 1988; Finetti et al,. 1988; Görür, 1988; Görür, 1997; Spadini et al., 1997). During the post rifting stage, from Late Cretaceous to the recent day, more than 10000 m sediments (as observed in regional seismic lines) were deposited.

Moesian Platform, which existed from Late Jurassic to Early Cretaceous is a carbonate platform located at the southern margin of the Laurasian Supercontinent (Finetti et al., 1988; Görür, 1988; Görür, 1997; Robinson, 1997; Nikishin et al., 2003; Muntenau et al., 2013). Generation of the rifted WBSB is attributed to extensional deformation of the Moesian Platform (Görür, 1993; Görür, 1997; Spadini et al., 1997). Evidences can be seen at outcrops and wells as highlighted by Görür et al., 1993. The Middle Barremian limestones, İnalti formation, in the Western Pontides are unconformably overlain by Albian-Abtian-aged Çağlayan and Ulus formations which are synrift sediments (shallow water sandstones, submarine slides, olistostromes and turbidites) (Görür et al., 1993; Görür, 1997). Cenomanian-aged Kapanbogazi Formation (pelagic carbonates and distal tuffs) unconformably overlies the synrift strata (Görür et al., 1993; Görür, 1997). This unconformity might be indication of the change from rift to drift in the Western Black Sea (Görür et al., 1993; Görür, 1997).

The Akçakoca reservoirs are shaped by the post-rift compressional deformation that occurred in the Eocene (Finetti et al., 1988; Yılmaz et al., 1997; Stephenson et al., 2004; Munteanu et al., 2011; Munteanu et al., 2013). The upper member of Kusuri Formation, Sürmeli member, had already been deposited when the deformation occurred whose supporting evidence can be seen in isopachous, concordant reflection geometries it possesses in seismic sections (Figure 5). This observation is also valid for Akçakoca member. Furthermore, any interpreted horizon along the reservoir level in Akçakoca 3D survey is characterized by channel geometries in amplitude maps. These geometries are not controlled by compressional deformation-related faulting proving that such deformation postdates the deposition of the Akçakoca member. This observation reveals that compressional deformation starts at Eocene and continues up to Early Oligocene (Figure 5 and 75). Any sediment

younger than Early Oligocene does not show any significant reflection geometry which may imply compressional deformation.

Reflection geometries of Erikli member of Akveren Formation, on the other hand, show undulating geometries due to compressional deformation. Undulation intensifies and thickens towards the basin which indicates deformation related accumulation along the Erikli. Seismic interpretation shows a series of thrust faults (with increasing displacement towards the basin) develop with diminishing throws towards the shoreline direction (Figure 5). Foreland propagated displacement generates a series of forethrusts which are getting younger (as young as Early Oligocene) towards the basin. Foreland propagated displacement also generates strong differential stress which is only possible with a backstop (Gomes et al., 2010). In this study, Yemişliçay has been interpreted as foreland dipping backstop that is unconformably overlain by the basin infill.

Regional 2D seismic lines carry valuable information which suggests a NW-SE elongated strike slip fault (Figure 5) along with southern margin uplift. Amount of uplift at eastern block is considerably higher than the uplift that we see at western block of the strike slip fault plane.

In conclusion, Akçakoca basin is considered as an inverted half graben which was initiated during the Middle Baremian rifting and inverted by Late Eocene compressional deformation. In such a basin, rheologic contrast between the basement and the synrift sedimentary sequences control the inversion process (Gomes et al., 2010). Compressional deformation, in the study area, is represented by a series of north-vergent thrust faults and their south-vergent back thrust components (Figure 5 and 75).

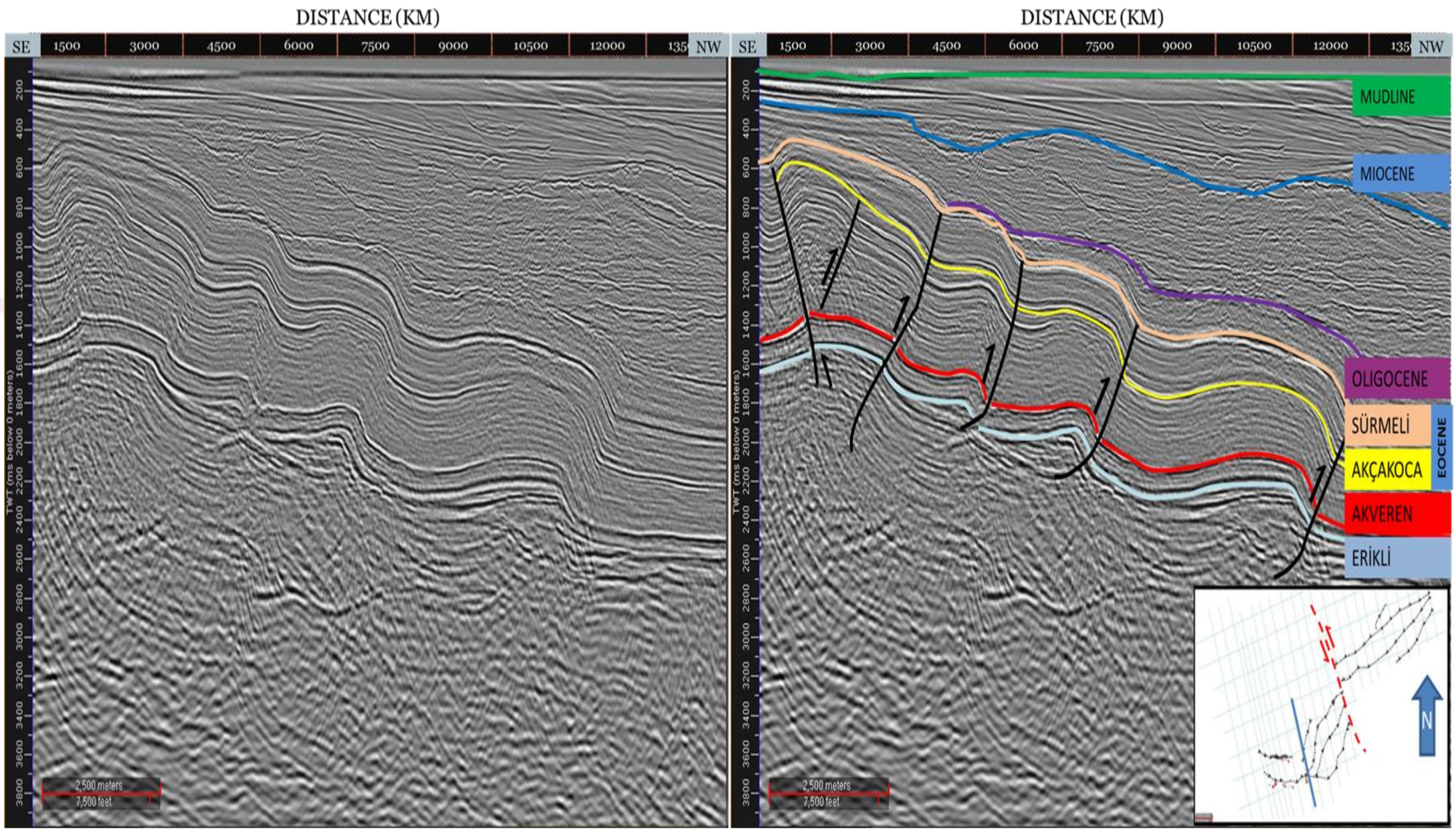


Figure 6: Left is a 2D Seismic section in time perpendicular to the shoreline and right is the same line with interpretation and its base map (time slice at 2100 ms). Black lines show the interpreted thrust faults and associated antithetic faults. Green horizon is water bottom. Blue horizon is top of Miocene. Purple horizon is top of Oligocene. Orange horizon is top of Sürmeli member of Kusuri Formation, yellow horizon is top of Akçakoca member of Kusuri Formation, red horizon is top of Akveren Formation and light blue horizon is top of Erikli member of Akveren Formation. Reflection geometries of the Erikli look undulating due to compressional deformation. Undulation intensifies and thickens towards the basin. These are interpreted as a series of thrust faulting with a basinward increasing throw amount. Red dash line on the base map indicates the major strike slip fault.

2.3 Stratigraphy

Stratigraphic model of Spadini et al. (1997) simply summarizes the possible evaluation of the WBSB stratigraphy which started with the rapid basement subsidence during the rifting in Middle Barremian and followed by a major basin starvation era which is responsible for the limited development of the syn-rift sediments. After rifting is completed, high rate of sedimentation occurred in the basin center and sediment bypass led to relatively low rate of sedimentation at the basin margins. At the southern margin of the WBSB, two phases of compression are observed, the first one in Middle Eocene and the second one in Late Eocene (Finetti et al., 1988; Yılmaz et al., 1997; Stephenson et al., 2004; Munteanu et al., 2011; Munteanu et al., 2013). Oligocene-aged deep water sediments onlap onto the Upper Cretaceous paleo-high at the south margin of the Black Sea and do not reach neither Akçakoca 3D survey area nor the present-day shoreline position. The basin underwent another compressional deformation during Early and Middle Miocene. During the Late Miocene, water depth increased as a result of the basement subsidence, creating a huge accommodation space. This sudden increase in water depth and high rate of sedimentation is represented in seismic sections as chaotic seismic reflections along the southern margin of the Black Sea (Figure 6). During the Quaternary, the rate of tectonic subsidence slowed down, leading to deposition of a thin sedimentary package (figure 6) (Muntenau et al., 2011; Stuart et al., 2011).

Figure 2 shows a generalized stratigraphic section which is compiled from various data sets including the wells drilled both onshore and offshore Western Black Sea as well as outcrops along the Turkish Western Black Sea shoreline and extensive 2D/3D seismic data sets which cover the south of the Western Black Sea.

Most of the wells in the field tested, Plio-Quaternary section as a sequence of shallow to deep marine interbedded fine grain sandstone, claystone and shale. Miocene section mainly consists of siltstone, claystone and shale. Oligocene section is either truncated or not deposited, and thus Miocene – Eocene transition is recognized as major unconformity surface. The Eocene-aged Sürmeli member of Kusuri Formation consists of sandstone, claystone, siltstone, and tuff sequence. In cutting samples, the Sürmeli sandstones are described as light grey colored, scattered polygenetic, fine to

medium, rarely coarse grained, angular subangular, subrounded medium sorted, intergranular weak porosity with many fossil shells. Claystones are defined as light grey, light green colored, soft sticky, rarely hardy weak carbonaceous, interbedded with fossil shells. Siltstones are described as grey, light green, colored soft, carbonaceous, interbedded with sandstone and, tuffs are defined as grey, light grey colored hardy and brittle.

Akçakoca member of the Kusuri Formation contains several gas saturated sandstone intervals, and thus, is considered as reservoir. Sandstones in Akçakoca member are summarized as light grey, off-white colored, soft carbonaceous, claystone interbedded from the cuttings. Claystones are defined as white, light grey colored soft-hardy, soft carbonaceous. Siltstones are described as light grey, off-white colored soft carbonaceous, claystone interbedded. Shales are defined as light green, light grey, white color, hardy hard, carbonaceous. Marls are summarized as light grey, grey, white color and soft, rarely hardy, rarely silty. Cutting definitions mainly assist the facies to lithotype transformation for reservoir classification (Figure 54).

Late Cretaceous Akveren Formation consists of limestone, marl, shale and claystone sequences which are underlain by Erikli sandstones, a member of Akveren Formation. There is no well tested deep marine Erikli sandstone in a location underlain by Sarıkorkmaz formation which consists of dominantly fluvial sandstone. Finally, the whole section is underlain by Yemişliçay Formation which contains volcanics and volcanoclastics. There are only two wells in the field which penetrated the Devonian-aged Yılanlı Formation, which is dominantly composed of dolomitic chert and fossiliferous limestone (Figure 6).

2.4 Petroleum System of the Akçakoca Field

The source rock in Akçakoca Field is not well defined, and existing hydrocarbons (gas) are considered to have a biogenic source which is the product of local biogenic activity at the reservoir level and only preserved under certain conditions of depth, pressure, and temperature.

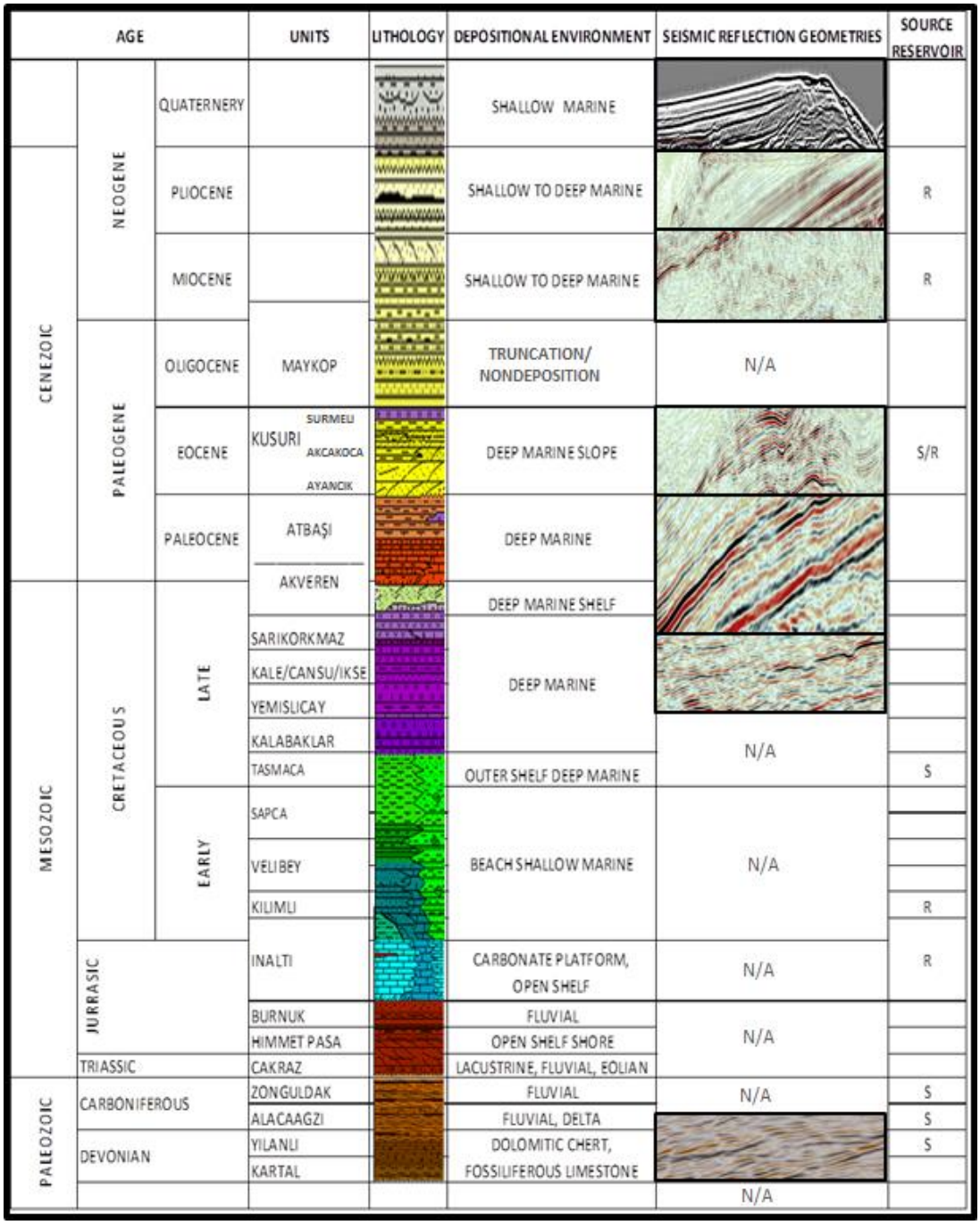


Figure 7: Generalized stratigraphic section for offshore Akçakoca gas field (courtesy of TPAO).

However, in the literature (Görür et. al. 1997), there are several potential source rock intervals (mostly proven by laboratory measurements) which have possibility of lateral and vertical charge. One observation is really important from the conceptual faulting model drawn in figure 5. All the producing wells are located at the south-vergent thrust fault, and north-vergent thrusts are not promising for the hydrocarbon exploration or there is no such evidence. This may lead us to conclude, even though the Akçakoca reservoir is considered to be a biogenic gas reservoir, south-vergent thrust fault-related thermogenic gas charge from the basin is theoretically possible.

Akçakoca reservoirs are located within the Eocene aged Kusuri Formation. Kusuri Formation consists of three members, Sürmeli at the top, Akçakoca in the middle and Ayancık at the bottom (Görür et. al. 1997). Even though the Sürmeli and Ayancık members are defined as products of turbiditic clastic systems which consists of sandstone and shale sequences, they have no proven hydrocarbon potential tested with wells. Akçakoca member is also described as turbite system. Its reservoir levels consist of sand rich channels, sand dominated point bars, and lobes with sheet sands.

Shaly intervals of Kusuri Formation constitute the seal rocks in Akçakoca Field. Main reservoir levels are sand-filled, high to moderate sinusoidal submarine channels which are capped by either shaly floodplain deposits or shale dominated levees of the system. Akçakoca reservoirs show meandering geometries which contain laterally and vertically stacked sand-rich point bar deposits. In some places, these point bars are sealed by clay plugs as well.

Trap mechanism is mainly structural and controlled by south-vergent thrust faults. Traps at Akçakoca field are interpreted to have formed by folding of the hanging-wall of the south-vergent thrust faults. Reservoirs show east-west elongated geometries which are structurally closed in 3-ways against the south-vergent thrust faults. Specifically, the apex of folded hanging wall of the thrust fault acts as the top of the trap, and it is laterally limited to the south by the fault plane itself.

CHAPTER 3

METHODS

The purpose of this chapter is to introduce principles of the research methods and the methods used for obtaining input data. Various types of data from different disciplines have been combined and modeled into a series of simulations. Seismic methods and seismic related statistical methods are briefly summarized in order to build a basic understanding of the research methodology. Furthermore, simulation methods are explained in order to understand reservoir characterization techniques.

3.1 Seismic Reflection

There are three phenomena which can occur when a wave encounters an interface. These are (1) reflection, (2) refraction and (3) conversion of the propagated wave (Figure 7). Reflection is defined as the energy or wave from a source that has been reflected back from an acoustic impedance contrast (reflector) or series of contrasts within the Earth (Sheriff, 2002). When a seismic wave encounters an interface between two materials (lithologies) with different acoustic impedances, some of the energy in the wave is reflected, while some of the energy continues (transmitted) through the interface. By observing changes in the strength of reflectors, contrasts in acoustic impedances can be predicted and used to infer changes in the properties of the rocks at the interface, such as density and elastic modulus.

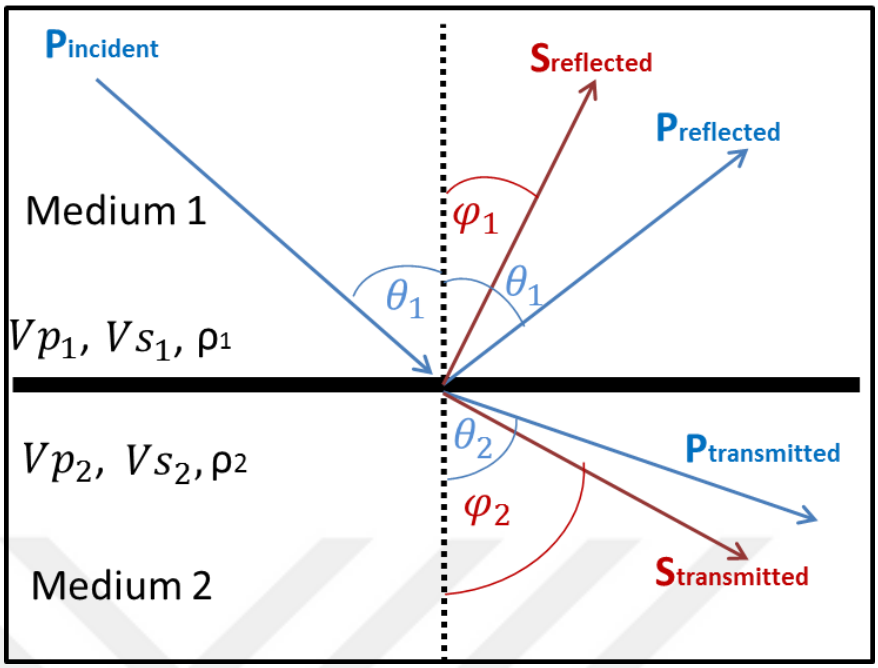


Figure 8: Snell's law for plane waves propagating in a two-layer medium.

By observing the interaction of a plane wave upon an interface of two semi-infinite half spaces, four different energy partitions result from an incident P-wave. These partitions are (1) a reflected P-wave, (2) a transmitted P-wave, (3) a reflected S-wave, and (4) a transmitted S-wave (Castagna and Backus, 1993). The angles of each partition may be calculated using Snell's law,

$$p = \frac{sin\theta_1}{Vp_1} = \frac{sin\theta_2}{Vp_2} = \frac{sin\varphi_1}{Vs_1} = \frac{sin\varphi_2}{Vs_2} \quad 3.1$$

where, Vp_1 and Vp_2 are the P-wave velocities in medium 1 and medium 2, respectively; Vs_1 and Vs_2 are the S-wave velocities in medium 1 and medium 2, respectively; θ_1 and θ_2 are the incident P-wave angle, and the transmitted P-wave angle, respectively; φ_1 and φ_2 are the reflected S wave angle, and the transmitted S wave angle, respectively. Finally p is the ray parameter and, it is constant along each ray (Figure 7).

Seismic rays obey Snell's Law just like in optics. The angle of incidence equals the angle of reflection, and the angle of transmission is related to the angle of incidence through the velocity ratio as we see in the equation 3.1. The conversion from P wave to S wave or vice versa can also occur.

Zoeppritz, 1919 derived amplitudes of the reflected and transmitted waves using the conservation of stress and displacement across the interface, which yields four equations with four unknowns.

$$\begin{bmatrix} R_P \\ R_S \\ T_P \\ T_S \end{bmatrix} = \begin{bmatrix} -\sin\theta_1 & -\cos\phi_1 & \sin\theta_2 & \cos\phi_2 \\ \cos\theta_1 & -\sin\phi_1 & \cos\theta_2 & -\sin\phi_2 \\ \sin 2\theta_1 & \frac{Vp_1}{Vs_1}\cos 2\phi_1 & \frac{\rho_2 {Vs_2}^2 Vp_1}{\rho_1 {Vs_1}^2 Vp_2}\cos 2\phi_1 & \frac{\rho_2 Vs_2 Vp_1}{\rho_1 {Vs_1}^2}\cos 2\phi_2 \\ -\cos 2\phi_1 & \frac{Vs_1}{Vp_1}\sin 2\phi_1 & \frac{\rho_2 Vp_2}{\rho_1 Vp_1}\cos 2\phi_2 & \frac{\rho_2 Vs_2}{\rho_1 Vp_1}\sin 2\phi_2 \end{bmatrix}^{-1} \begin{bmatrix} \sin\theta_1 \\ \cos\theta_1 \\ \sin 2\theta_1 \\ \cos 2\phi_1 \end{bmatrix}$$

3. 2

In seismic reflection method, response of the elastic wave field to velocity and density contrasts across interfaces of sediments is recorded and called seismic trace. The acoustic impedance and the reflection coefficient values of a layer can be determined by velocity and density properties. Simple conversion from depth function of reflection coefficients to time function of reflectivity is possible (Figure 8). Time domain reflectivity function is convolved with the proper wavelet, and the result is a noise free seismic trace. Noise can be added at any time after generating the trace.

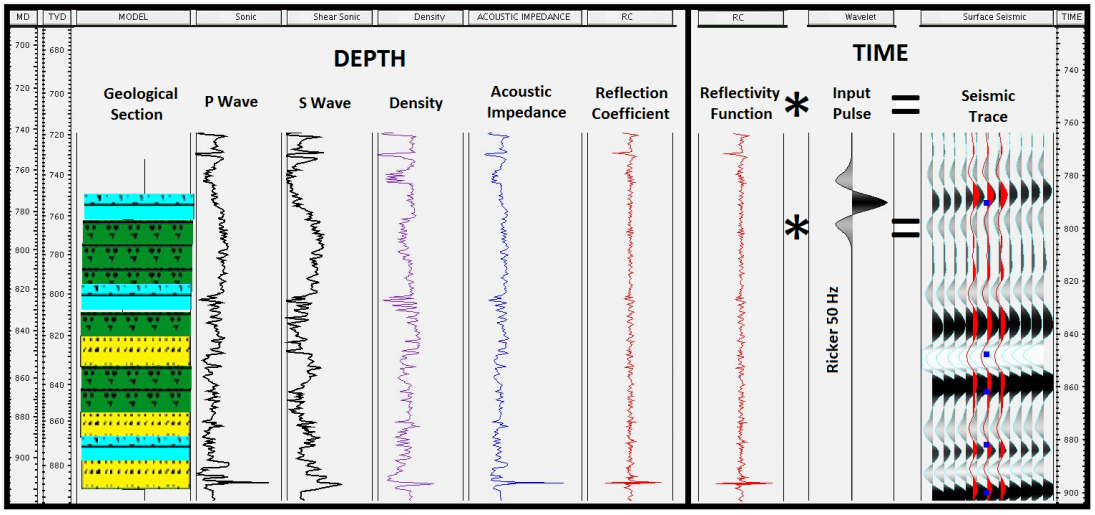


Figure 9: Geologic model and related compressional sonic, shear sonic and density logs respectively from right to left. Acoustic impedance and reflection coefficient logs are calculated logs in depth.

Reflectivity function is derived from acoustic impedance and reflection coefficient logs. Convolution of reflectivity function with a wavelet (Ricker 50Hz) gives a seismic response of geologic model in time which is called synthetic trace represented by red wiggles. Recorded seismic traces shown in black and white are overlain by synthetic traces in red for comparison.

At the early interpretation stage, the concept of polarity should be introduced and set by interpreter. Instead of describing reflections as positive or negative, it is more usual to use the term *polarity*. The Society of Exploration Geophysicists (SEG) defines *normal polarity* as a positive seismic signal produces a positive acoustic pressure on a hydrophone in water or an upward initial motion on a geophone on land. A positive seismic signal is a pick on a seismic as SEG standard suggested. For example, the water bottom interface between the low impedance water and the high impedance mud deposits is characterized by a trough at the seismic.

For the interpreter to evaluate the pulse shape, it is necessary to know at which basic wavelet shape processing was aimed. This is not necessarily the same as the input pulse, since transformations to a new wavelet are often made during processing. In an extremely simplified way, seismic wavelets displayed on seismic sections can be grouped into two main types, minimum and zero phases (Figure 9). Although this is a reasonable simplification for the interpreter, it may not be for the processing geophysicist or the modeler.

The seismic data used in this study has a normal polarity, and it is processed with and converted to zero phase wavelet. Figure 9 shows normal and reverse polarity displays for two common seismic pulse types which are minimum phase and zero phase pulses.

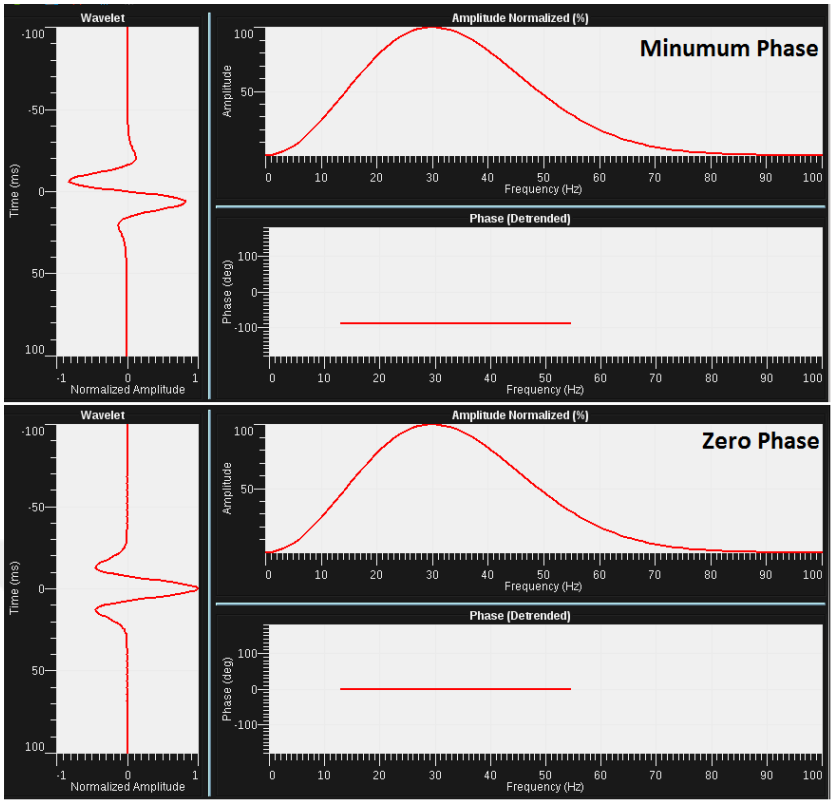


Figure 10 : Minimum and zero phase wavelet and their amplitude and phase spectra.

There are several ways to display seismic traces; wiggle (W), variable area (VA), variable density (VD) and wiggle variable density (VDWG) (Figure 10). Display preferences can be changed depending on the phenomena that need to be highlighted. In this study, the seismic lines were demonstrated in a variable density display, which was preferred for seismic facies analysis and the interpretation. The amplitudes are often plotted in different grayscales or in colors (variable density). In this way, the differences in amplitudes are more clearly observed. In wiggle display, the amplitude is depicted as a curve for a simple representation. Wiggle display is preferred in order to emphasis the correlation between normal incident synthetic and the zero offset seismic. Likewise, offset synthetic and the pre conditioned pre-stack angle gathers are displayed with wiggle.

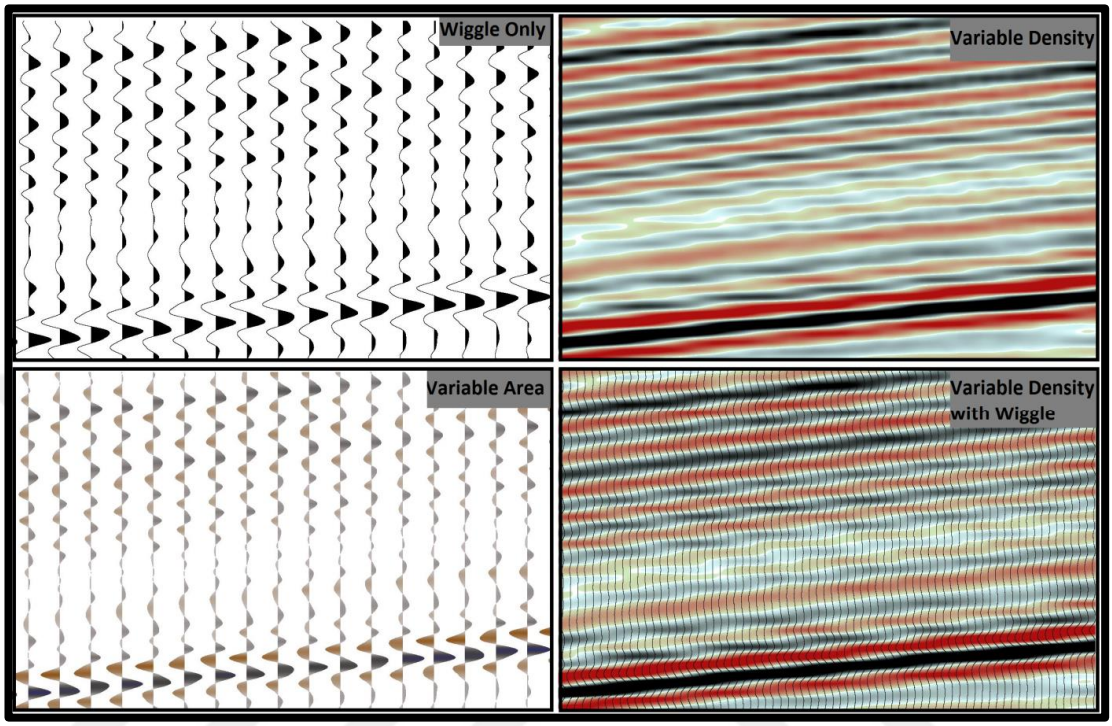


Figure 11: A group of seismic traces displayed in wiggle only (W), variable area (VA), variable density (VD) and variable density with wiggle (VDWG).

Seismic resolution is defined as the minimum distance between two objects which can be identified separately by the seismic wave. The relationship between frequency, velocity, and wavelength is straightforward shown in Figure 11. Unfortunately, both velocity and frequency show an overall change with depth which causes a gradual decrease in resolution. This might reduce our perception of the reflection pattern and our ability to interpret the seismic section.

	Age of rocks		Very Young	Young	Medium	Old	Very old
	Depth of target	m	100-400	400-700	700-1000	1000-1300	1300-1600
	Formation Velocity	m/s	1500	1600	1700	1800	1900
	Predominant Frequency	Hz	80	40	20	10	5
	Wavelength	λ	18,75	40,00	85,00	180,00	380,00
LIMIT OF SEPARABILITY		λ/4	4,69	10,00	21,25	45,00	95,00
Poor S/N	e.g. Water sand poor data	λ/8	2,34	5,00	10,63	22,50	47,50
Moderate S/N	e.g. Water or oil sand fairly good data	λ/12	1,56	3,33	7,08	15,00	31,67
High S/N	e.g. Gas sand good data	λ/20	0,94	2,00	4,25	9,00	19,00
Outstanding S/N	e.g. Gas sand excellent data	λ/30	0,63	1,33	2,83	6,00	12,67

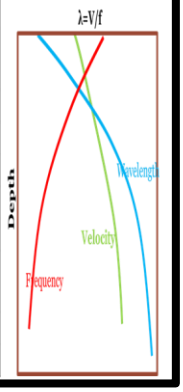


Figure 12: Vertical resolution and the depth versus frequency, velocity and wavelength which are specifically modified for Akçakoca 3D.

Velocity tends to increase with depth due to compaction and diagenetic effects. Frequency decreases due to attenuation of the seismic wave. There is an almost constant fractional energy loss per cycle of the seismic wave, and higher frequencies are attenuated more than lower frequencies for a particular path. Thus burial depth is inversely proportional to vertical and lateral resolution, and interference effects become more pronounced as the pulse length increases due to lower frequency.

3.2 Conventional Seismic Interpretation

Mapping geologic structures, stratigraphy and reservoir architecture is considered to be the main subject of the conventional seismic interpretation which is basically picking laterally traceable, consistent seismic reflectors or disrupted surfaces such as unconformity surfaces. The ultimate goal is to detect possible structures which may contain hydrocarbon accumulations, delineate their extent, and calculate their volumes. The geometrical expression of seismic reflectors is mapped in travel time since interpreted seismic simply consist of traces which are time function of amplitudes. Furthermore, proper time-depth conversion is need which is also part of the conventional workflow.

3.2.1 Surface Interpretation and Attributes

Amplitude is the most basic attribute of a seismic trace. In the past, the interest of interpreter to amplitude was just restricted to its presence on time or depth, not its magnitude as in that time seismic was popularly used only for structural analysis. Currently, the seismic data processing is generally directed to obtain "preserve true amplitude" so AVO, inversion and stratigraphic analysis can also be done. Although seismic amplitude is most frequently used to recognize hydrocarbon-related amplitude anomalies such as the bright-spots, dim spots, etc., however it can shed light on reservoir properties as well. The lateral changes of amplitude can be used to distinguish one facies with another. For instance, while the concordant beds tend to have relatively higher amplitudes, hummocky and chaotic beds are characterized by lower and the lowest amplitudes, respectively. The sand-rich environments usually have higher amplitudes compared to the shale-prone ones. These differences in sand-shale ratio and geometries can easily be analyzed in amplitude maps and interpreted as elements of a depositional environment.

The interpretation of lithologies and depositional architectures from seismic data is defined as seismic facies analysis. Spatially definable three-dimensional unit is called seismic facies which is composed of groups of seismic reflections whose parameters (configuration, shape, amplitude, continuity, frequency, phase and velocity) differ from the elements of adjacent facies (Mitchum et al., 1977). Basically, stratal surfaces, unconformities and fluid contacts are represented by seismic reflections. Interpretation of seismic facies involves consideration of internal reflection configurations, boundary relationships, lateral facies relationships and external geometry. Erosional unconformities create high amplitude reflections, and they are usually considered as diachronous surfaces because they commonly separate strata with different acoustic impedances. In addition, strata below an unconformity are commonly weathered or altered mineralogically which also creates acoustic impedance contrast (Brown and Fisher, 1980).

Seismic interpretation starts with picking certain reflection and making a time structure map of such laterally consistent reflection surface. In this point, there are two major issues before this reflection surface is interpreted as a "meaningful" geological surface. First, the time scale of this surface should be converted to depth in order to

have a depth structure map of the selected reflection surface. Second, depth structure map of the selected reflection surface should tie with the well data which is considered to be solid data.

3.2.2 Well Tie and Correlations

Well tie procedure relies on convolution method which is basically convolving sonic and density log values with a selected wavelet in order to generate a single normal incidence trace or a range of traces at different angles or offset synthetics (Figure 8) (Ziolkowski et al., 1998). Selected wavelet which ties seismic data to the well-based stratigraphic information is derived from both the seismic data and the well logs (White et al., 1980).

Well correlation can be done at different scales depending on the data involved in the correlations. Seismic only correlation might be considered as a large scale correlation where a set of well data which consists of logs, cuttings or cores can give a small scale high resolution correlation. Correlation can be designed depending upon the required detail and availability of the data sets.

3.2.3 Velocity Analysis and Modeling

The certain degree of accuracy at the velocity field over the study area is required for proper time-depth conversion. However, it has to be pointed out that this is an iterative procedure and there is no unique answer for the velocity. In order to start this iterative flow, one might start with a single velocity function which is defined by regional velocity information. Another good starting point might be the processing velocities over the survey area since these are picked densely and interpolated though each trace location. Wells consist of several data types such as electrical logs (compressional sonic, shear sonic, density, gamma ray etc.), cuttings and side-wall cores. After detailed preparation, processing and evaluation of each data set, several valuable data and information are derived from them such as fossils, ages, facies, depositional environment definitions, reservoir tops, reservoir properties etc. Since the sonic and density responses in a well are recorded with logs, these can be used to generate a synthetic response of the lithology tested at the well location. Well

synthetics should tie to the seismic at well location. In this point, two types of velocity information are revealed. First one is derived from the procedure of matching formation top (value in meters) with reflection surface (value in time), and propagate the related velocity through the surface. This gives you a constant velocity through the surface. Second one is a velocity function which is used for tying the seismic time section to depth values of the well. This velocity function is called *time-depth function*. Time-depth function can be interpolated through the surface and used for time depth conversion of either seismic or well data. As mentioned above, several types of velocity, velocity function or field can be derived from different ways but the important point is that these velocities should be combined into a velocity model. As soon as the proper velocity model conducted, the time domain seismic interpretation can be converted to depth. Moreover, depth-converted reflection surfaces are always supported by well data since the velocity model which is subjected to depth conversion is previously derived by well data itself.

3.2.4 Petrophysical Log Calculation and Evaluation

Several wireline logs are acquired at well locations. Available logs for each well used in this study are listed in figure 2. Some of the logs are used as input to estimate logs which are not acquired. Table 1 summarizes input logs, constants, and the formulas which give the output logs required for modeling.

Table 1 : Summary of calculated logs with derived formulas, constants and input logs with names and units.

INPUT LOGS	DT	Sonic Compressional	Observed	us/ft
	DT2	Sonic Shear	Observed	us/ft
	GR	Gamma Ray	Observed	API
	NPHI	Neutron Porosity	Observed	v/v
	RHOB	Density	Observed	g/cm^3
	RT	Resistivity	Observed	ohm.m
NUMERIC INPUTS	DTfld	205	Constant	us/ft
	Dtma	70	Constant	us/ft
	GRcln	40	Constant	API
	GRshl	60	Constant	API
	RhoF	1	Constant	g/cm^3
	RhoM	2.68	Constant	g/cm^3
	Rw	0.1	Constant	ohm.m
	Swirr	0.35	Constant	v/v
OUTPUT CURVES	DENSITY	Density	DENSITY=RHOB	g/cm^3
	DTC	Sonic Compressional	DTC=DT	us/ft
	DTS	Sonic Shear	DTS=DT2	us/ft
	GAMMA	Gamma Ray	GAMMA=GR_LOG	API
	PERM1	Tixier Permeability	PERM1 = (250 * PHIE^3/Swirr)^2	mD
	PERM2	Timur Permeability	PERM2 = (100 * PHIE^2.25/Swirr)^2	mD
	PERM3	Coates Permeability	PERM3 = (70 * PHIE^2 * (1- Swirr)/Swirr)^2	mD
	PHIA	Avarage Porosity	PHIA = ((RhoM - RHOB) / (RhoM - RhoF) + NPHI) / 2	v/v
	PHIE	Effective Porosity	PHIE= PHIA*(1-Vshl)	v/v
	BVW	Bulk Volume Water	BVW=PHIA*SwA	v/v
	R0	Archie R0	Ro = Rw/(PHIE^2)	ohm.m
	SoPhi	Hydrocarbon Pore Volume	SoPhi = (1-SwA) * PHIE	v/v
	SwA	Archie Water Saturation	SwA = Min(1,Max(0,(Ro / RT)^0.5))	v/v
	Vshl	Volume Shale	Vshl = min(1, max(0, (GR-GRcln) / (GRshl-GRcln)))	v/v

3.3 Quantitative Seismic Interpretation (QSI)

The seismic amplitudes, representing primarily contrasts in elastic properties between individual layers, contain information about lithology, porosity, pore-fluid type and saturation, as well as pore pressure information that cannot be gained from conventional seismic interpretation.

3.3.1 Rock Physics Analysis

Investigating reservoir properties and relating them to the seismic data is the main goal of the rock physics studies. Basically, in situ reservoir conditions are modeled by relating velocity and impedance to porosity and mineralogy. Revealed

relations can be distributed through the seismic survey in order to generate several reservoir property maps.

Sedimentary rocks (sandstones, shales, limestones etc.) can be considered as sets of grains. The space between the grains is called *pore space*. At reservoir conditions, the pore space is filled with oil, water or gas each of which is considered as pore fluid. *Pore pressure* is the fluid pressure in the pore space. For a case with perfect communication between the pores, the pore pressure is equal to the *hydrostatic pressure* which is produced by the weight of the fluid. Hydrostatic pressure is often referred to as *normal pressure*. Rocks that deviate from the hydrostatic pressure are either called *over-pressured* or *under-pressured* depending on whether the pressure is greater or less than the normal pressure.

Velocity-porosity relation is conventionally used for mapping porosity and facies at reservoir level. Mavko et al. (1998) reviews effective elastic moduli of rocks and sediments. Upper and lower bounds of the elastic moduli of rocks provide useful velocity-porosity relations which are also essential for the fluid substitution. The most common bounds are *Voigt upper* and *Reuss lower* bounds. Voigt upper bound is the arithmetic average of the rock moduli and defines the stiffness boundary (Voigt, 1928). Reuss bound is the harmonic average of the rock moduli and defines the softness boundary (Reuss, 1929). P-wave velocity versus porosity cross plot is depicted by Avseth et al. (2005) for several water saturated sediments starting from ocean bottom suspensions to consolidated sandstones (Figure 12).

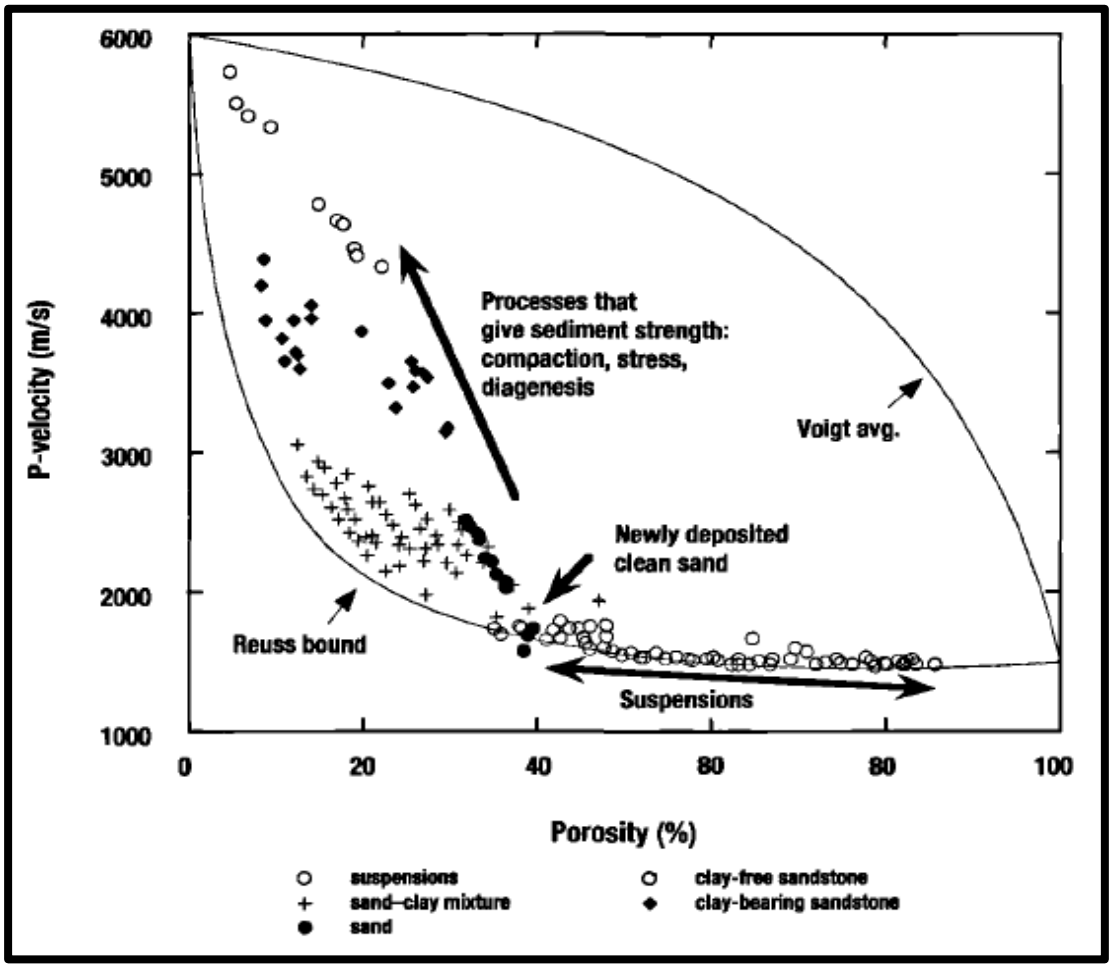


Figure 13: P-wave velocity versus porosity cross plot for several water saturated sediments starting from ocean bottom sandstone to consolidated sandstone (Avseth et al., 2005).

Fluid substitution is another commonly used rock physics method in oil and gas industry in order to understand the possible effect of pore fluids on seismic velocity and impedance. Gassman's (1951) relations allow predicting changes of rock modules when the pore fluid properties change. The *rock bulk density* and *compressibility* are two parameters which might change due to fluid effect. Compressibility of the dry rock is simply represented by the sum of the mineral and pore space compressibility (Avseth et al., 2005) as shown in equation 3.3.

$$\frac{1}{K_{dry}} = \frac{1}{K_{mineral}} + \frac{\phi}{K_{\phi}}$$

3. 3

Where ϕ is the porosity, K_{dry} is the dry rock bulk modulus, $K_{mineral}$ is the mineral bulk modulus, and K_{ϕ} is the pore space stiffness defined by:

$$\frac{1}{K_{\phi}} = \frac{1}{v_{pore}} \frac{\partial v_{pore}}{\partial \xi}$$

3. 4

v_{pore} is the pore volume, and ξ is the increment of hydrostatic confining stress from the passing wave. Soft and compressible rocks or rocks at low effective pressure are generally represented with small K_{ϕ} (Avseth et al., 2005). Stiff and less compressible rocks or rocks at high effective pressure such as well cemented rocks have higher K_{ϕ}. Compressibility of saturated rocks can be expressed as

$$\frac{1}{K_{sat}} = \frac{1}{K_{mineral}} + \frac{\phi}{K_{\phi} + \frac{K_{fluid} K_{mineral}}{K_{mineral} - K_{fluid}}}$$

3. 5

or can be approximated as

$$\frac{1}{K_{sat}} \approx \frac{1}{K_{mineral}} + \frac{\phi}{K_{\phi} + K_{fluid}}$$

3. 6

where K_{fluid} is the bulk modulus of pore fluid. In this point, it can be easily seen that changing the pore fluid has the effect of changing stiffness at pore space. The stiffness value of pore space is inversely proportional to degree of fluid sensitivity. For instance, a soft and compressible rock is highly sensitive to fluids or vice versa. Gasmann's relations describe these effects in a simple and reliable way. Equation 3.2 and 3.4 together are equivalent to Gassmann's (1951) relations. It can be shown in short by eliminating K_{ϕ} from the equation,

$$\frac{K_{sat}}{K_{mineral} - K_{sat}} = \frac{K_{dry}}{K_{mineral} - K_{dry}} + \frac{K_{fluid}}{\phi(K_{mineral} - K_{fluid})}$$

3. 7

and the results can be extended to,

$$\mu_{sat} = \mu_{dry}$$

3. 8

Gassmann's equations predict that for an isotropic rock, the rock bulk modulus change when the fluid changes, however the rock shear modulus do not change due to fluid.

As we see it in the velocity-porosity crossplot, more separation can also be seen at Vp vs Vs crossplot due to fluid effect at pore space. Castagna et al. (1993) provides a good review of the Vp-Vs relation for different lithologies. Several empirical relations exist in the literature including famous "mudrock line" of Castagna et al. (1985) and Greenberg – Castagna relations at Greenberg et al. (1992).

An extremely important group of reflectors originate from acoustic impedance change that is not directly related to lithological change. These are the reflections associated with hydrocarbons. The presence of gas in a reservoir often produces a detectable suite of responses in the seismic record, and it is obviously very important for the interpreter to be able to recognize these gas effects. There are several criteria such as acoustic impedance, velocity, frequency effects etc., which might help recognizing the presence of gas in seismic data.

The way in which a reservoir responds to the presence of gas depends on the acoustic impedance of the gas-filled reservoir interval, the water-filled reservoir interval, the cap rock interval and the thickness of the gas-filled interval. If the reservoir gas column is thick enough, and there is an acoustic-impedance contrast between the gas-oil or gas-water filled reservoir interval, impedance responses likely to be found in porous sandstone.

Although other impedance related diagnostics exist between the cap rock and gas-bearing reservoir, the best indication of gas is called *flat spot*. Anomalies of very high amplitude are commonly called *bright spots*, and anomalies of very low amplitude are commonly called *dim spots*. Any local change of reflection strength that does not appear to have its origin from the lithology may be considered as hydrocarbon anomaly. Gas related bright spots are usually associated with porous sands; however

dim spots due to a reduced reflection coefficient of the top-reservoir reflector are more common with less porous or well-compacted sandstone reservoirs. In such cases, the claystone/compacted-sand would usually have a strong positive reflection coefficient. The reflection coefficient is reduced by the presence of gas in the reservoir; hence the top reservoir reflector loses its amplitude and gets dimmer. Amplitude anomalies are sometimes accompanied by corresponding polarity changes. A polarity reversal of the top reservoir reflector at the gas-oil or gas-water contact is a common feature of bright spots.

Velocity typically follows a decreasing trend when the gas column is sufficiently thick enough which may also cause a push-down effect in underlying reflectors.

Sometimes, a significant frequency loss appears beneath a bright spot location. This phenomenon has been attributed to greater absorption of the seismic wave within gas-bearing as opposed to water-bearing intervals. This absorption selectively depletes the signal of higher frequencies of the observed data.

Amplitude and velocity anomalies do not always infer the presence of gas. Moreover, not all of them are economically valuable such as low (as low as 5%) gas saturation can produce a detectable amplitude anomaly at porous sand interval. Carbonates, igneous intrusion or thinning beds at tuning thickness can also produce high amplitude anomalies which are not directly related to hydrocarbons. Finally, diagenetic effects can also generate flat spots.

3.3.2 Amplitude vs. Offset (AVO)

Certain Amplitude Variation with Offset (AVO) responses of seismic reflections are interpreted as direct hydrocarbon indicators which have made the AVO method one of the major prospecting tools in hydrocarbon exploration. Several AVO parameterizations which are combinations of three elastic constants exist (Russell et al., 2011). The following equations were derived by Zeoppritz (1919) which calculate the amplitudes for reflected and transmitted plane waves.

One of the basic assumptions about seismic data is that the seismic wave strikes the rock interfaces at normal incidence. In this case, the reflection coefficient is given by following equation 3.9:

$$RC_i = \frac{Z_{i+1} - Z_i}{Z_{i+1} + Z_i} \qquad 3.9$$

where, Z is acoustic impedance and i is the layer.

The variation of amplitude with offset is also affected by the Poisson's Ratio. The formula for Poisson's ratio is given by the following equation 3.10:

$$\sigma = \frac{1}{2}\frac{(\frac{V_p}{V_s})^2 - 2}{(\frac{V_p}{V_s})^2 - 1} \qquad 3.10$$

Theoretically, the Poisson's ratio can vary between 0 and 0.5 and is close to 0 for gas and is 0.5 for a liquid. From equation 3.10, it is obvious that when the Poisson's ratio approaches 0.5, the Vp/Vs ratio goes to infinity. This is because the S-wave velocity is zero in fluids. On the other hand, the Vp/Vs ratio = $\sqrt{2}$ when the Poisson's ratio is 0. Schoenberg (1980) suggested that a parameter can be used to simplify the transformation from velocity to Poisson's ratio is $\sigma = (Vp/Vs)^2$.

As mentioned before, the equations which determine the amplitude variations as a function of offset are dependent on P-wave velocity, Poisson's ratio, and density. They are derived from the continuity of displacement and stress in both the normal and tangential directions across an interface between two layers by Zeoppritz (1919). Equation 3.2 gives the final form of the Zeoppritz equations.

There are several approximations to Zeoppritz's equations in order to understand how these amplitudes are related with the various physical parameters. For analyzing of P-wave reflections, the requirement is an equation which relates reflected P-wave amplitudes to incident P-wave amplitudes as a function of the angle of incidence (Smith and Gidlow, 1987). Following Russell et al. (2011), the Aki and Richard's (1980) approximation is expressed as a linearized sum of three terms given by:

$$R_{PP}(\theta) \approx (1 + tan^2\theta)\frac{\Delta V_P}{2V_P} + \left(\frac{-8sin^2\theta}{\gamma_{sat}^2}\right)\frac{\Delta V_S}{2V_S} + \left(1 - \frac{4sin^2\theta}{\gamma_{sat}^2}\right)\frac{\Delta\rho}{2\rho}$$

3. 11

Smith and Gidlow (1987) rearranged Aki-Richard's equation in the following way:

$$R_{PP}(\theta) \approx A + Bsin^2\theta + Ctan^2\theta sin^2\theta$$

3. 12

where $A = R_{P0} = \frac{1}{2}\left[\frac{\Delta V_P}{V_P} + \frac{\Delta\rho}{\rho}\right]$ is a linearized approximation to the zero offset P wave reflection coefficient, $B = \frac{\Delta V_P}{2V_P} - \frac{8}{\gamma_{sat}^2}\frac{\Delta V_S}{2V_S} - \frac{4}{\gamma_{sat}^2}\frac{\Delta\rho}{2\rho}$, and $C = \frac{\Delta V_P}{2V_P}$ (Russell et al., 2011).

Equation 3.12 is rearranged by Gidlow et al., 1992 and Fatti et al., 1994 in the following equation,

$$R_{PP}(\theta) \approx (1 + tan^2\theta)R_{P0} + \left(\frac{-8}{\gamma_{sat}^2}sin^2\theta\right)R_{S0} + \left(\frac{4}{\gamma_{sat}^2}sin^2\theta - tan^2\theta\right)R_D$$

3. 13

One of the earlier case studies published by Koefoed (1955) shows angle dependent variation in the P-wave reflection coefficient due to the Poisson's ratio. Rutherford and Williams (1989) realized that it was possible to discriminate the gas sands from overlying shale facies due to their acoustic impedance responses. Universally adopted classification system for AVO responses has been recognized by oil and gas exploration industry after their work (Foster et al., 2010). These early works showed that identifying hydrocarbon-related changes on the acoustic impedance and Poisson's ratio of reservoir sands requires a certain degree of development in seismic attributes in order to detect such effects (Foster et al., 2010). Several AVO attributes have been developed, and some common attributes are listed as intercept of normal-incidence reflection coefficient; gradient of normal incidence reflection-coefficient; P-wave normal-incidence reflectivity which is equivalent to intercept; and S-wave normal incidence reflectivity. Most of these attributes originate with Aki and Richards'

(1980) approximation for the angle-dependent P-wave reflection coefficient (Foster et al. 2010).

The development of methods to obtain various fluid factors from pre-stack seismic data has pushed the development of technology for reservoir forecasting and fluid discrimination (Smith and Gidlow, 2000; Quakenbush et al., 2006; Zong et al., 2012). Traditional AVO and petrophysical analysis seeks to identify anomalous variations between seismic compressional wave velocity (V_p) and shear wave velocity (V_s) to indicate changes primarily in pore fluid, as well as lithologic properties (Goodway et al., 1997; Gassmann, 1951; Pickett, 1963; Tatham, 1982; Castagna, 1993).

3.3.3 Seismic Amplitude Inversion

Converting seismic reflectivity data to models of elastic properties of the subsurface is called *inversion*. The seismic amplitude inversion is basically an inverse modeling, where the input is the seismic record that is inversely modeled into the acoustic impedance (Z) section. Inverse modeling algorithm is basically a deconvolution between the seismic records and seismic wave which then produces the Z section. Basic inputs for inversion are seismic volume, well logs and estimated wavelets. Amplitude inversion methods (Figure 13) can be classified as post-stack and pre-stack amplitude inversion.

Post amplitude inversion methods can be subdivided into three main methods. First one is *recursive inversion* which is considered as the simplest inversion method. Recursive inversion is based on the equation 3.9 and 3.14. Seismic data is assumed to be equal to the density-velocity model and inversed by using the inversed relation in equation 3.14 which is first proposed by Lindseth (1979).

$$Z_{i+1} = Z_i(1 + RC_i)/(1 - RC_i) \tag{3.14}$$

For the nth layer case:

$$Z_n = Z_1 \prod_{i=1}^{n-1} (1 + RC_i)/(1 - RC_i) \tag{3.15}$$

From this equation, a non-linear relation between impedance and reflectivity is seen. Z_1 is the impedance of the first layer. At least one impedance value is required in order to compute the impedance profile from the reflectivity. For small reflection coefficients (RC < 0.2), linear approximation is possible, and it shows the limitation of the inversion methods as well.

The lack of geologic control is the main weakness of this technique and, therefore, it is almost identical to the forward modeling. The correct wavelet is assumed as zero phase wavelet which affects the resulted geology model. Low and high frequency components from Earth reflectivity which are lost when the reflectivity is convolved with the selected wavelet are also difficult to be recovered with this technique, so the ability of lateral prediction of the Z is limited. Recursive inversion also ignores the seismic wavelet effect and treats the seismic trace as an RC series which is filtered by zero phase wavelet. The recursive inversion equation also assumes that the absolute scaling of RC value is correct. Because the equation is applied recursively from top to bottom, the error effect will be accumulated. The noise in seismic trace will be interpreted as a reflection and involved in the inversion.

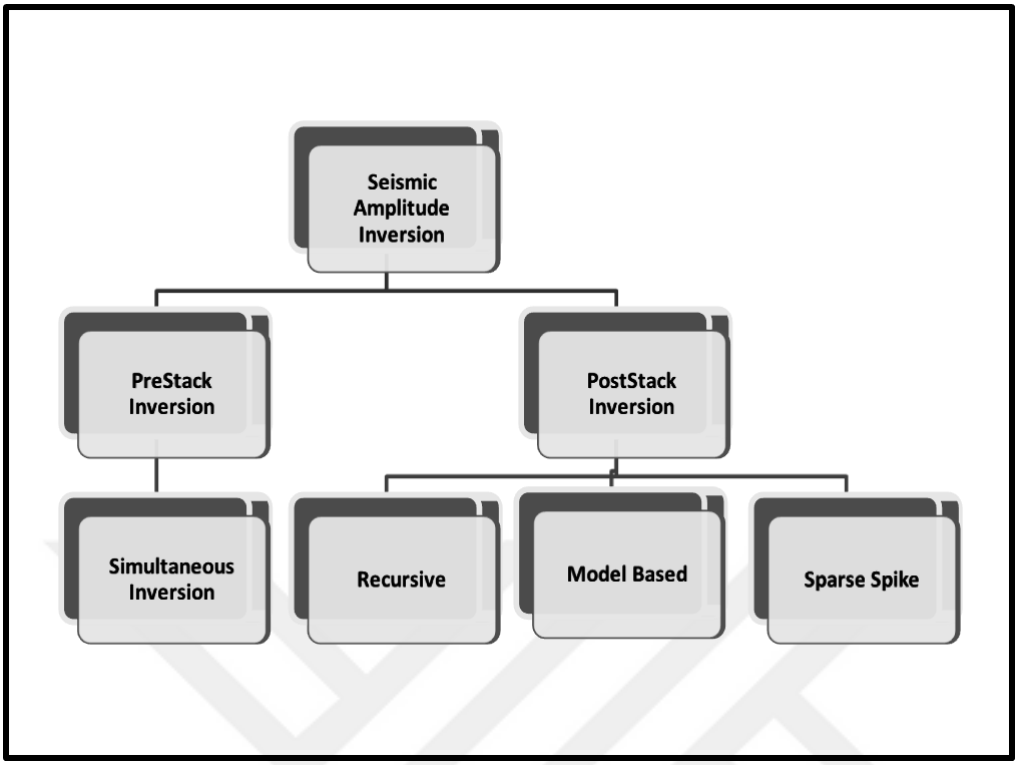


Figure 14: Seismic amplitude inversion methodologies.

Model based inversion approach iteratively changes a model to give a least-squares fit to the seismic data (Russell and Hampson, 1991). Model based inversion is also based on deconvolutional model but it starts with an initial geologic model. Basically, synthetic trace is subtracted from the real trace and the result is the error between the real trace and the modeled one. Acoustic impedance values are changed with several iterations until the results reach an acceptable error range. It is sensitive to the initial model quality and the seismic quality.

Sparse-spike method assumes a certain model of the reflectivity and estimates the wavelet based on this model assumption. It has an advantage over classical methods of deconvolution because the sparse-spike estimate, with extra constraints, can be used as a full bandwidth estimate of the reflectivity. Sparse spike method uses three statistical solutions; first one is maximum-likelihood, second one is Norm L1

and finally minimum entropy. The sparse-spike inversion considers only the higher magnitude spikes. The method locates the higher magnitude spikes by checking the seismic trace. Reflectivity series reconstruct one spike each at a time. The spike is added until the trace is modeled at a range of acceptable accuracy. Each added spike which is smaller than previous one contributes the accuracy of model trace.

Simultaneous inversion starts with the equation 3.13 derived by Fatti et al. (1994). This equation models amplitudes of reflection as a function of incident angle. A linear relationship is assumed for the background saturated lithologies. Combining the model-based inversion approach with the Fatti's equation gives an extended version of the zero offset model (Hampson et al., 2005) which can be written as;

$$R_{PP}(\theta) \approx c_1 R_{P0} + c_2 R_{S0} + c_3 R_D$$

3.16

Where: $c_1 = (1 + tan^2\theta)$, $c_2 = \left(\frac{-8}{\gamma_{sat}^2} sin^2\theta\right)$, $c_3 = \left(\frac{4}{\gamma_{sat}^2} sin^2\theta - tan^2\theta\right)$, $\gamma = \frac{V_S}{V_P}$

$R_P = \frac{1}{2}\left[\frac{\Delta V_P}{V_P} + \frac{\Delta \rho}{\rho}\right]$ is equal to the A term from equation 3.12, $R_S = \frac{1}{2}\left[\frac{\Delta V_S}{V_S} + \frac{\Delta \rho}{\rho}\right]$ is the linearized approximation to the S wave impedance reflectivity, and $R_D = \frac{\Delta \rho}{\rho}$ is the linearized density reflectivity term (Russell et al., 2011).

$$R = MP \rightarrow \begin{bmatrix} R_{PP}(\theta_1) \\ R_{PP}(\theta_2) \\ \vdots \\ R_{PP}(\theta_N) \end{bmatrix} = \begin{bmatrix} c1(\theta_1) & c2(\theta_1) & c3(\theta_1) \\ c1(\theta_2) & c2(\theta_2) & c3(\theta_2) \\ \vdots & \vdots & \vdots \\ c1(\theta_N) & c2(\theta_N) & c3(\theta_N) \end{bmatrix} \begin{bmatrix} R_P \\ R_S \\ R_D \end{bmatrix}$$

3.17

$$P = \begin{bmatrix} R_P \\ R_S \\ R_D \end{bmatrix} = (M^T M + \lambda\, I)^{-1} M^T R$$

3.18

Before a simultaneous approach to inversion is derived, small reflectivity approximation needs to be visited.

Small reflectivity approximation $R_i \approx \frac{\Delta ln Z_i}{2}$ for (R < 0.1) allows us to rewrite impedance vs. reflection coefficient relation as R=DL, where: D= the difference

matrix. Writing L=ln(Z), the reflectivity can be derived from the logarithm of impedance using the matrix operation given by:

$$\begin{vmatrix} R_1 \\ R_2 \\ \vdots \\ R_{N-1} \end{vmatrix} = \begin{bmatrix} diff(\theta_1) & diff(\theta_1) & diff(\theta_1) \\ diff(\theta_2) & diff(\theta_2) & diff(\theta_2) \\ \vdots & \vdots & \vdots \\ diff(\theta_N) & diff(\theta_N) & diff(\theta_N) \end{bmatrix} \begin{bmatrix} L_1 \\ L_2 \\ \vdots \\ L_N \end{bmatrix}$$

3.19

Now, the model based inversion approach can be combined with Fatti's equation in order to have an extended version of a zero offset model (Hampson et al., 2005).

$$S(\theta) = c_1 W(\theta) DL_P + c_2 W(\theta) DL_S + 2c_3 W(\theta) DL_D$$

3.20

Where: $S(\theta)$= seismic trace at angle θ, $W(\theta)$= the extracted wavelet at angle θ.

Following equations relate the products of R_S and R_D to R_P,

$$L_D = mL_P + m_c + \Delta L_D$$

3.21

$$L_S = kL_P + k_c + \Delta L_S$$

3.22

Combining equation 3.20, 3.21 and 3.22, equation of simultaneous inversion can be finalized as (Hampson et al., 2005).

$$S(\theta) = \tilde{c_1} W(\theta) DL_P + c_2 W(\theta) D\Delta L_S + c_3 W(\theta) D\Delta L_D$$

where: $\tilde{c_1} = c_1 + kc_2 + mc_3$

3.22

Initial model consists of the P-impedance model and deviations away from background trends for both the S impedance and the density.

Equation 3.22 can be written as S=ML and solved as

$$L = (M^T M + \lambda\, I)^{-1} M^T S$$

3.23

The pre-stack inversion method is based on angle gathers, and it calculates the elastic impedance of P wave (PI), S wave (SI) and density simultaneously. The inversion workflow begins with the conversion of well data from depth to time, and

the use of calibrated wells and different angle stacks to derive wavelets. To guide and constrain the interpolation of reservoir properties during simultaneous inversion, a prior low frequency model is generated by laterally extrapolating filtered well log data, using seismic horizons and interval velocities as constraints. Then the inversion is executed, which produced three outputs: PI, SI, and density. Observed and inverted PI and SI should exhibit a good match with measured logs.

3.3.4 Forward Modeling

Forward modeling is based on the convolutional model which simply represented by a seismic trace. Equation 3.24 shows the basic concept. In general, noise (N) is not included to the model.

$$Seismic\ trace\ (S) = Wavelet\ (W) * Earth's\ Reflectivity(R) + Noise\ (N)$$

3.24

Matrix equation of the 3.24 can be written as,

$$S = WR \rightarrow \begin{vmatrix} S_1 \\ S_2 \\ \vdots \\ S_N \end{vmatrix} = \begin{bmatrix} W_1 & 0 & \cdots & 0 \\ \vdots & W_1 & \ddots & \vdots \\ W_K & \vdots & W_1 & 0 \\ 0 & W_K & \vdots & W_1 \\ \vdots & \ddots & W_K & \vdots \\ 0 & \cdots & 0 & W_K \end{bmatrix} \begin{vmatrix} R_1 \\ R_2 \\ \vdots \\ R_M \end{vmatrix}$$

3.25

N=K+M-1 where N is the output length, K is the wavelet length and M is the input length.

Simulated facies and petrophysical properties are used in order to predict Earth's reflectivity. Convolving them with the proper wavelet gives a normal incidence synthetic. There are certain assumptions which avoid complications on the synthetic models such as no modeled multiples are included, transmission loss and geometric spreading are ignored, frequency dependent absorption is ignored, and shape of wavelet might be time varying.

The aim of running forward model at well location is to observe amplitude sensitivity of the simulated facies and petrophysical properties. Moreover, the set of wells are reserved for blind test and are not involved in any of the simulations.

Therefore, the match between simulation results and observed values at the blind well locations purely reflects the power of simulation for facies and properties.

3.4 Deep Water Facies

The study of deep water systems within deep offshore may require many different remote-observation techniques, each of which can provide information on just one part since the entire system can reach hundreds of kilometers long in length. The major challenge in analyzing deep water depositional systems is the integration of multiple data types including outcrop studies, 2D and 3D seismic data, cores, logs, bio-stratigraphy and well-test.

Kuenen and Migliorini (1950) was the first who defined the process of deep water deposits (Mutti et. al. 2009). They advanced the concept of turbidity currents as an important process by which sediment is transported from shallow water environment to deep water environment. The first indirect evidence of existing turbidity currents was periodic breakages of deep-ocean (water depth is more than 250 m) seafloor communication cables in the early 20^{th} century at Grand Banks of Newfoundland, offshore eastern Canada (Heezen and Ewing, 1952, Shanmugam, 2000). Later on, pioneering work by Bouma (1962), Mutti (1972), and Normark (1978) provided early geologic models for submarine fans and their component strata (Figure 14).

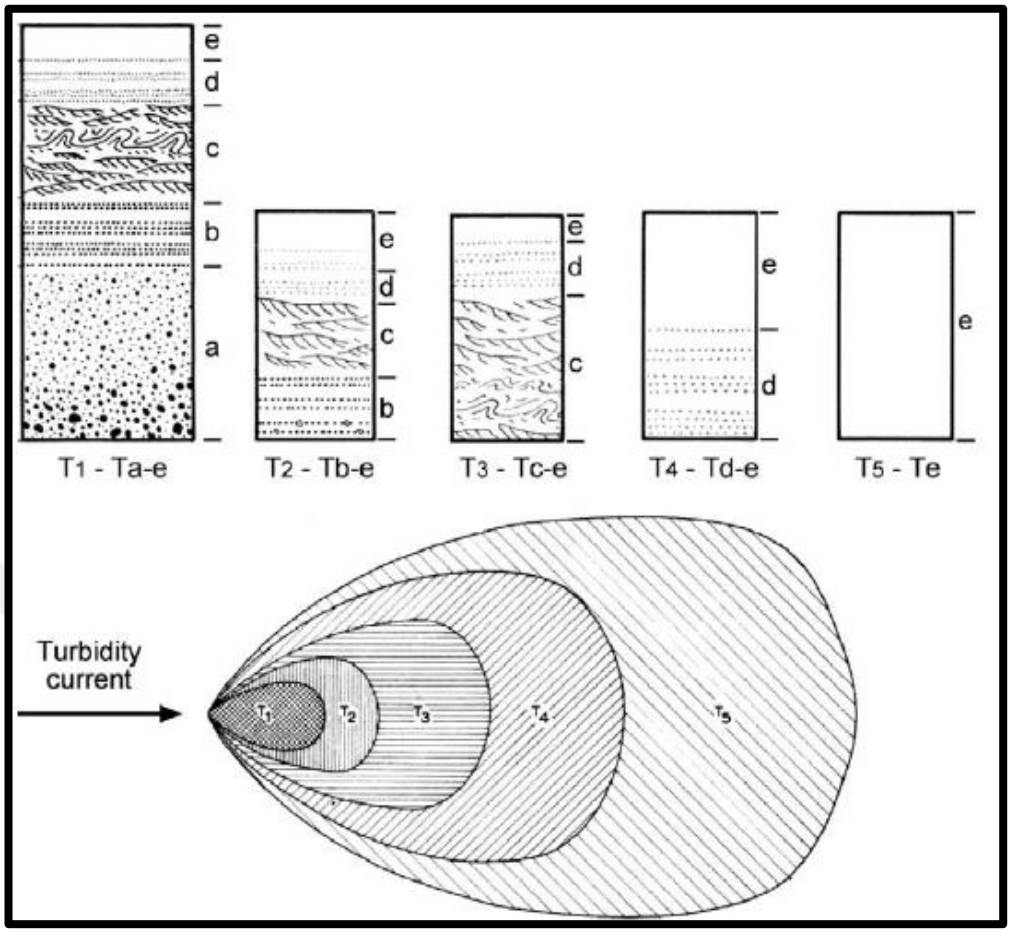


Figure 15: The Bouma sequence and its 'depositional cone' (from Bouma, 1962). (taken from Mutti et. al. 2009).

Turbidity currents take form when a small volume of subaqueous sedimentary particles, relative to the total volume of water, move downslope under the influence of gravity. Because fluid is the dominant component, the flow becomes turbulent and remains turbulent as it travels downslope (Shanmugam, 2000). In addition to turbidity currents, a variety of types of sediment gravity flows distribute sediment into deep water (Shanmugam, 2000). These flows behave according to the interactions of the individual particles in the flow. At low sediment concentrations, turbulent, fluidal flow predominates. With higher concentrations of sediment, the grains interact more

frequently, and different mechanisms keep the grains moving within the flow (Shanmugam, 2000).

Mutti (1985) introduced the concept of turbidite elements, which emphasized three main sand-bearing architectural elements: sheets (layered and amalgamated), channels (single and multistory with an erosional feature), and thin beds (aggradational) in levee sediments. This descriptive classification of the architectural elements of deep water systems is commonly used in the oil and gas industry (Figure 15).

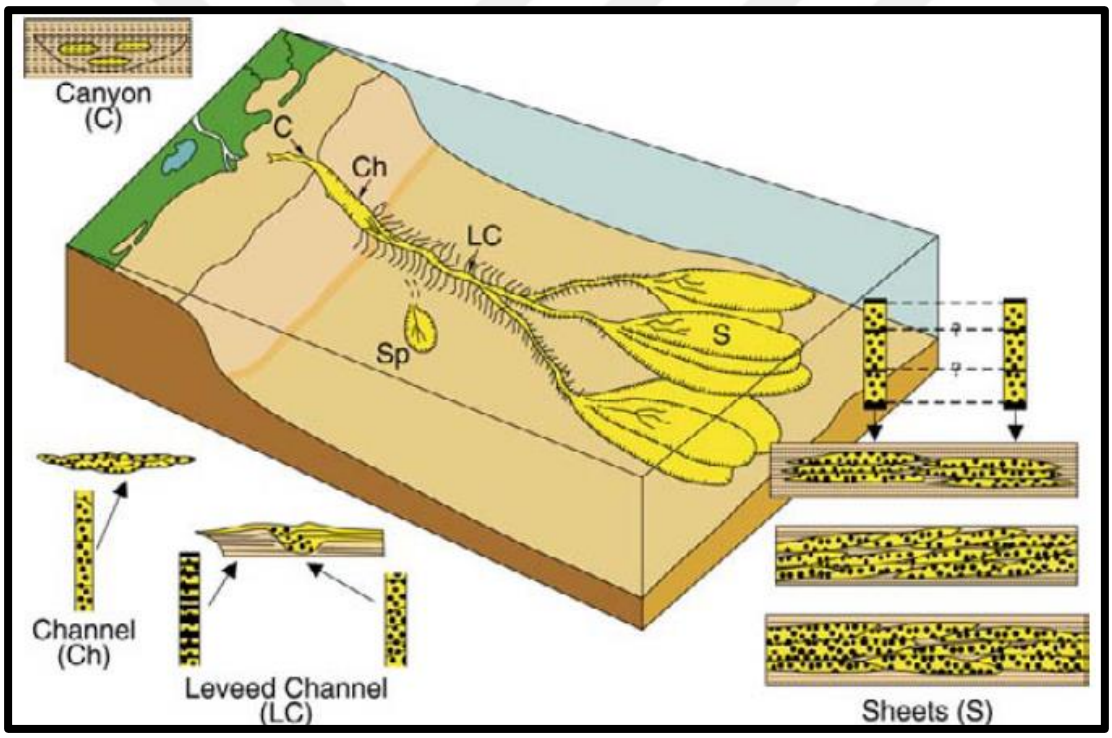


Figure 16 : Schematic diagram of the architectural elements of fine-grained deepwater depositional systems. (Stratigraphic Reservoir Characterization, Slatt, 2006).

Walker (1978) attempted to combine models into a comprehensive submarine-fan model composed of a feeder canyon, a proximal suprafan lobe, and a more distal lobe fringe, all sitting on a basin-plain deposit (Figure 16). According to this model, the grain size of the sediments decreases progressively basinward which suggests that the potential for oil and gas reservoirs also diminishes in that direction. This model was the standard for many years up to the introduction of new 2D and 3D seismic-reflection technologies which revealed that the model was too simplified. Later on Walker (1992) stated that one model could not fit all deep water systems. As a result of recent developments in 3D seismic-reflection acquisition and processing technologies which further enhance imaging of detailed stratigraphic and facies relationships in 3D space, it has been possible to develop verifiable insights into the complex processes and deposits of deep water environments.

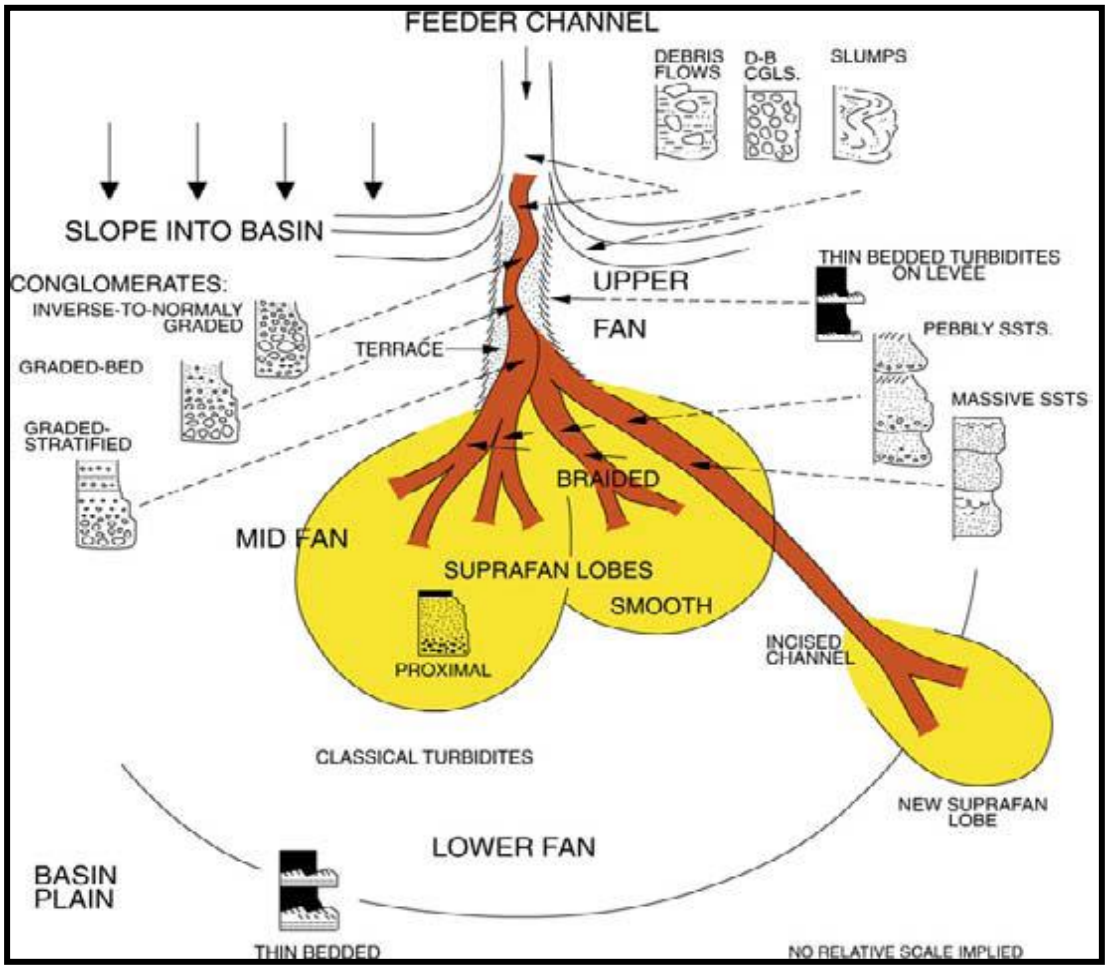


Figure 17 : Generalized submarine-fan model of Walker (1978) (From Stratigraphic Reservoir characterization by R.M. Slatt).

The concept of suprafan lobes with mounded seismic forms had its influence in seismic sequence stratigraphy. Application of the suprafan concept to the Paleocene sands was done by Sarg and Skjold (1982), and they mapped eight distinct suprafan lobes with mounded seismic geometries. Each individual mound was interpreted as a suprafan lobe containing an inner fan with fining upward channelized deposits and an outer fan fringe with coarsening upward sheet sands (Sarg and Skjold, 1982). Later on, Mitchum (1985) introduced a general seismic model for ancient fans which consisted of an upper and a lower fan. Mounded seismic facies and sheet-like turbidite sandstones of depositional lobes were equated by Mitchum (1985). In Mitchum's

(1985) model, a lobe is considered to exhibit mounded external form and bidirectional downlap, suggesting that the lobe is fully developed and has well defined outer limits. In a sequence stratigraphic framework, the lowstand systems tract is composed of the basin floor fan, the slope fan and the prograding wedge. In short, the basin floor fan concept is nothing but a combination of Normark's (1970) suprafan lobe concept and Mutti and Ricci Lucchi's (1972) depositional lobe concept. However there is an important distinction between fan models of sedimentology and sequence stratigraphy. In sedimentologic fan models, channels and lobes are contemporaneous elements. On the other hand, leveed fan channels are part of the slope fan, and are therefore younger, and not coeval with the lobes which are part of the older underlying basin floor fan in sequence stratigraphic models.

3.5 Geostatistical Simulations

Danie Krige (1951)'s early attempt of forecasting properties away from the known location was the starting points at geostatistical techniques. Introduced linear regression method is called Kriging. Kriging produces two powerful results one of which is accurately defined least squares regression values, and other one is the conditional cumulative distribution function (ccdf). Therefore, kriging is commonly used to estimate the probability of distribution, or single location uncertainty. Three common versions of kriging are *Simple Kriging* (SK), where the mean of the attribute in question is considered to be constant over a study region, *Ordinary Kriging* (OK), where local variation in the mean of the attribute in question is accounted for, and *Indicator Kriging* (IK) where the attribute in question is apportioned by a series of thresholds into classes (Deutsch, 1996). Kriging is used both for continuous data (attributes such as mineral grades, porosity, and permeability) and categorical data such as lithology. Main problem with the kriging is the full spatial and statistical variability of the sample represented by the single realization. Estimation process includes smoothing effect which is minimal at the locations where the estimated data and the observed data are close to each other. In contrary, at the locations were the distance between estimated data and the observed data are far away from each other than smooth effect increases.

Compared to kriging, conditional simulation is an advance in characterizing the spatial variation of earth variables such as lithology. The simulation approach takes into account not only the spatial variation of observed data at sample locations but also the variation in estimates at unsampled locations (Deutsch, 1996).

Vann et al., 2002 provides a summary of the development of these techniques. Numerous simulation techniques have been developed over the years and as they are computationally expensive their growth can be aligned with the increased availability and power of computers.

Simulation methods under the assumption of multi Gaussian random functions can be listed as covariance matrix decomposition, turning bands, Sequential Indicator Simulation (SIS), Sequential Gaussian Simulation (SGS), Truncated Gaussian Simulation (TGS) and the more complex Plury-Gaussian Simulation (PGS).

Categorical data, such as rock types (lithotypes), can be modeled using a variety of algorithms. Indicator kriging (IK) was introduced by Journel (1983) and for a considerable time was one of the most widely applied grade estimation techniques in the mining industry. The original appeal of IK was non-parametric, and it made no assumptions about the distribution underlying the sample data (Vann et al. 2002). The basis of the indicator approach is the binomial coding of data into either 1 or 0 depending upon its relationship to a cut-off value, resulting in a non-linear transformation of the data values (Vann et al. 2002). A benefit for continuous data is extreme values take the same indicator value as data close to the cut-off, thus limiting the effect of very high values in the kriging process. The outcome of IK is a conditional cumulative distribution function (ccdf) which is a distribution of local uncertainty or possible values conditional to data in the neighborhood of the block or cell to be estimated. There are two requirements which may not be met by IK results. One is cumulative distribution at a block should be non-decreasing. Second, the results should be valued between 0 and 1. Several methods have been proposed to overcome this issue, including direct correction of the indicator values (eg. Deutsch and Journel, 1998), using nested indicator variables (Dagbert and Dimitrakopoulos, 1992) and probability kriging (Isaaks, 1984) which is indicator co-kriging between the indicator-transformed data and a uniform transform of the sample data. The indicator transform

is simply the estimation of categorical data such as lithotypes. In this case, instead of kriging indicators at a set of thresholds, categorical IK will produce the probability of a given rock type at a given location producing probability maps of given rock types. Lloyd and Atkinson (2001) suggest that adaptation of the variogram for IK to local variation would increase the accuracy of the estimations by resolving the problem of changing means and variograms across the study area and this approach has been formalized by the conditional simulation.

Sequential indicator simulation (SIS) is considered to be a non-parametric algorithm which requires the binary transformation of continuous (eg. porosity or permeability) or categorical (eg. rock type) data into a series of indicator variables (Goovaerts, 1997, Deutsch and Journel, 1998). It applies IK in a sequential fashion where a precise category is drawn by Monte Carlo simulation at each location following a random path through the three dimensional grid. Individual grid nodes are simulated one after another, using continually updated conditioning data sets, and the conditioning data set includes the original data set and all previously simulated values within a specified range. This process ensures that closely spaced values have the correct short scale correlation as described in detail by Srivastava (1994). Deutsch (1996) used SIS in a categorical context and compared numbers of SIS algorithms, but noted two common criticisms of the technique: the models produced could appear very patchy and unstructured, and SIS often leaded to uncontrolled and unrealistic transitions between categories. Li and Zhang (2007) pointed out that SIS models did not follow interclass relationships in simulation maps.

The Sequential Gaussian simulation (SGS) is an efficient method widely used in the industry. The algorithm defines a random path through all grid nodes including the conditioning samples as well. Simple kriging of the nodes in the path helps generating a local distribution. A new value is then drawn from this local distribution. This is added to the nodes in the random path and the next node is simulated (Lantuejoul, 2002).

Aforementioned simulation techniques are well suited to petroleum reservoir simulation. They have several applications for facies simulation as well as reservoir properties such as porosity, permeability, or water saturation. Several authors

described reservoir characterization using geostatistical approaches that integrates seismic data and electrical logs. Doyen (1988) generated porosity map by cokriging 3-D seismic data with log data. Lucet and Mavko (1991) maps porosity by cokriging cross-well velocity tomogram with porosity logs. Kriging with an external drift, collocated cokriging, and Gaussian simulation to integrate 3-D seismic data and log data for the mapping of a salt dome is discussed by Journel, et al (1992). Tonn (1992) estimates the reservoir quality from complex trace attributes such as instantaneous amplitude, instantaneous phase, and instantaneous frequency generated by a 3-D seismic data.

Moreover, several papers have been published which mostly relating to the use of soft secondary data such as geological interpretation or geophysical measurements (Gomez-Hernandez and Srivastava, 1990; Goovaerts, 1997). Models of IK and SIS are both non-parametric which implies that they have no predetermined underlying model. Many simulation algorithms make purely mathematical assumptions that such an underlying model theoretically exists, and a popular set of these models use the Gaussian function as its basis.

CHAPTER 4

RESULTS OF THE STUDY

4.1 Conventional Seismic Interpretation of the Study Area

4.1.1 Surface Interpretation and Attributes

Akçakoca production field is located to the south western part of the offshore Black Sea. The primary reservoir in the field is the Eocene Kusuri Formation. Major reservoir levels are present within the Akcakoca member of the Kusuri Formation, which is composed of deep marine turbiditic sandstone and shale facies. Reservoir sandstones vary in thickness from 2-20m, with net to gross ranging from 20% to 80%. For such a heterogeneous turbiditic system, correlation of shales and turbiditic sandstones possess a major challenge for reservoir characterization when based on well data alone.

Several laterally consistent horizons have been picked in order to understand the depositional architecture and lateral distribution of the related lithologies. Wells drilled at the reservoir location first tested the Eocene-aged Sürmeli member of the Kusuri Formation which is conformably underlain by the Eocene-aged Akçakoca member is mostly composed of hydrocarbon-bearing sandstone and shale sequences. Late Cretaceous, Akveren Formation which is composed of carbonates, is unconformably overlain by Kusuri formation, and finally Yemişliçay volcanics located at the base.

The conventional interpretation started by selection of series of horizons above, below and through the reservoir. Chapter 3 explains the details of the mapping procedure during and after interpretation. First, Sürmeli member has been picked and interpreted. Figure 17a and 17b show depth and time structure maps of Sürmeli member, respectively which indicate that major deformation is in east-west direction. Also Figure 17h shows the south-vergent thrust faults are significant and basically this deformation gives the final shape to the reservoir. Figure 17c is the azimuth map of the Sürmeli member, and it clearly shows the folded hanging wall of the thrust fault which is located to the northern part of the fault planes. Figure 17d is the coherency

map of the Sürmeli member, where black color represents the uncoherent events which generally imply fault or fault zones. This figure is polluted by acquisition footprint which is depicted by northwest-southeast oriented coherent linear events. Dip map of the Sürmeli member (figure 17e) indicates that at the survey area maximum dip is around 13^0, and the flat apex of the folded thrust faults can easily be recognized. Figure 17g shows the combined dip azimuth values which are from 1 to 64. Values 1 through 16 represent increasing dip values in the North quadrant (azimuths 315 to 45). Values 17 through 32 represent increasing dip in the East quadrant (azimuths 45 to 135). Values 33 through 48 represent increasing dip in the South quadrant (azimuths 135 to 225). Values 49 through 64 represent increasing dip in the West quadrant (azimuths 225 to 315). Each quadrant's the lowest value (1, 17, 33, and 49) corresponds to a dip of 0. Each quadrant's the highest value (16, 32, 48, and 64) corresponds to the maximum possible dip. In this case it is 13^0. Fault zones are delineated in detail with this dip-azimuth map. Finally, the instantaneous velocity map (Figure 17f) which is extracted along the Surmeli horizon from the instantaneous velocity model indicates the low velocity zones which are conformable with the folded structures. Change in thickness in Sürmeli member is limited except at fault zones (Figure 18). The stable thickness implies that deformation is post depositional which is also supported by the literature (Finetti et al., 1988; Yılmaz et al., 1997; Stephenson et al., 2004; Munteanu et al., 2011; Munteanu et al., 2013).

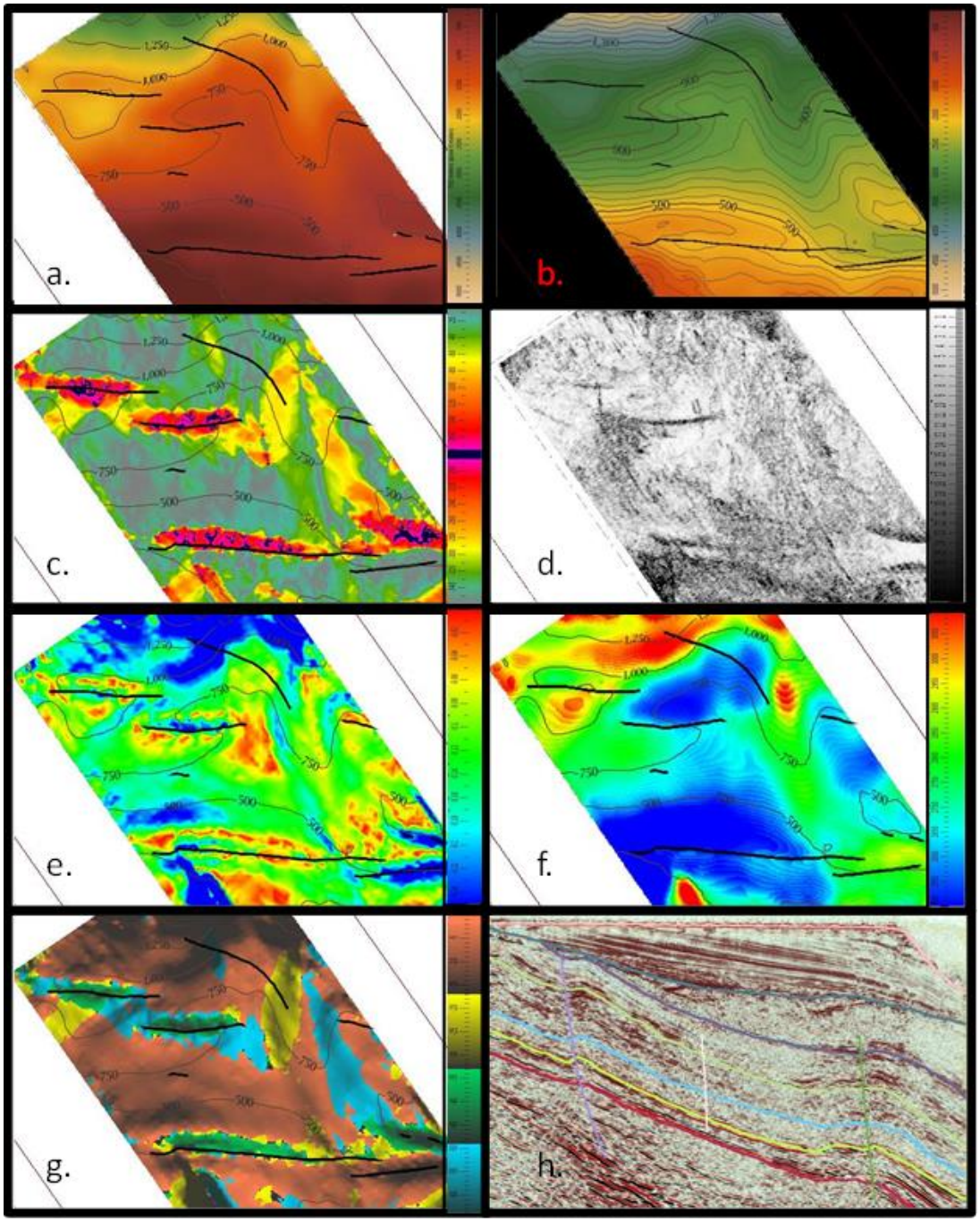


Figure 18 : Sürmeli Top a. depth structure map, b. time structure map, c. azimuth map, d. coherence map, e. dip map, f. instantaneous velocity map, g. dip azimuth map, h. interpreted seismic section,. Top reservoir laterally picked with purple line. Faults are drawn with thick black line at maps. Contours are in depth with 250 meters increment except time structure map which is in time with 400 millisecond increment and each of them drawn as thin black line. Thick red line indicates the location of the seismic section shown at 1h.

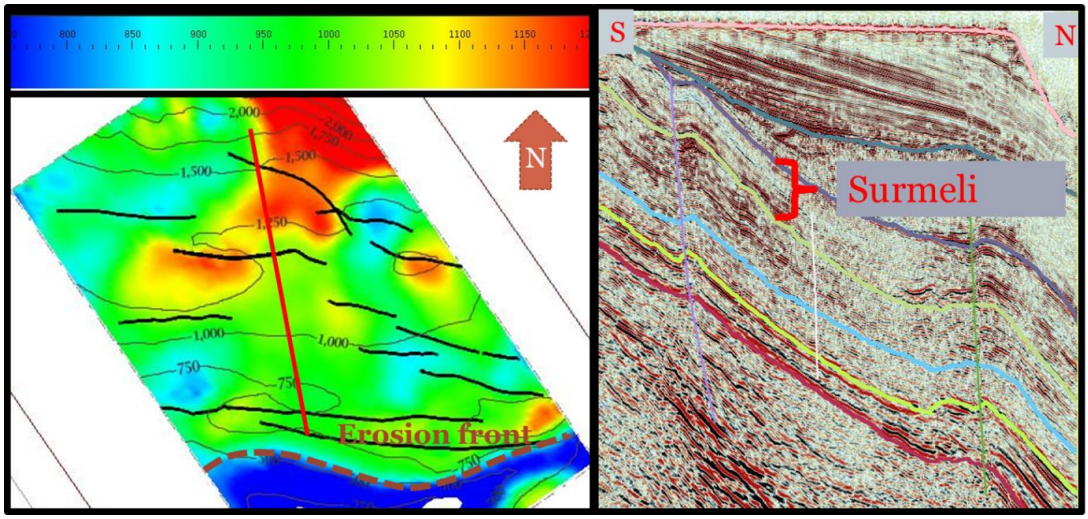


Figure 19 : Thickness map of the Sürmeli member (left) and interpreted seismic which indicates Sürmeli interval (right). Change in thickness is minimum, only thickening is seen at the fault zone due to shortening. Southern boundary of the survey area is interpreted as erosional front due to uplifting.

Next horizon interpretation has been done along the top of reservoir level within Akçakoca member. It is also called "AA Sand Top" which is one of the shallowest sandstone packages within the reservoir level. Figure 19a and 19b show depth and time structure maps of Akçakoca member, respectively which also indicate that major deformation is in east west direction. From the literature (Finetti et al., 1988; Yılmaz et al., 1997; Stephenson et al., 2004; Munteanu et al., 2011; Munteanu et al., 2013), the known presence of Late Eocene compressional deformation provided guidance during the fault interpretation. This compressional deformation is observed in Akçakoca 3D seismic survey starting from Mid-Eocene aged upper member of Kusuri formation to Late Cretaceous-aged Akveren Formation. The most of the Sürmeli member at the southern boundary of the survey area is deformed and eroded after uplifting stage of Late Eocene compressional event. Time to time, this erosional deformation can be so deep that it reaches down to top of Akçakoca member, specifically the AA Sand reservoir level. Also Figure 20h shows the south-vergent thrust faults. Figure 19c shows the azimuth map of the top Akçakoca member, and it clearly displays the folded hanging wall of the thrust fault which is located to the northern part of the fault planes at the top reservoir level. Figure 19d is the coherency

map of the top of Akçakoca member, and black color represents the incoherent events as mentioned earlier which generally imply fault or fault zones. Dip map of the top of Akçakoca member (figure 19e) indicates that the maximum dip is around 13^0 within survey area, and the flat apex of the folded hanging wall of thrust faults can easily be recognized which is considered as the reservoir location. Figure 19g shows the dip azimuth values. Fault zones are delineated in detail in this dip azimuth map. Specifically, antithetics of the thrust faults are easily recognized with their low dip values due to limited throws which are as small as zero. Finally, the instantaneous velocity map (Figure 19f) which is extracted along the top of AA Sand horizon from the instantaneous velocity model indicate the low velocity zones which might be clear acoustic response of gas bearing sandy reservoir. Low velocity zones are also conformable with the folded structures which coincide to reservoir locations.

The bottom of the reservoir levels has been interpreted and called as bottom of F Sand deepest reservoir level at the survey area. Its time and depth structure map including various geometric maps shown at figure 20. Folding at the hanging wall of the thrust faults is in maximum when the fault plane is close to the shoreline. Maximum folding is related to the shortening, and it shows the maximum increase of thickness at the southern boundary. Thickness between the fault planes is almost constant in the east-west direction which may imply the sediment fairway is in south-north direction. Overview of the thickness map shows general thinning towards the basin due to deposition (Figure 21).

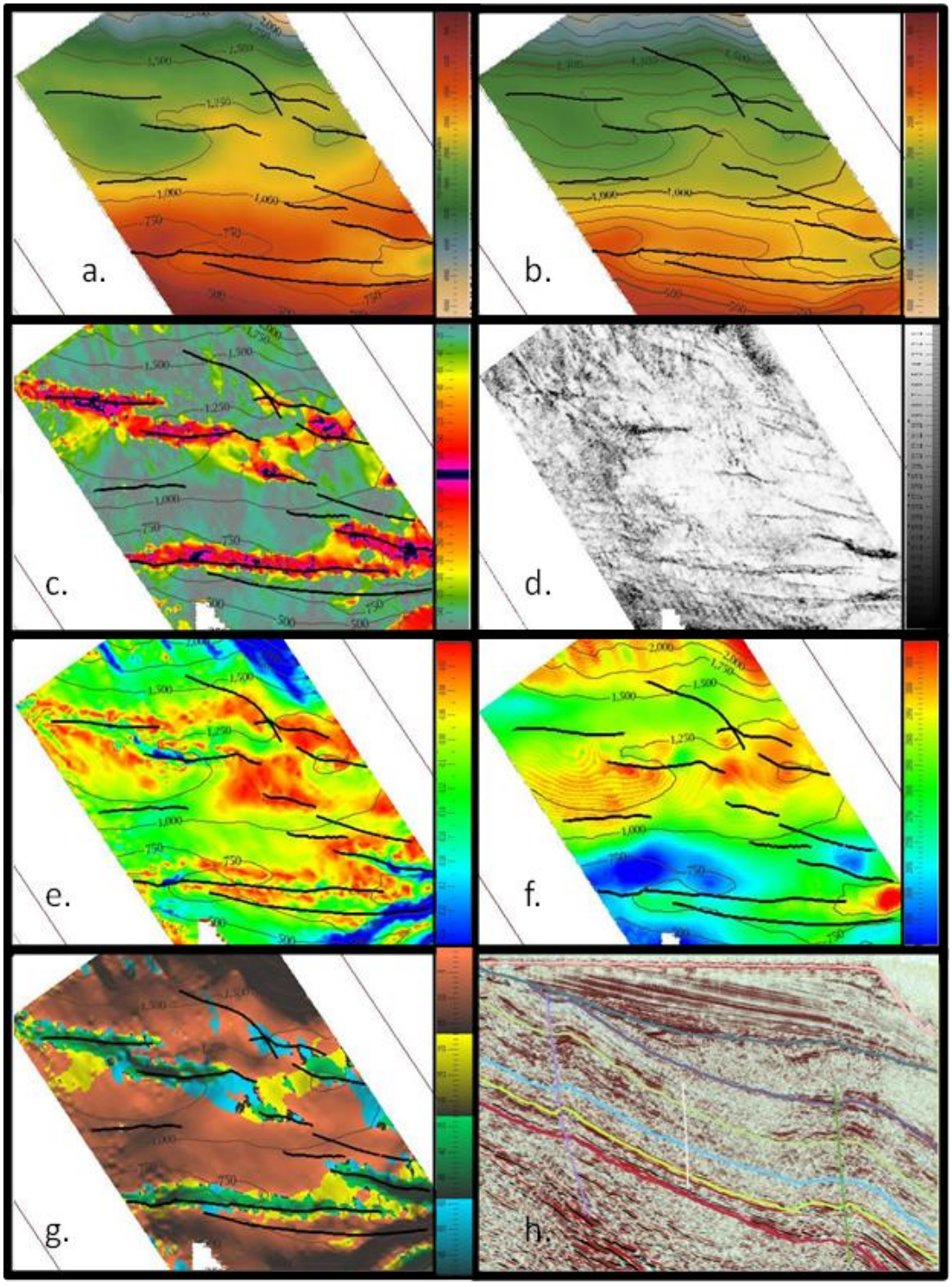


Figure 20 : AA Sand Top a. depth structure map, b. time structure map, c. azimuth map, d. coherence map, e. dip map, f. instantaneous velocity map, g. dip azimuth map, h. interpreted seismic section,. Top reservoir laterally picked with green line. Faults are drawn with thick black line at maps. Contours are in depth with 250 meters increment except time structure map which is in time with 100 millisecond increment and each of them drawn as thin black line. Thick red line indicates the location of the seismic section shown at 3h.

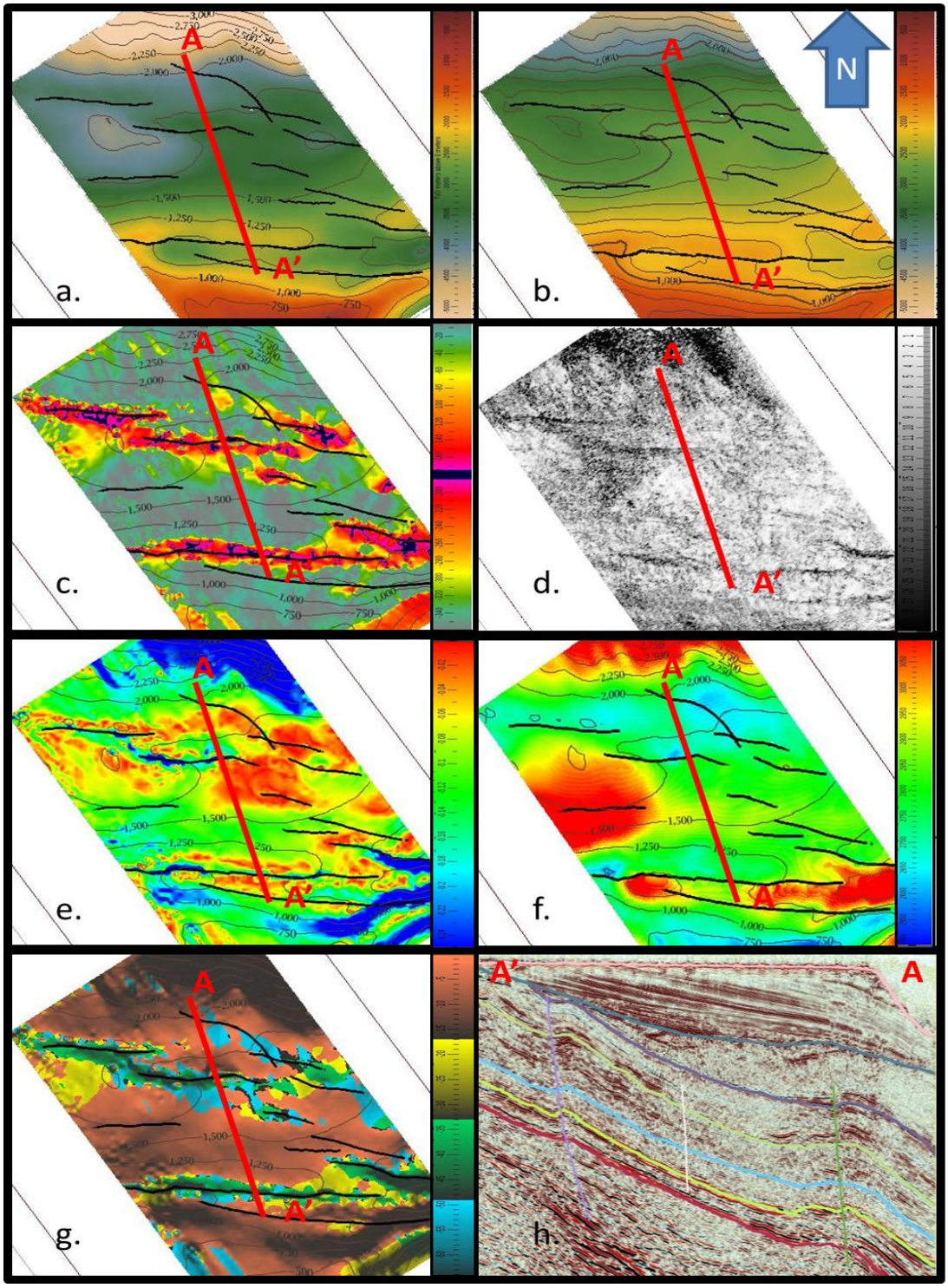


Figure 21 : F Sand Bottom a. depth structure map, b. time structure map, c. azimuth map, d. coherence map, e. dip map, f. instantaneous velocity map, g. dip azimuth map, h. interpreted seismic section,. Top reservoir laterally picked with light blue line. Faults are drawn with thick black line at maps. Contours are in depth with 250 meters increment except time structure map which is in time with 100 millisecond increment and each of them drawn as thin black line. Thick red line indicates the location of the seismic section shown at 4h.

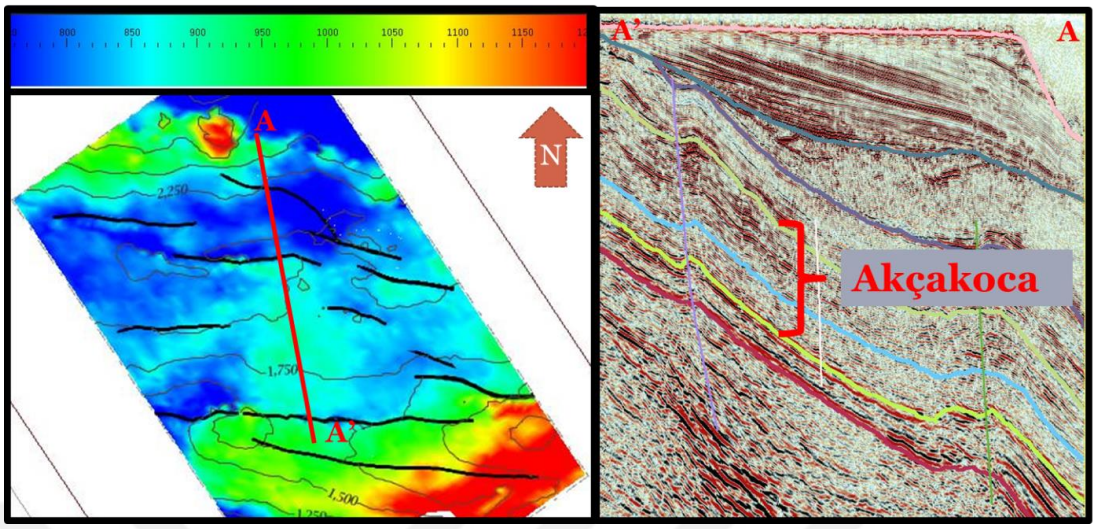


Figure 22 : Thickness map of the Akcakoca member on the left and interpreted seismic which indicates Akcakoca interval on the right. Thick red line on the map indicates the location of the seismic section shown on the left. Folding at the hanging wall of the thrust faults is in maximum when the fault plane is close to the shoreline. Maximum folding is related to the shorting, and it shows the maximum increment of thickness at the southern boundary. Between the fault planes thickness is almost constant through the east west direction which may imply the sediment fairway is in south north direction. Overview of the thickness map shows general thinning towards the basin due to deposition.

Late Cretaceous-Paleocene Akveren Formation has been picked and interpreted as shown in Figure 22. It is composed of carbonate rocks which were deposited on the paleo-high of Late Cretaceous volcanic arc in Western Black Sea Basin. Akcakoca 3D seismic clearly shows that interpreted Akveren Formation was affected by the Late Eocene deformation (Figure 22a, 22b, 22c, 22d, 22e, 22f and 22g). Although thickness map of the Akveren Formation indicates that major thickness changes occur at the fault zones (Figure 23), the average thickness is generally around 300-400 m.

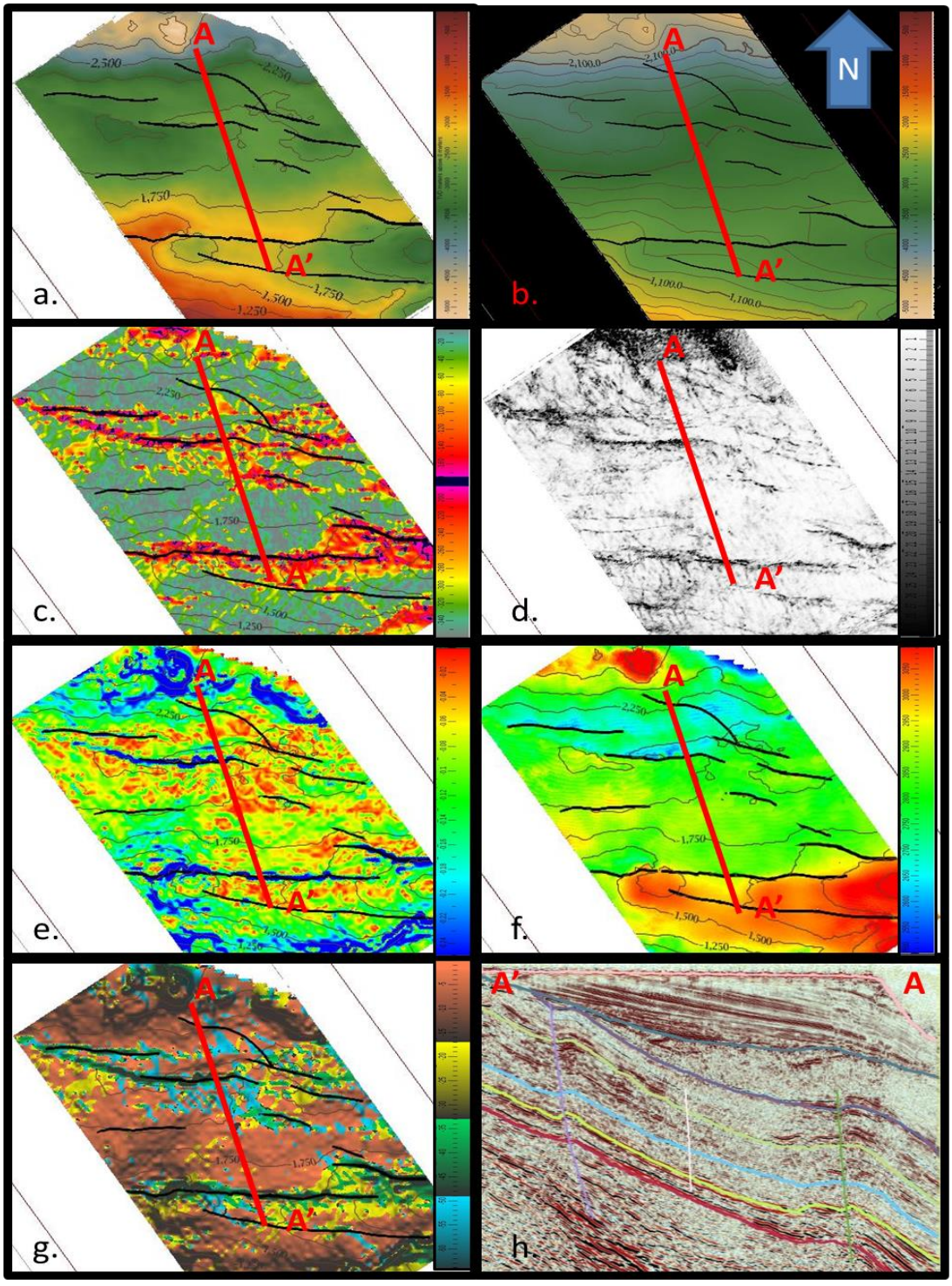


Figure 23 : Top of Akveren formation a. depth structure map, b. time structure map, c. azimuth map, d. coherence map, e. dip map, f. instantaneous velocity map, g. dip azimuth map, h. interpreted seismic section. Top Akveren laterally picked with yellow line. Faults are drawn with thick black line at maps. Contours are in depth with 250 meters increment except time structure map which is in time with 100 millisecond increment and each of them drawn as thin black line. Thick red line indicates the location of the seismic section shown at 6h.

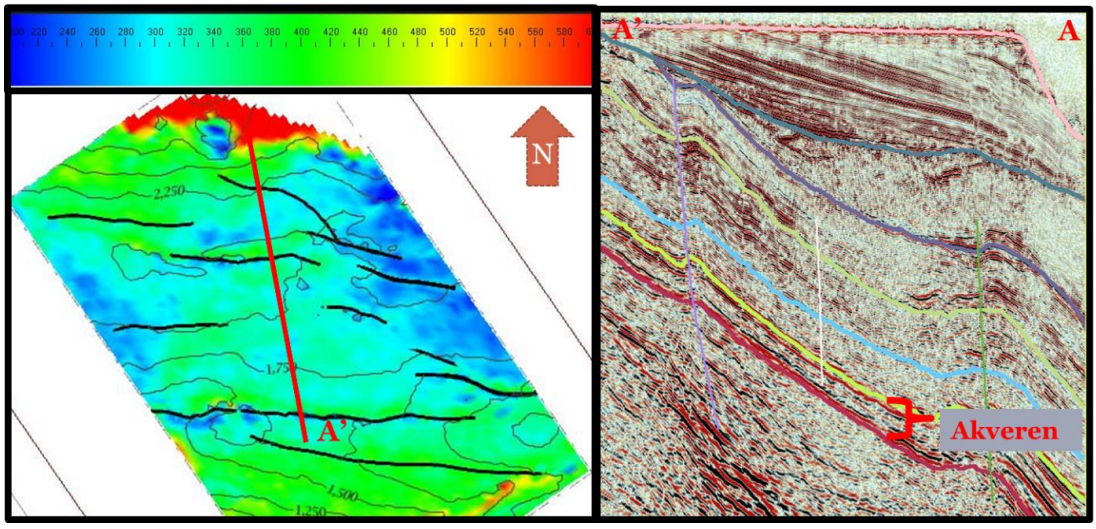


Figure 24 : Thickness map of the Akveren formation on the left and interpreted seismic which indicates Akveren interval on the right. Thick red line on the map indicates the location of the seismic section shown on the left. Thickness change at the fault zones are in maximum. Scale is relatively small and thickness is changing from 300 meters to 400 meters.

The lateral changes of amplitude are the major indicator of distinguishing one facies from another. At the study area, the top of Akçakoca Formation has continuous, high to moderate amplitudes on seismic sections which may be indicative of shale-prone flood plain deposits and any sinusoidal geometry with high amplitude is interpreted as submarine turbidite channel with sandy facies (Figure 24). Differences in sand-shale ratio and geometries can be easily analyzed in the amplitude map and interpreted as elements of depositional environment. Generally, fault planes are considered as incoherent surfaces, and their geometries in amplitude maps are characterized by lineaments with dim amplitudes along the fault plane direction.

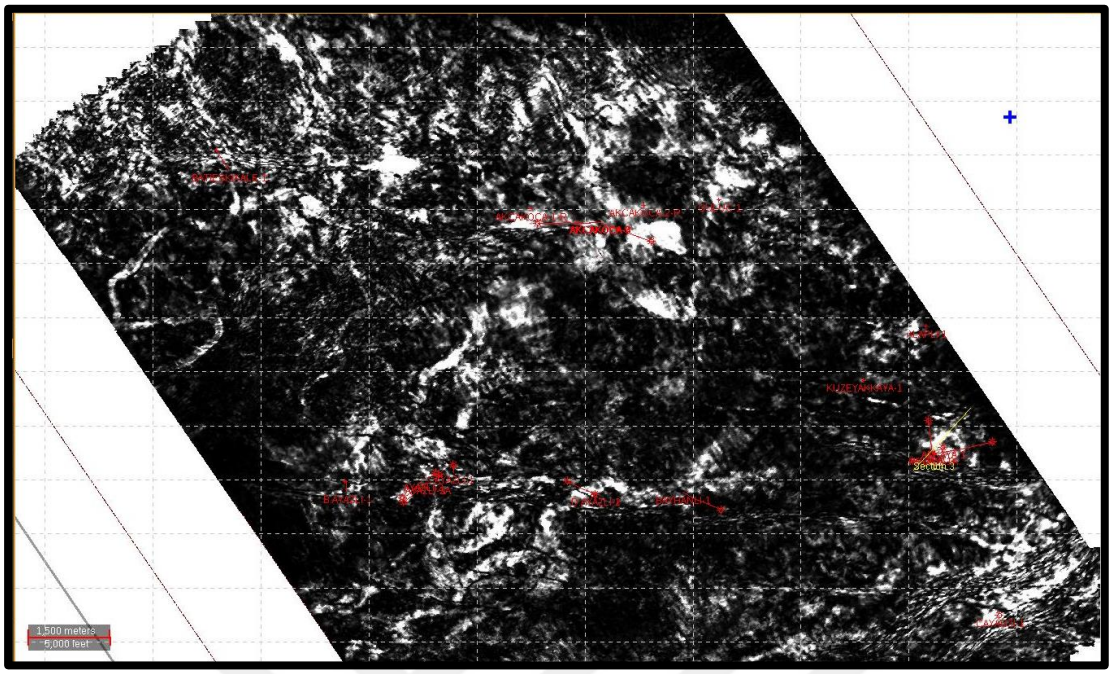


Figure 25 : RMS amplitude map of the D Sand. High amplitudes are in white and dim amplitudes are in black. Channelized geometries shown in white are the indication of relatively higher sand-shale ratio. Continuous black colored area is considered to be shale prone flood plain where the turbidite channels transport their sediment loads into the basin.

Spectrally decomposed amplitude maps at different frequency bands (Figure 25) indicate the facies distribution along the geometries that have been identified on the seismic might vary and can be detected in great detail. Thus, it can be help to construct well-defined facies maps for the reservoir levels. In figure 25 shows several frequency panels ranging from 5 Hz to 45 Hz. At figure 26, 25x30 Hz panel shows a high sinuosity, low energy, subaqueous, turbidity channel existing within the reservoir level. Furthermore, at the same panel, point bars are specifically represented by high amplitudes which do not seem coincidence because high amplitudes are, in general, interpreted to indicate high sand content. Point bars are the best places where possibility of encountering sands is the highest. Interpreting this information with other frequency panels would be much valuable. For instance, that the lower frequency bands do not define the channel very well might be interpreted as much of the channel geometries contain shale or, in this case, seismic does not have valuable signal lower

than 5 Hz. With this acquisition-related information, first panel barely contains any signal that can be interpreted. Since high magnitude of the amplitude gives sand related response, and higher frequency panel shows the lower part of the channel geometry in high amplitude, this map implies the lower part is mostly sand. Specifically, this channel is located at as deep as 1000 m with 3000 m/s velocity and its reflection is around 6.25 m thick for 40 Hz and 12.5 m thick for 20 Hz. This means at the point where the interpretation stands, there is at least 12.5 m thick sand for the lower part of the channel. However, upper part of the channel has another story. In the panel showing frequencies higher than 25 Hz, upper part of the channel does not show a clear geometry which implies that this part of the channel is mainly shale dominated. But this information can be constrained vertically because the channel is detected at lower frequency panels. For the upper part of the channel, our reflection is around 10 meters thick at 25 Hz and any thickness thinner than 10 meter is detected by higher frequency panels implying the point where the interpretation stands there is no distinctive sand response. In another words, upper part of the channel is shalier than the lower part even though whole submarine channel is mainly sand dominated.

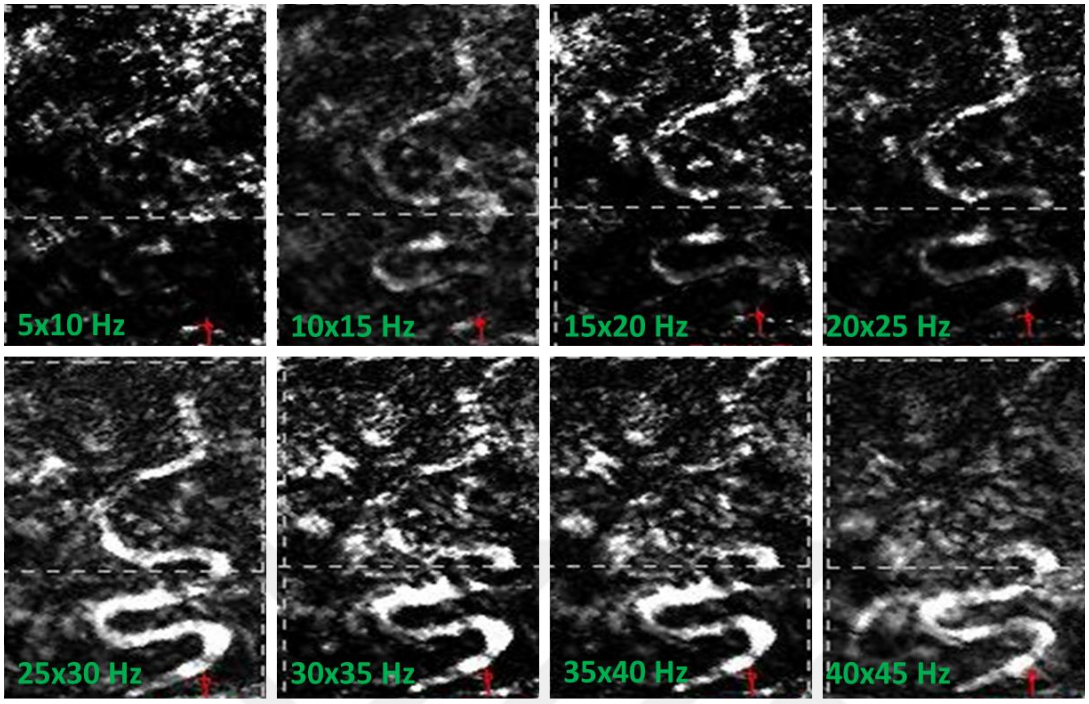


Figure 26 : Amplitude map of a channelize system at several frequency bands ranging from 5Hz to 45Hz.

In order to combine all these facies and depositional environment related information, spectral decomposition has been run on the 3D seismic volume. Several spectrally decomposed maps have been generated and analyzed from bottom to the top of Akçakoca reservoirs. The older sinusoidal, subaqueous, channel system (figure 26e and 26f) is interpreted as having low to moderate energy and deposited proximal to the southern shoreline. However, at further stages the channelized geometries (figure 26c and 26d) laterally migrate to the north due to uplifting of the southern margin of the basin. Deformation rate is interpreted to have been controlling the sediment influx at this stage. At the bottom part of the Akçakoca reservoirs, sinusoidal channel geometries do not change their orientation or shape while crossing the east-west oriented faults. This may imply that faults are postdated by Eocene aged turbidite channels. Moreover, at the last stage (figure 26a and 26b), there is not distinctive and steady channel geometry at the southern margin. During this period, sediment input is clearly in east to west direction which shows that faults are recently generated and

started to lead sediments through the basin. This sudden change in sediment direction is due to a higher rate of uplift of the southern margin. Surprisingly, it is even possible to see an event which might be interpreted as an abandoned channel, which is significant with its green color (figure 26e). This oxbow-looking event can be another imprint of turning low energy channel system into a high energy straight channel system due to deformation or uplift of the southern margin.

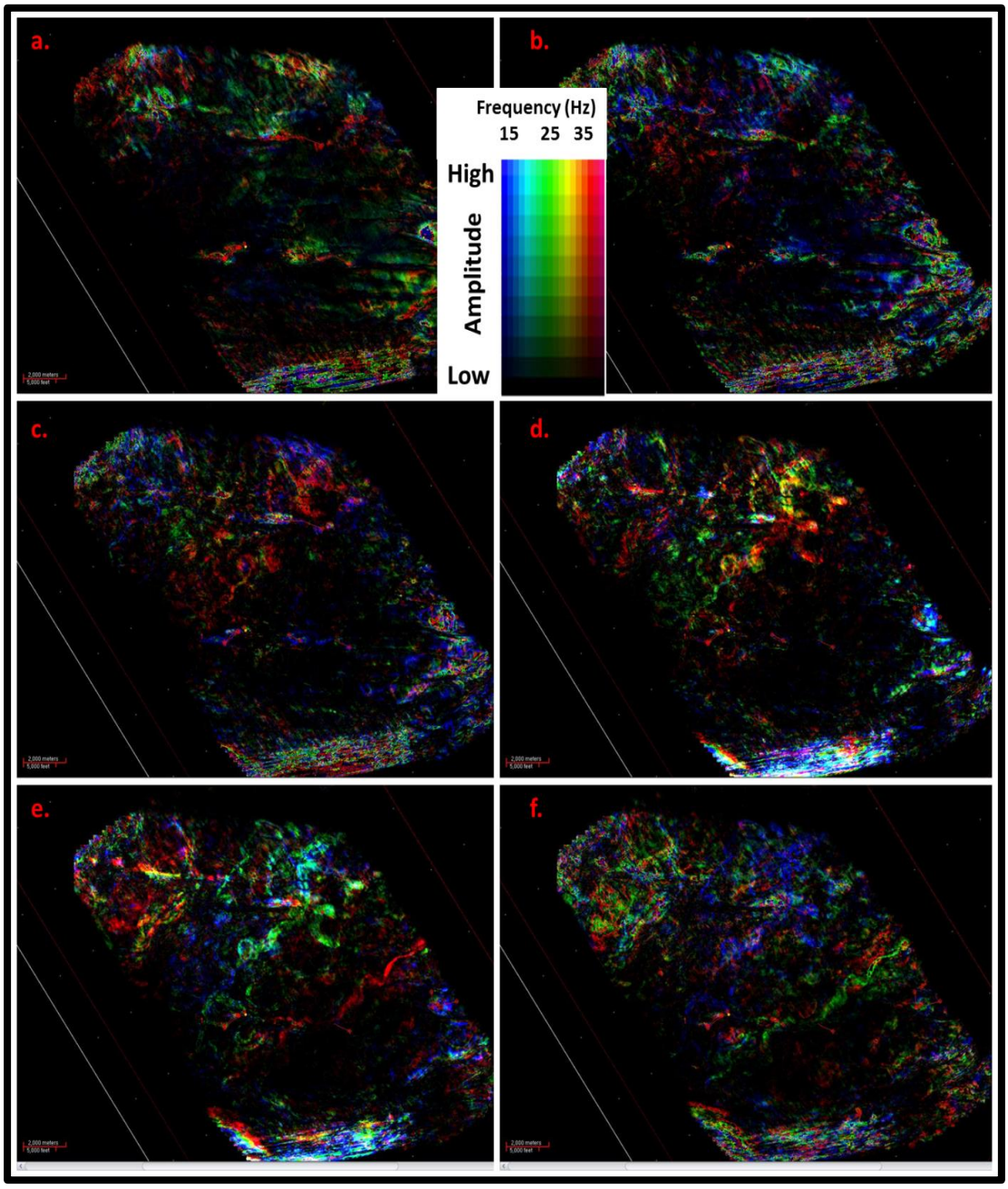


Figure 27 : Spectrally decomposed (15x25x35Hz, RGB color coded) maps of a. A Sand, b. B Sand, b. B Sand, c. C Sand, d. D Sand, e. E Sand, and f. F Sand.

4.1.2 Well tie and correlation

Classified well locations have been plotted on coherency map showing the relationship between fault trends and well locations (Figure 27). Representation of well tie and generated synthetic at a well in Field-1 zone are drawn in figure 28. Related time-depth function and the functions for each well have been generated and used in correlating lithologies at the survey area.

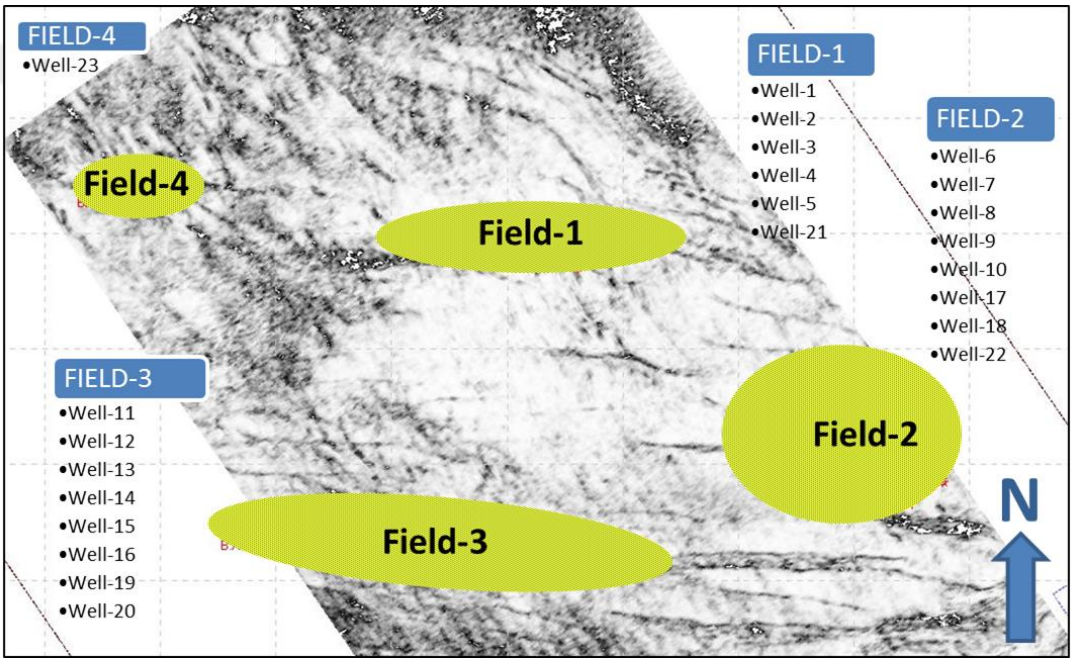


Figure 28 : Coherence map showing well locations which are classified with respect to their prospect positions. Field-1, 2 and 3 are the group of gas producing well locations. Field-4 is a single well location which is used for blind well test and interpreted separately.

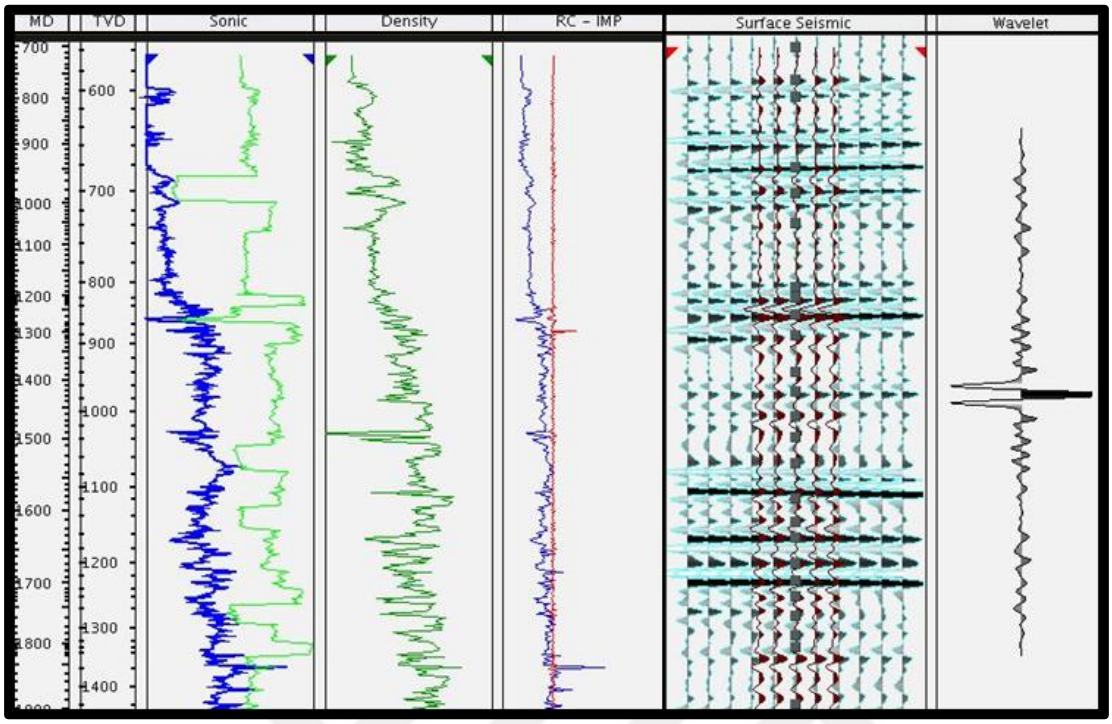


Figure 29 : Well tie representation from Field-1 production area. Sonic, Density, Reflection Coefficients (RC), Impedance (IMP), Observed seismic inline section with 5 synthetic traces in red color and the extracted wavelet used at convolution. More than 60 % correlation exists between observed data and generated synthetic. It is in acceptable range.

Figure 29 shows the well correlation at field-3 location. After hanging the formation at the key bed (AA Sand or tuff level), sand correlation has been done and named as AA Sand, A Sand, B Sand, C Sand, D Sand, DE Sand, E Sand, and F Sand (Figure 30). Only first three reservoirs are displayed at figure 29. Identifying sandy reservoir can be done with several ways. For instance, gamma ray, density and resistivity log responses can be used for identifying reservoir but downside of the well-log only correlation is that there might be similar log responses which are represented by different facies. Therefore, it has to be updated with the cuttings as well.

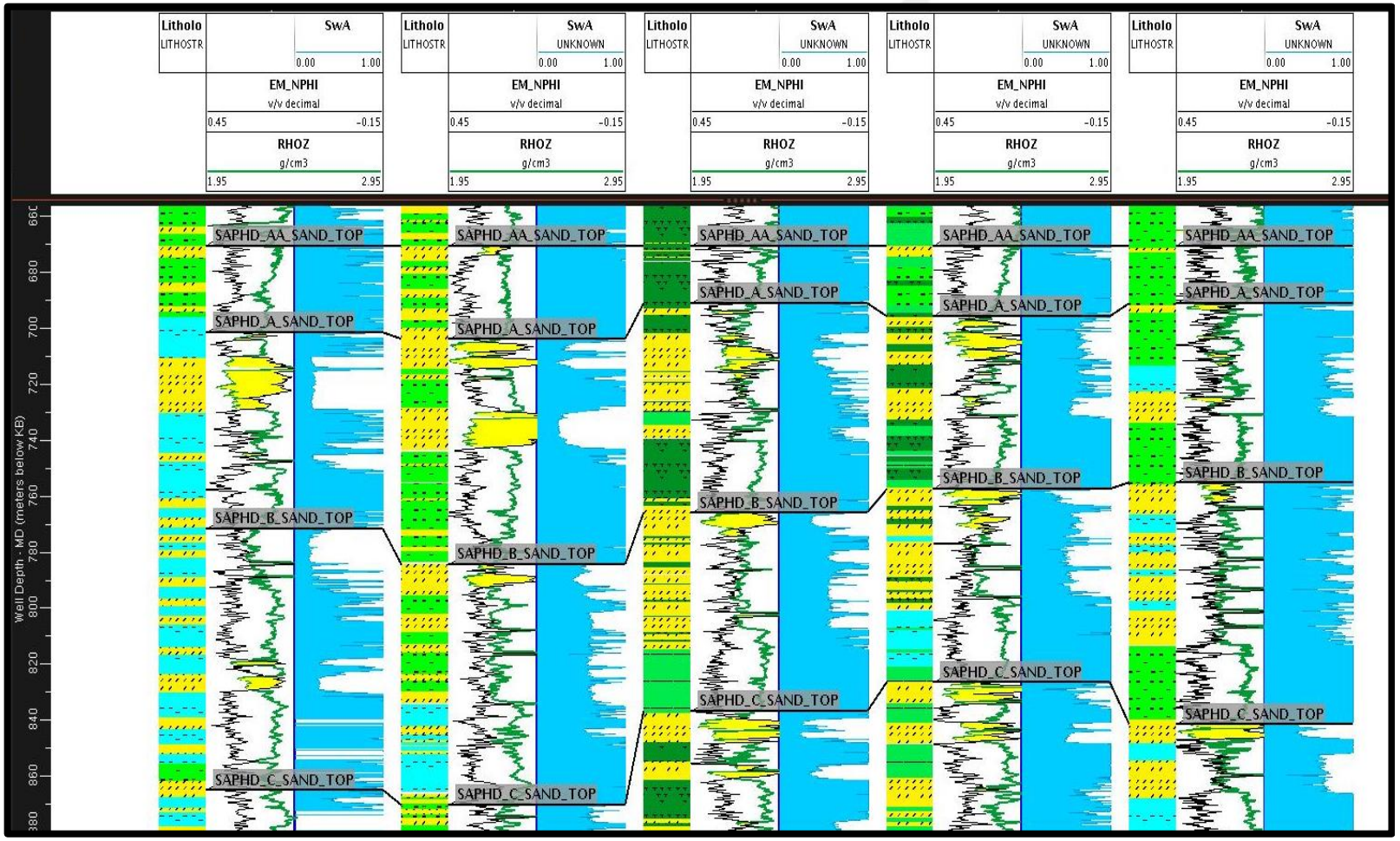


Figure 30 : Well correlation 5 wells from the Field-3 production field with facies, density (RHOZ), porosity (EM_NPHI) and water saturation (SwA) logs. AA, A, B, and C sand top can be seen. Low density high porosity crosses from the logs are colored to yellow which indicates gas bearing sands. Water saturation (SwA) is colored to blue

In order to have more well-based information, facies log has been generated based on composite logs which are derived from electrical logs and cuttings as well as existing well information. Generated facies log consists of the lithologies which are the most frequently tested at the wells, and these are listed as tuff, sandstone, marl, silt, clay, and shale. Density-porosity curves indicate gas charged reservoir levels where the log values are crossing and these intervals are colored with yellow for a simplistic representation of HC (Figure 30). Each gas bearing sand package has its own gas-water contact (GWC), and this feature helps to reconnaissance individual sand reservoirs as they are defined at figure 30 for A-Sand. Water saturated sands are diverging from gas saturated sand by their density and porosity log responses as well as gamma ray. Facies logs displayed at figure 29 indicates that there are at least two different sand facies. One of which is gas saturated and other one is water saturated sands. Detail investigation has been done while log based rock physics analysis applied to data.

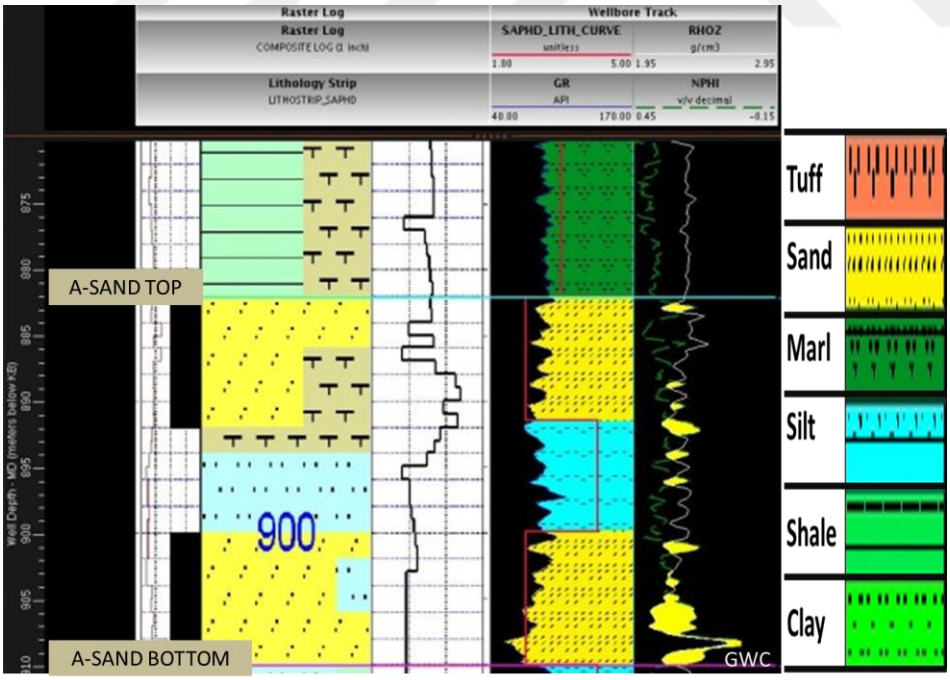


Figure 32: Well correlation at Field-2 location. A-Sand lithotype definition. Generated facies curve is plotted next to composite log and onto gamma log. Density, porosity curves are also plotted and any crossing area colored with yellow as an indication of gas charge. Sand package is underlain by a gas water contact (GWC).

4.1.3 Velocity Analysis and Modeling

Interpreted time surfaces and their depth converted structure maps are shown in figure 17a, 17b, 19a, 19b, 20a, 20b, 22a and 22b. Chapter 3 explains the velocity model construction workflow. A tomographic velocity model (Figure 31) has been constructed and used for time-depth conversion. Transferring log base velocity information into velocity model is only possible with proper well-tie (Figure 28). Existing check shot or VSP information is used for calibrating sonic logs and individual synthetics are created for each well. After all, each well has its own unique time depth functions. Each time-depth function is converted to the several velocity functions such as interval, instantaneous, average or RMS velocity in order to check any abnormal velocity values which do not fit to any lithologically meaningful explanation. Figure 28 shows an example of the well tie procedure which has been followed during the study.

A certain degree of accuracy in the velocity field over the study area is required for proper time-depth conversion. It has to be pointed out, this is an iterative procedure, and there is no unique answer for the velocity. In order to start this iterative flow, one might start with a single velocity function which is defined by regional velocity information. Another good starting point might be the processing velocities (Figure 31d) over the survey area since these are picked densely and interpolated through each trace location. The procedure of matching formation tops (values in meters) with reflection surfaces (values in time), and propagating the related velocity through the surface is another source of velocity (Figure 31a) which might be used. This gives a constant velocity through the surface. Finally, time-depth function (figure 31c, 31d) which is used for tying the seismic time section to depth values of a well is an input to velocity model. As mentioned above, several types of velocity, velocity function or field can be derived from different ways but the important point is that these velocities should be combined into a velocity model. There are several ways; one might use to combine these velocity values, one of which used in this study is inverse weighted distance interpolation, and other one is least squares method which is based on minimizing time differences up to a certain thresholds, and it is simply called *tomographic solution* (figure 31f).

As soon as the proper velocity model exists the time domain seismic interpretation can be converted to depth, and interpreted as it is. Moreover, depth-

converted reflection surfaces are always supported by the well data since the velocity model which is subjected to depth conversion is derived by using the well itself.

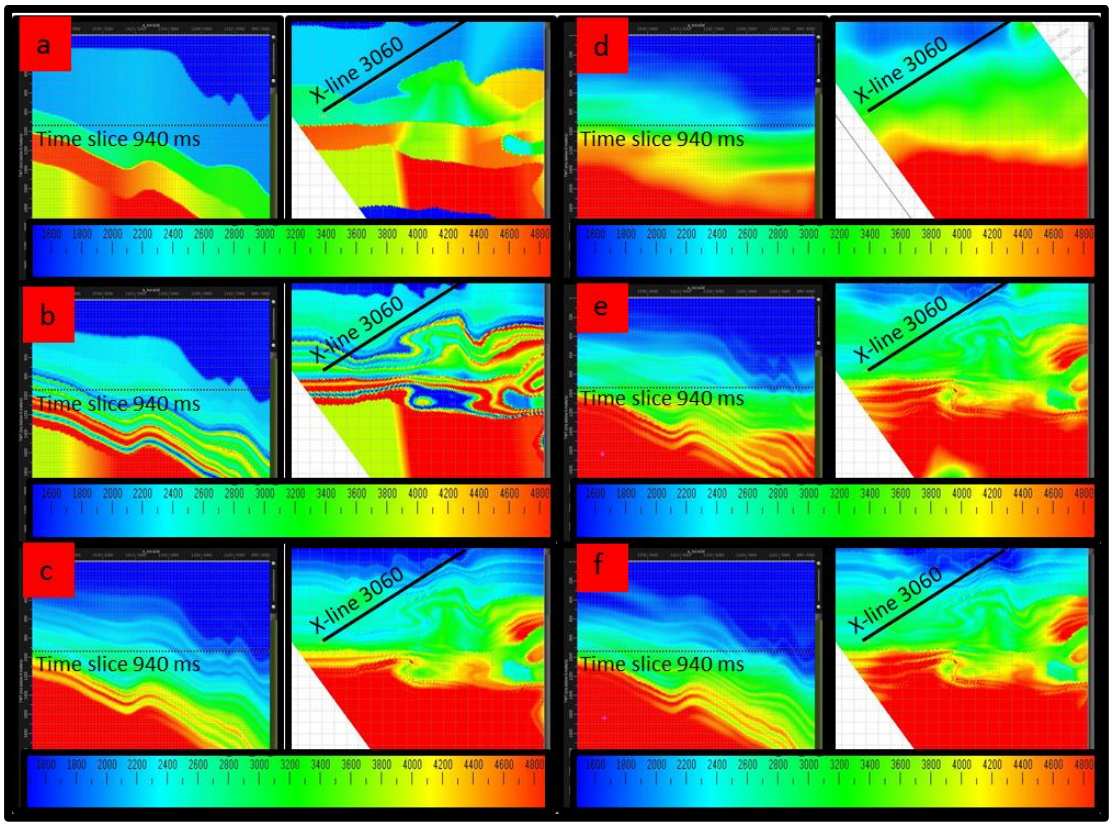


Figure 33: Velocity model building schemes. a. A simple constant velocity section x-line 3060 which is collected by matching formation top and interpreted surface and its time slice at 940 ms b. Velocity section x-line 3060 which is produced by a single time depth function distributed through surface and its time slice at 940 ms. c. Velocity section x-line 3060 which produced by multiple time depth functions interpolated through the surfaces and its time slice at 940 ms. d. Stacking velocities shown as section in x-line 3060 and its time slice at 940 ms. e. Inversely weighted interpolation of all the available velocity functions shown as section in x-line 3060 and its time slice at 940 ms. f. Least square tomographic solution for all the available velocity inputs and its time slice at 940 ms.

4.1.4 Petrophysical Log Calculation and Evaluation

Available logs for this project are listed in figure 4. Some of the logs have been edited and some of them have been estimated from the existing logs. There are three types of log calculations one of which is volume based calculations such as bulk volume of water, hydrocarbon pore volume or volume shale. Another one is rock property calculation such as effective porosity and permeability. These two types of calculations, their formula and constants are listed in Table 1 in Chapter 3. Average porosity has been calculated by averaging sonic and neutron porosities. Effective porosity has been calculated by using volume of shale estimation. Permeability has been calculated by the empirical formulas of Tixier, Timur and Coates (Torskaya et. al., 2007) separately. These three permeability estimations are compared with the permeability values derived from laboratory measurements of cores and outcrop samples (Courtesy of TPAO) (Figure 32 and 33). Porosity vs. permeability cross-plot gives an exponential relation. In this study, this relation has been formulized and used to generate an extra permeability log at well location. All the permeability porosity estimations give similar trend up to %12 porosity. Increasing porosity values are aggressively diverging Tixier and Timur's empirical formulas from Coates and the measurements of core and outcrop samples.

Effective porosity has been calculated by multiplying average porosity with volume of sand. One way of calculating volume of sand is subtracting volume of shale from 1. Volume of shale has been calculated by gamma ray log. The last calculation is the elastic property calculation such as acoustic impedance, Poisson's ratio, Vp/Vs ratio, lambda-rho and mu-rho. These elastic logs are the main inputs for the rock physics analysis.

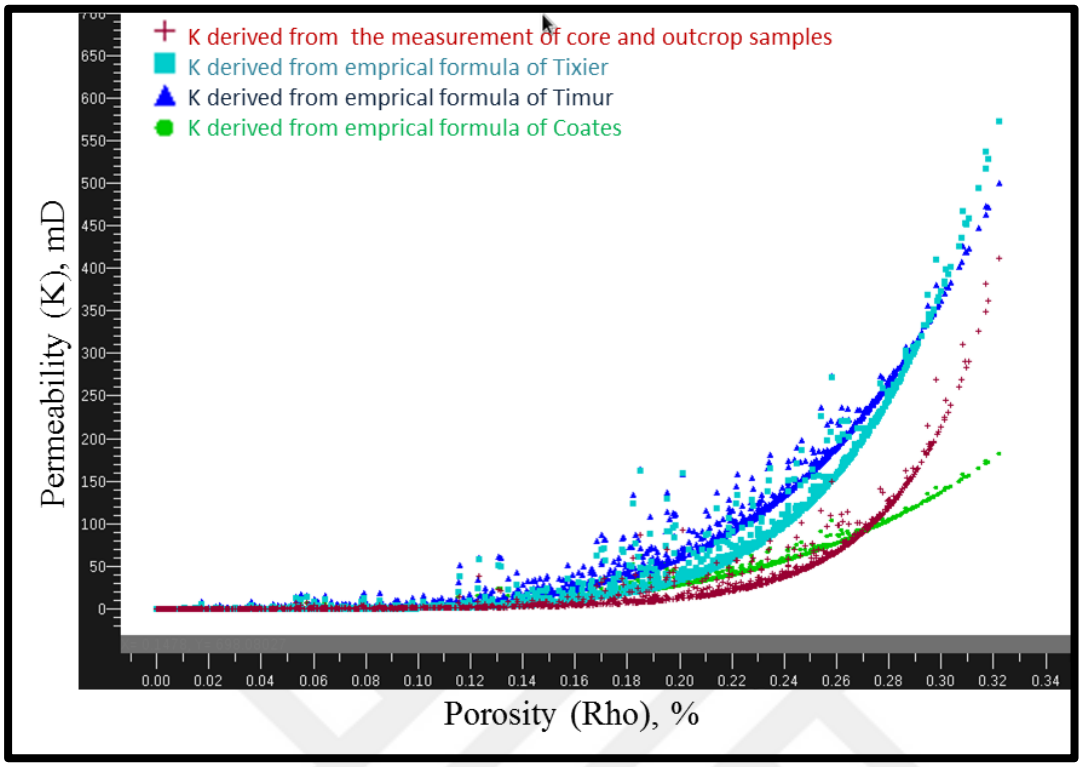


Figure 34: Permeability vs. porosity cross-plot shows comparison of the empirical permeability estimations with laboratory measurements of permeability (derived from the formula shown in figure 34) from core and outcrop samples (Data set is courtesy of TPAO).

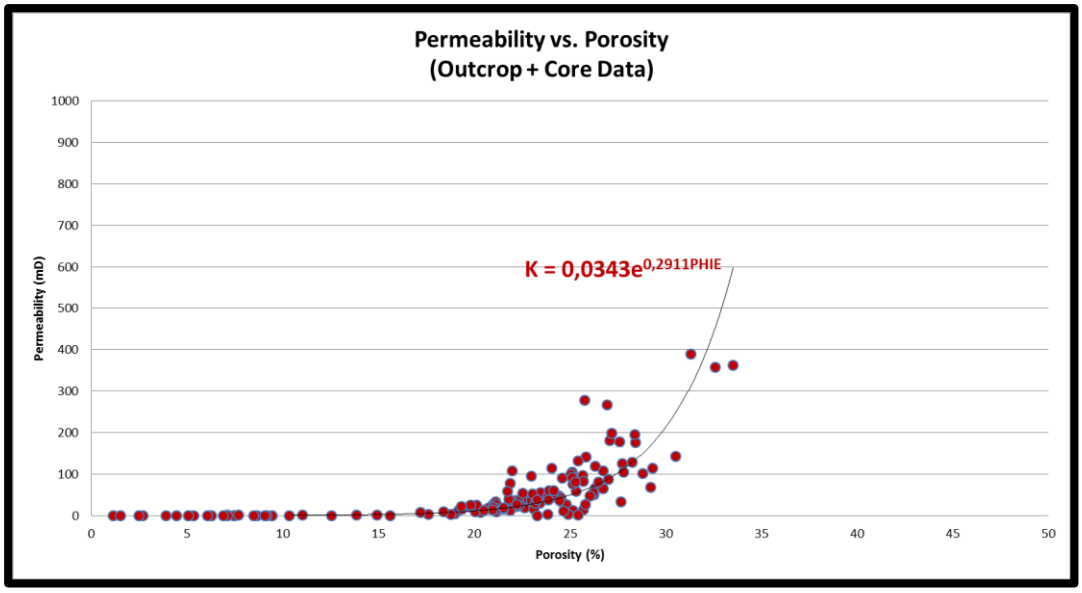
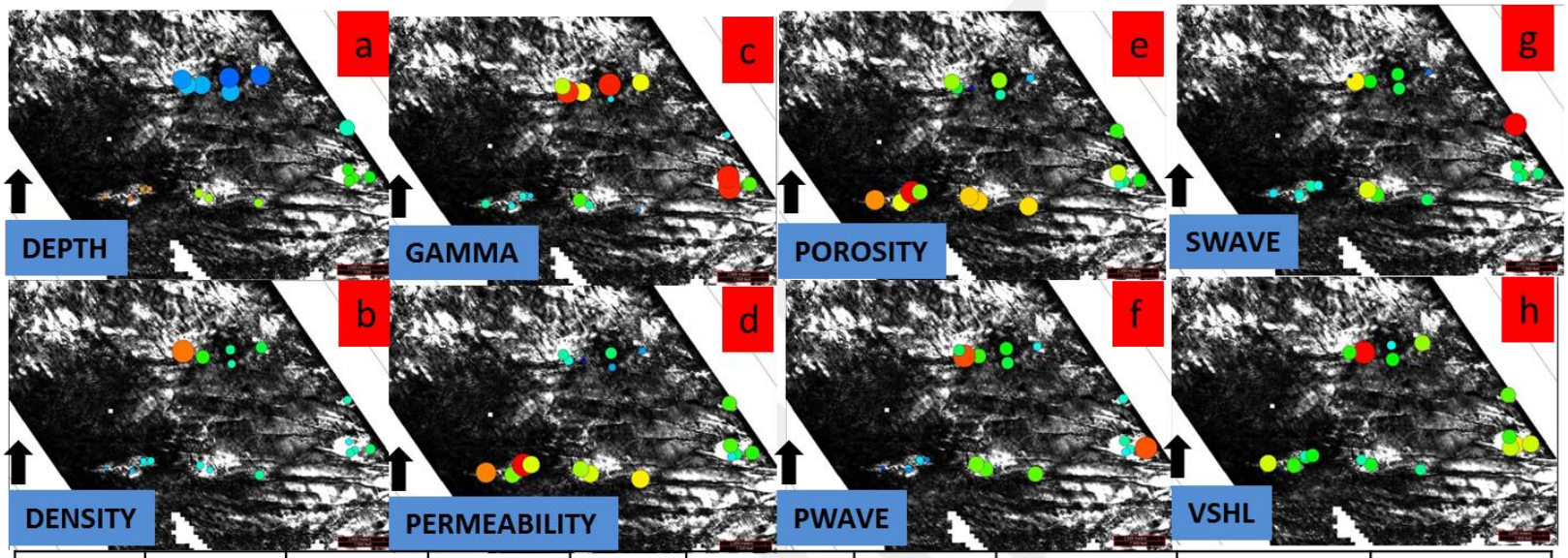


Figure 35: Permeability vs. porosity cross-plot shows exponential relationship which can be formulized as shown. (Data set is courtesy of TPAO).



A SAND	Color Bar	Averaged Depth	Averaged Density	Averaged Gamma	Averaged Permeability	Averaged Porosity	Averaged Pwave	Averaged Swave	Averaged Vshl
Unit	RGB	*m*	*gr/cc*	*API*	*mD*	*%*	*ms*	*ms*	*%*
Max		-500	2.6	91	100	24	3400	1900	80
Min		-1300	2.1	60	8	10	2400	1000	24

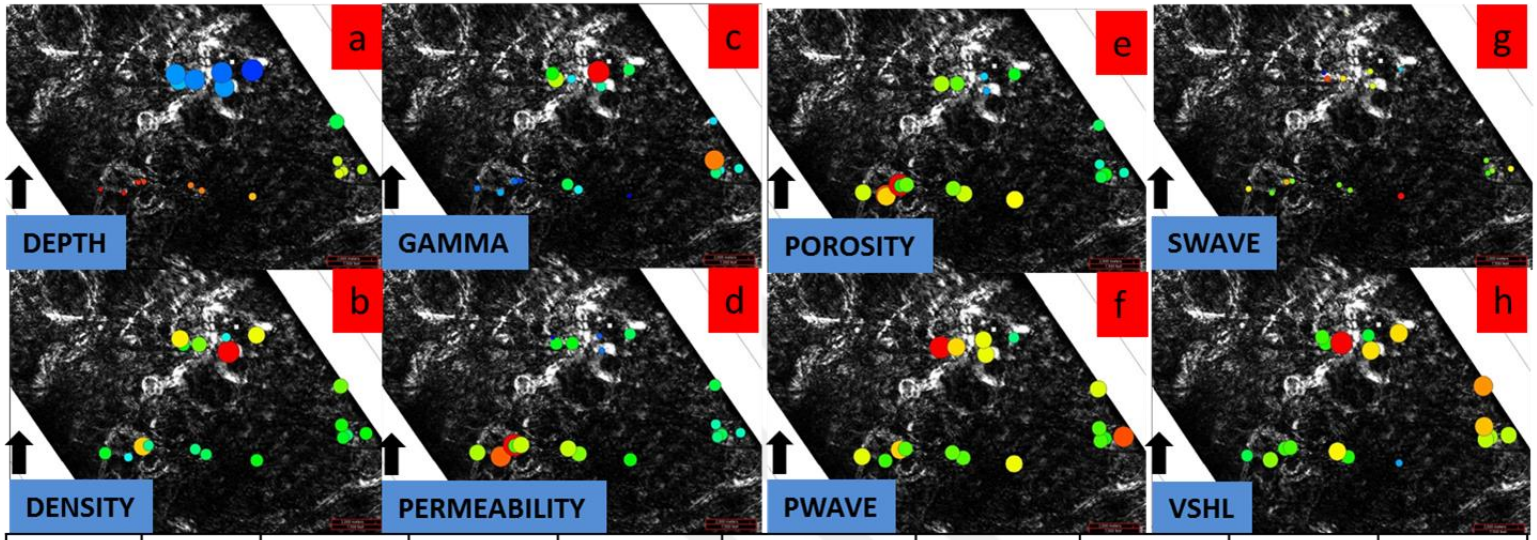
Figure 36: Amplitude map (high amplitudes are colored white) of A-Sand with wells represented by circles which colored and sized in order to emphasize a) depth of reservoir, b) average density, c) average gamma, d) average permeability, e) average porosity, f) average P wave velocity, g) average S wave velocity and h) average volume of shale. Min and max average log values are listed.

Akcakoca reservoirs and their burial depths are different from each other. Understanding general rock property trends and heterogeneity within and between the reservoirs is important. Moreover, log responses can change depending on the depositional environment and direction of sediment supply as well as syn-depositional and post-depositional deformation. Since depositional environment of the reservoir does not change within the survey area, the main focus for the log response analysis is on the direction of sediment supply and structural deformation. In order to correlate deformation, source of sediments and log responses of the reservoirs, observed and calculated log responses are averaged and displayed on the amplitude maps (figure 34 and 35). It has already been introduced at figure 27 that there are three major fields which can be seen at depth values of A Sand reservoir (figure 34a). Field-1, Field-2 and Field-3 are defined as from deepest to shallowest respectively. Furthermore, density values seem to be increase depending on to the burial depth of reservoir (figure 34b). Similarly, there is a good correlation between average gamma, density, permeability and porosity values as well (figure 34b, 34c, 34d and 34e). Averaged P and S wave values are in similar trend for the Field-1 and Field-3 but Field-2 is little different in terms of velocity (figure 34f and 34g). This observation reveals that impedance change between Field-1 and Field-3 is mostly controlled by the density another word lithology. However, any impedance related comparison between Field-1 and Field-2 or Field-3 needs detail investigation which counts fluid response as well for A Sand reservoir. Finally, volume of shale shows that Field-1 has more shale content than the Field-2 and Field-3 (figure 34h).

DE Sand is located within the deeper section of the Akçakoca reservoirs. Seismic interpretation and amplitude map of reservoirs reveal that direction of sediment supply differ within the Akçakoca reservoirs. Sediment dispersal system at A Sand reservoir is mainly controlled by faulting and possible southern margin uplift. Source of sediments is directed from East to West. Channels get straight rather than sinusoidal as a result of sudden uplift at the basement. However, amplitude map of DE Sand shows a group of sinusoidal channel propagated from SW to NE which imply that sediment dispersal system is totally different than top of the Akçakoca reservoirs. Figure 35a shows that Field-3 is little bit distal than the Field-3 at the same turbidite channel system. Averaged density values indicate deeper section of the channel system

has larger density values. Averaged gamma and volume of shale responses (figure 35c and 35h) show that channel system which field-1 and field-3 located gets shalier as it propagates into the basin.

So far, the reservoir levels have been interpreted and geologically identified by their geometric and physical properties. Well tie and correlation procedures have been applied for each well. By combining all the available inputs from different sources, proper velocity model has been created in order to use it for time to depth conversion. Log preparation, estimation and calculation were the part of the petrophysical studies at the survey area. Especially, permeability estimation took place, and the best possible empirical relation is determined as Coates empirical formula out of the four different sources of porosity and permeability relations. At this point, all the solid data needed in constructing the skeleton of the model is ready.



DE SAND	Color Bar	Averaged Depth	Averaged Density	Averaged Gamma	Averaged Permeability	Averaged Porosity	Averaged Pwave	Averaged Swave	Averaged Vshl
Unit	RGB	*m*	*gr/cc*	*API*	*mD*	*%*	*ms*	*ms*	*%*
Max		-850	2.45	95	100	24	3800	1900	80
Min		-1500	2.2	60	10	10	2400	1000	16

Figure 38: Amplitude map (high amplitudes are colored white) of DE-Sand with wells colored and resized in order to emphasize a) depth of reservoir, b) average density, c) average gamma log values, d) average permeability, e) average porosity, f) average P wave velocity, g) average S wave velocity and h) average volume of shale. Min and max average log values are listed as well.

4.2 Quantitative Interpretation

4.2.1 Rock Physics Results

Investigating reservoir properties from the wells which are located in Field-1, Field-2 and Field-3 production locations and relating them to the Akcakoca 3D seismic data is the main objective of this rock physics study. The part of this study involves to the elastic modules. Especially, the Lamé moduli of rigidity (μ) and incompressibility (λ) and their density multiplication products of lamdarho and murho enable to extract information about rocks within the earth. Figure 36a to 36d show different lithofacies plotted as gamma ray versus density, Vp/Vs ratio, lambdarho, and murho respectively. Good discrimination exists for density values in order to separate gas saturated sands from other lithofacies. Specifically, density values lower than 2.2gr/cc can easily be differentiated however ambiguity exists between shale, marl, clay and tuff as well. Gas saturated sand – shale ambiguity is not observed in density versus gamma ray (figure36a). Vp/Vs ratio versus gamma ray does not help to differentiate neither compacted sand facies nor clay rich shaley facies. However, it does separate gas saturated sands as it is seen at figure 36b. Moreover, lambdarho versus gamma ray discriminates gas saturated sandy facies very well (figure 36c). Lambda is defined as elastic modulus of incompressibility and low value of lambdarho is interpreted as response of compressible fluid such as gas. High value of lambdarho means low compressible reservoir fluid such as water. Murho interpretation is similar to lambda but it is mostly related to lithology. Figure 36d indicates there is limited discrimination for sand and shale facies.

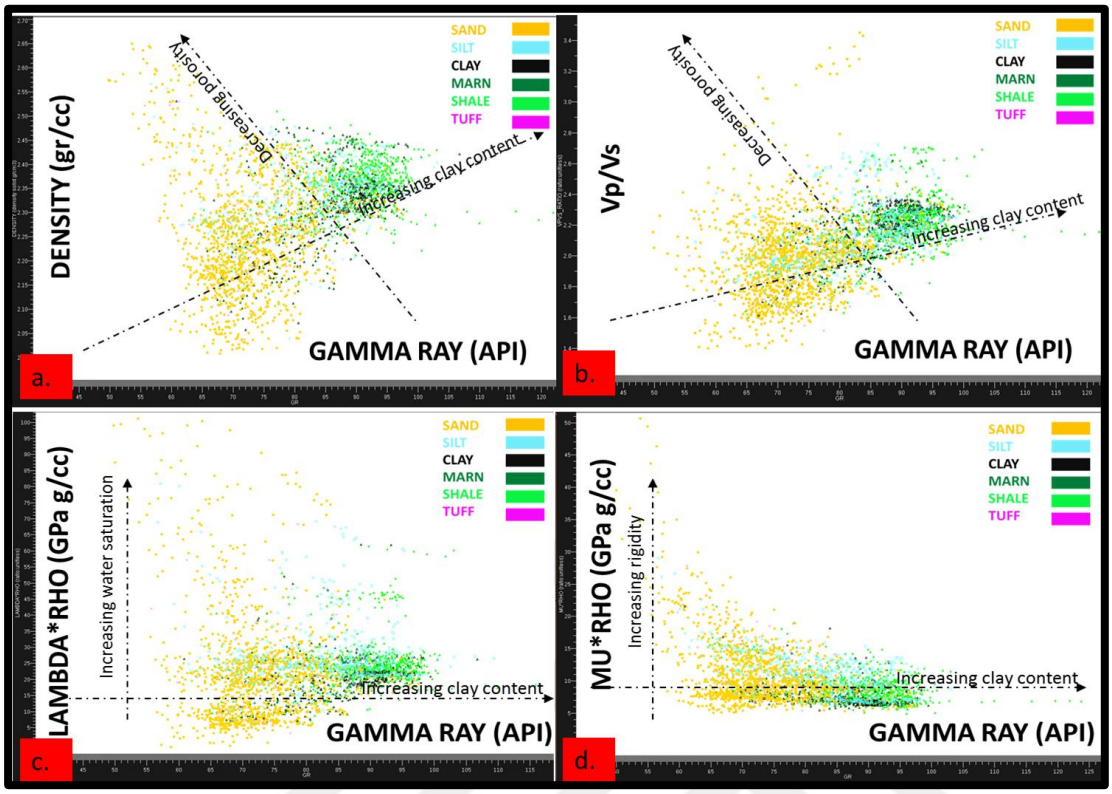


Figure 40 : a. Density versus gamma ray, b. Vp/Vs ratio versus gamma ray, c. lambda*rho versus gamma ray and d. mu*rho versus gamma ray from well logs.

In situ reservoir conditions are modeled by relating velocity and impedance to porosity and facies. For this purpose, several cross-plots have been generated. Figure 37 shows the Voigt-Reuss upper and lower bounds which are plotted over the P-wave versus porosity cross-plot for in situ reservoir. All the samples are in physical boundaries which make them reliable.

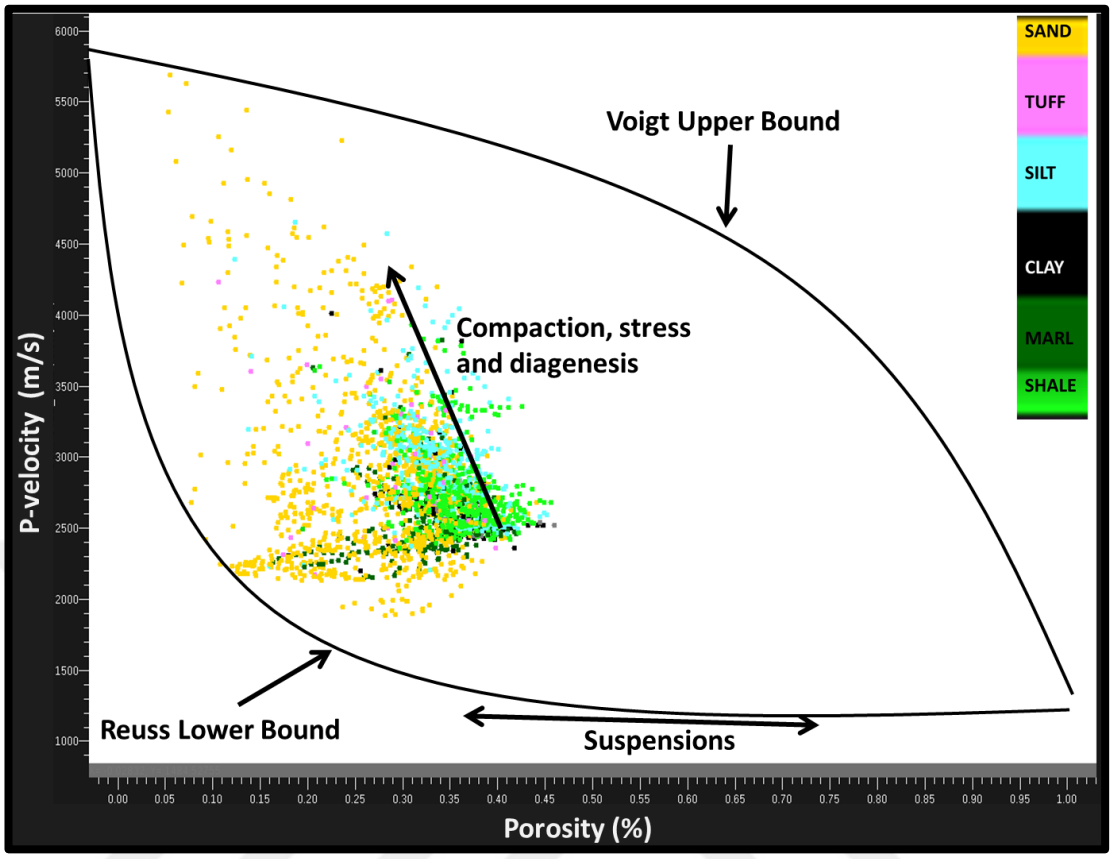


Figure 41 : P wave velocity vs. porosity for an interval between AA sand and DE sand at the type-well. Black lines show Voigt and Reuss bounds. Color bar indicates the lithology defined by composite logs for the same interval.

Several wells in the production area fortunately have the S-wave sonic log. Figure 38 shows P-wave vs. S-wave cross-plot colored with facies, density and porosity. Brine case fluid simulation shows values approach the mud rock line when their facies are predominantly shale, porosities are lower and densities are higher. However for the gas case simulation values diverge from the mud rock line trend when their facies are predominantly sand, porosities are higher and densities are lower. Finally, in situ data shows good correlation not only with gas case when facies are predominantly sand, porosities are higher and densities are lower, but also with brine case when facies are predominantly shale, porosities are lower and densities are higher.

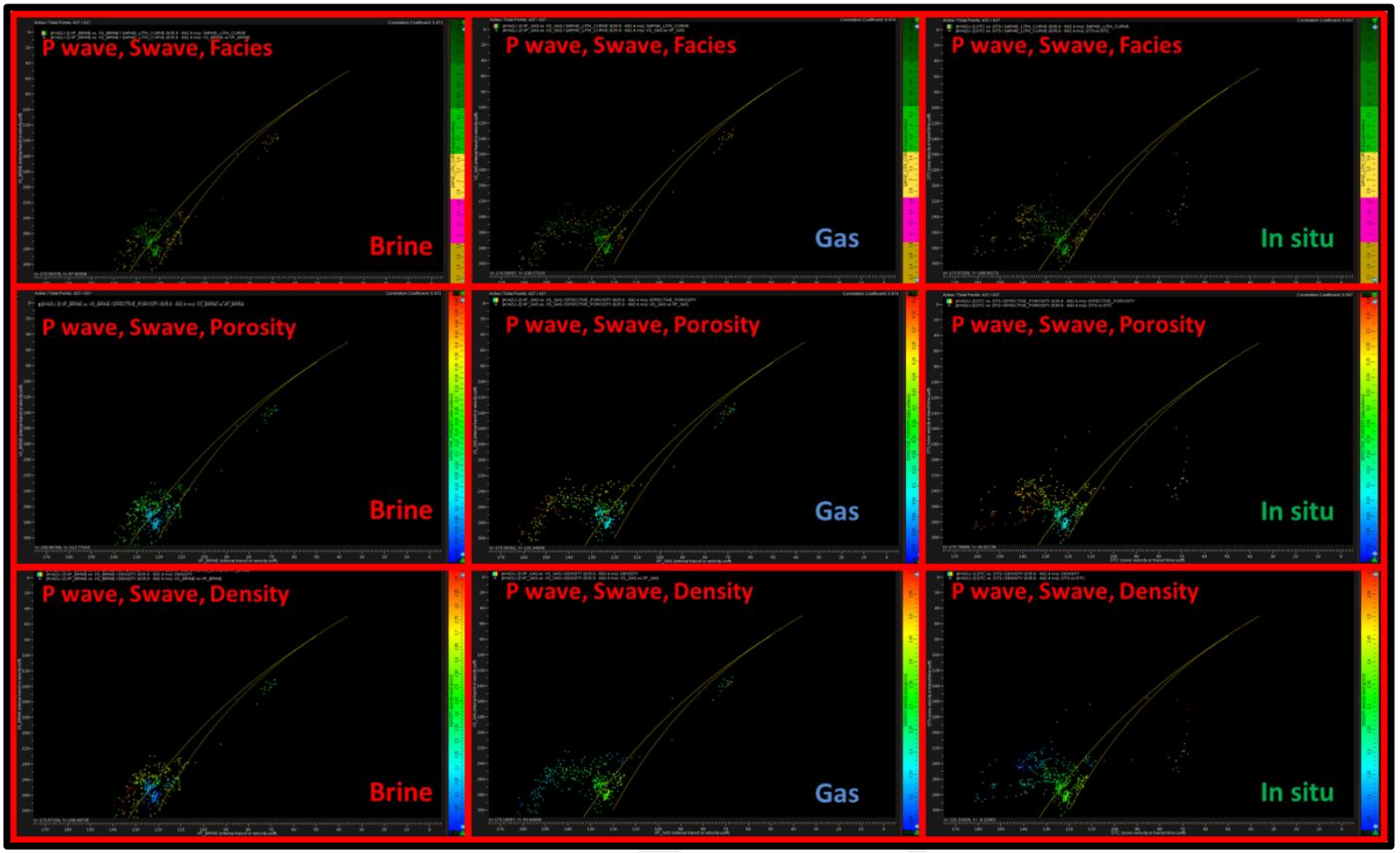


Figure 42 : P wave sonic versus S wave sonic crossplot combined with facies, effective porosity and density logs for fluid substitution brine case simulation, gas case simulation and in situ responses. Castagna's mud rock line and Greenberg-Castagna's sandstone line have been drawn for each cross-plot.

Figure 39 compares fluid sensitivity of sonic, density and porosity logs crossing. Sonic, gamma, density and porosity logs are shown in figure 39a. Figure 39b shows the sonic cross-plot with facies log. Mudrock line and Greenberg Castagna sandstone line are drawn over Vp-Vs cross-plot. Shaly facies are in the low S-wave and high P-wave trend however sandy facies are in either low P-wave – S-wave trend or high P-wave – S-wave trend depending upon the fluid content. Figure 39d shows the interpreted gas saturated, water saturated and shale dominated zones. Interpreted polygons are compared with the density porosity crossing. Red arrows in figure 39c show the perfect fit of the two different sources of fluid discriminant.

Suite of elastic logs including intercept impedance, gradient impedance, elastic impedance (30 degrees), intercept, gradient, Vp/Vs ratio, Poisson's ratio, lambda-rho and mu-rho have been generated by using well logs. In literature (Feng et. al., 2007), there are several examples of crossploting elastic properties in order to discriminate either lithology or reservoir fluid, and one of which is Lambda-rho vs. mu-rho (figure 40). Having a satisfactory discrimination at cross-plotting elastic logs for each well rises a new challenge what might be the best way of distributing this information away from the well location. The best practice is cross-plotting seismic trace-based elastic properties, bringing them to the same scale with trends which have been extracted from the wells, overlying the two data sets onto each other using well base trends, and discriminating and populating the data through 3D seismic survey as in figure 40.

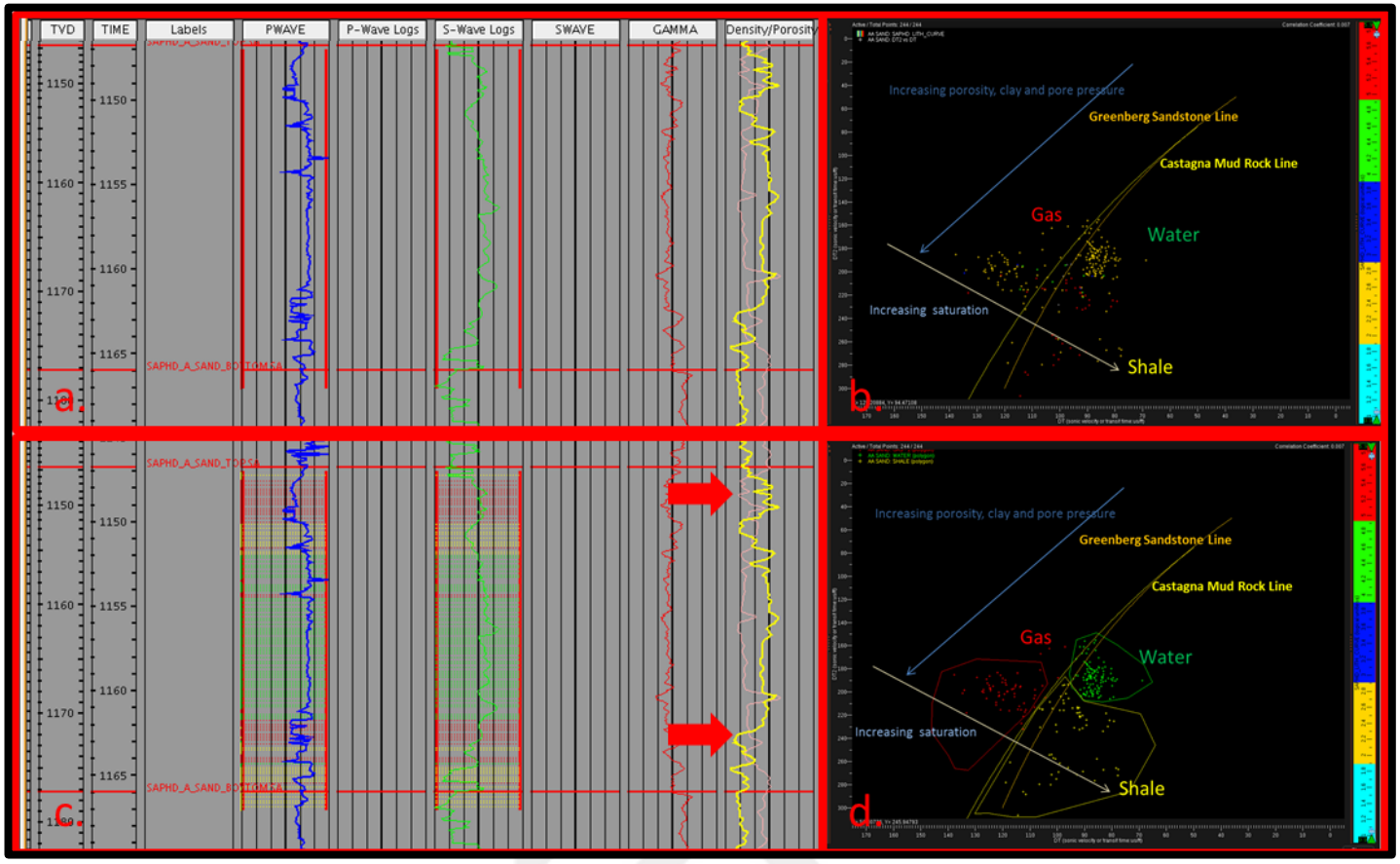


Figure 44: Fluid discrimination using sonic log responses. a. Set of logs (P-wave, S-wave, Gamma ray, Density/Porosity). b. P-wave sonic vs. S-wave sonic cross-plot with facies log. Castagna et.al. 1993 mud rock line and Greenberg Castagna sand stone lines are drawn on to the cross-plot. c. Set of logs shown in figure 18a and colors in red for gas zone, green for water saturated zone and yellow for shale dominated zone are the responses of selected polygon shown in figure 18d. d. Same cross-plot shown in figure 18b except colors are transformed to color of polygons. Any sample that falls within drawn polygons is either gas-saturated, water-saturated or shale-dominated. Red arrows indicate good fit with the gas responses of density-porosity crossing.

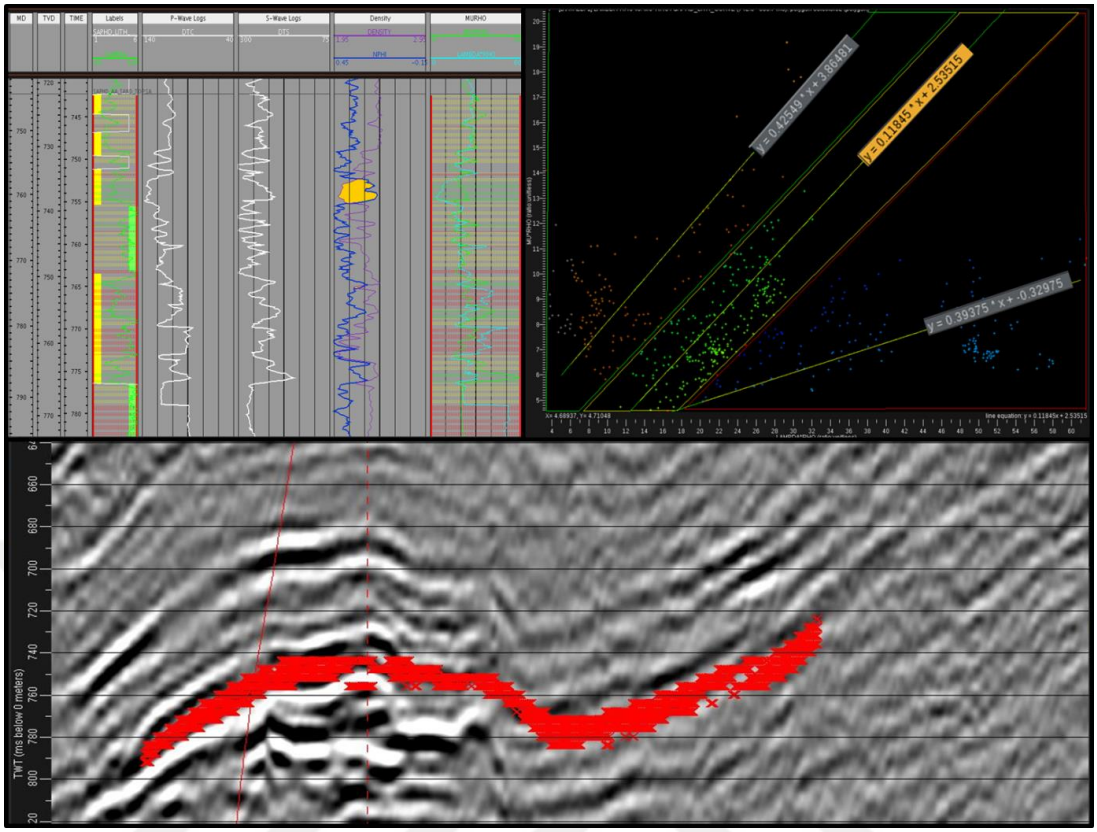


Figure 46 : Set of logs; facies (white), gamma (green), compressional sonic (white), shear sonic (white), density (purple), porosity (blue), lambda-rho (cyan) and mu-rho (green) are displayed respectively. Cross at density-porosity logs is colored with yellow in order to discriminate the gas saturated sandy reservoir. Cross-plot of lambda-rho-mu-rho is displayed with 3 polygons, green one represents gas saturated sand, yellow one represents shaly sand and red one showing water-saturated shaly sand. Each sample lying inside the polygons are drawn at vertical scale with proper color along the logs in order to show the correlated facies and fluids. Regression lines of polygons are shown with the related formula. Each formula is used while distributing the discriminated facies information through the 3D survey area. Grey scale seismic shows the well location, and red points are the distributed points from lambda-rho vs. mu-rho operation.

Density-porosity cross-plot is another way of recognizing fluid saturation in sandy reservoirs as shown in figure 41. In which two distinctive trends exist. Red line in figure 40 represents the porosity-density trend of sandy facies. Gas-saturated sandstone facies are diverged from the red line and grouped at around high porosity low density values, whereas shale trend is more stable than the sandstone trend. Shale density values are in range of 2.30-2.45 gr/cc, and change in porosity does not change the density values significantly (figure 41).

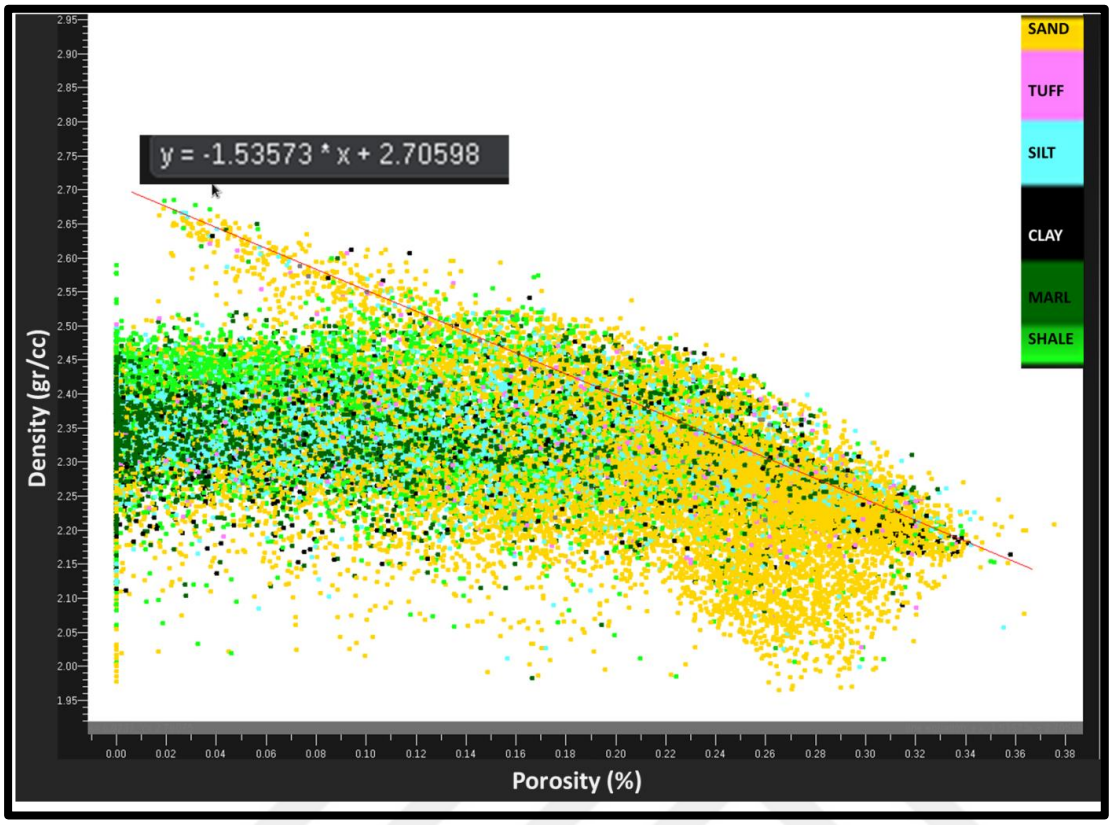


Figure 47 : Density vs. porosity within the interval between AA sand and DE sand for all wells. There is a distinctive porosity density trend shown with red line for sandy reservoirs. Color bar indicates the lithology defined by composite logs for the same interval at each well location.

4.2.2 AVO Results

Amplitude vs. offset responses of seismic reflections are interpreted as direct hydrocarbon indicators which have made the AVO method one of the major prospecting tools in hydrocarbon exploration. The evaluation of amplitude trends for each reservoir level has been completed (figure 42). AVO classification methodology is explained in chapter 3. Main amplitude response of the reservoirs in Akçakoca Field is Class III AVO. Intercept and gradient volumes are generated to form the basis of AVO classification and reconnaissance. Suite of logs is shown at figure 42. Normal incidence synthetics and offset synthetics are generated by using these logs. Offset synthetics are compared with observed pre-stack gathers and full stack. Amplitude versus offset for gas-saturated reservoir intervals are drawn with blue dots and the

underlying shaly intervals are shown with green dots. Clearly, amplitude response of the reservoir level gives class III AVO response which is identified by its increasing negative amplitude values with increasing offset.

Another AVO practice, which is shown at figure 43 which indicates a clear channelized system on a spectral decomposition map with two well locations: one is drilled and another one is considered as a prospect location. The first well which tested a gas-saturated sandy reservoir at the top gives clear AVO response. However, the same well that tested a deeper interval with amplitude reflections in seismic does not show a class III AVO response. Similarly, although a braided-looking channelized system that is characterized by a high amplitude zone to the south is also considered as a prospect area, it does not show a clear class III AVO response. Therefore, high amplitude zones in this particular prospect location are interpreted as lithology-related anomalies rather than fluid-related ones.

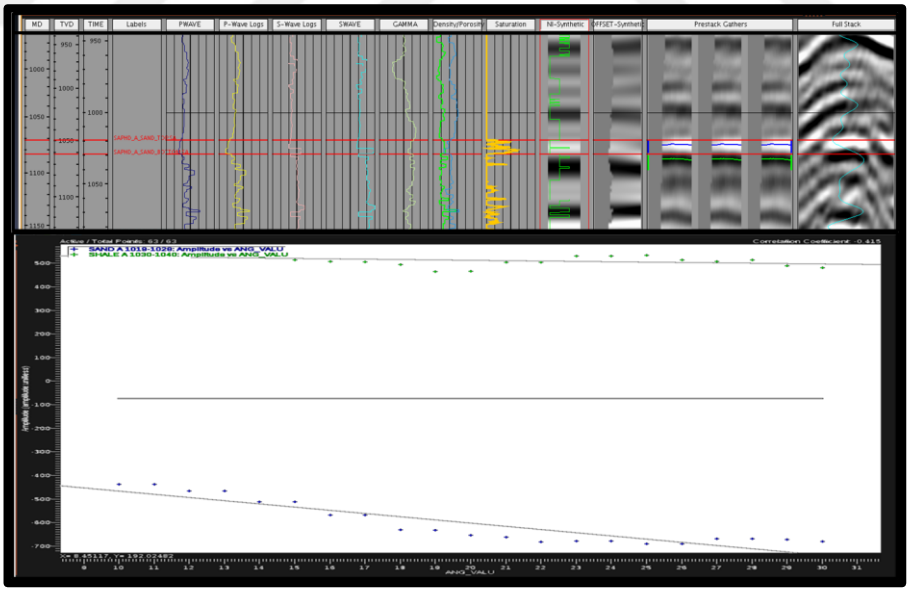


Figure 48 : Well-23, P-wave, S-wave, Gamma, Density, Porosity, and HC Saturation logs. Normal incidence synthetics and offset synthetics generated by using electrical logs. Offset synthetics are compared with observed Pre-stack gathers and full stack. Amplitude versus offset for gas saturated reservoir interval drawn with blue dots and it is underlain by a shaly interval which is drawn with green dots. Clearly amplitude response of the reservoir level gives class III AVO response which is identified by its increasing negative amplitude values with increasing offset.

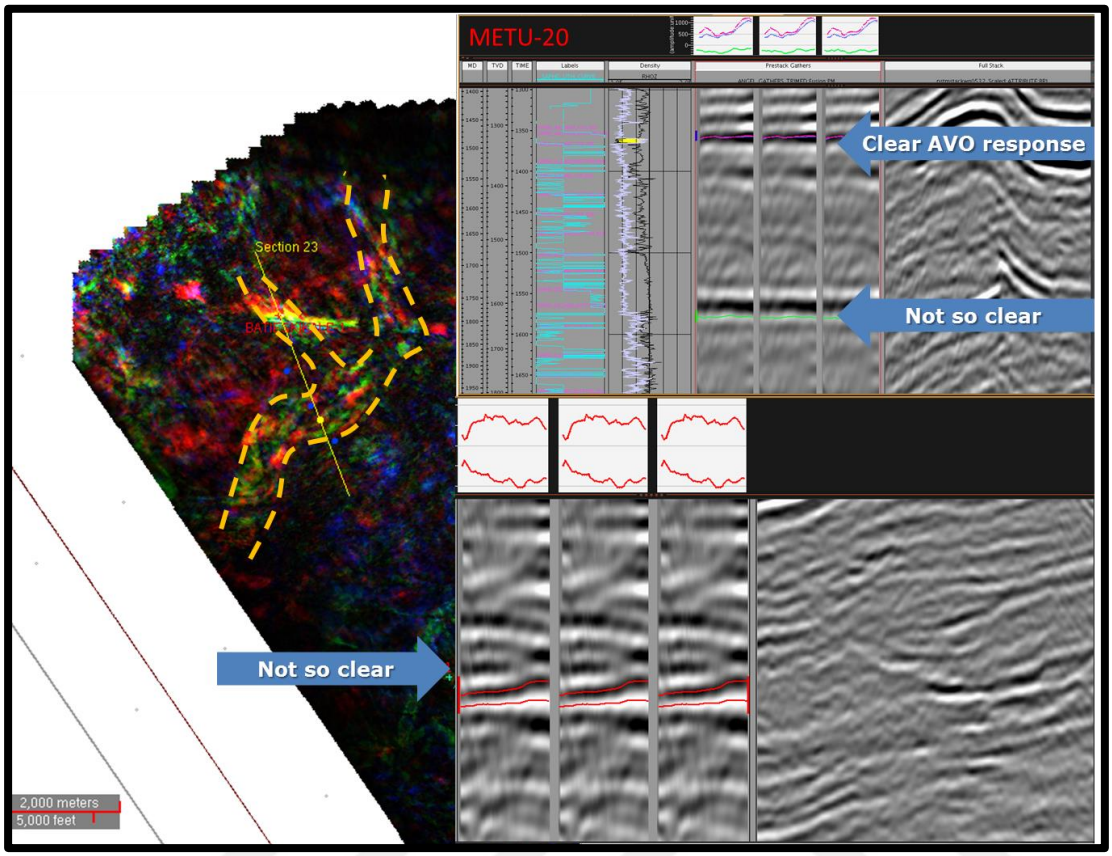


Figure 49 : Spectral Decomposition map shows a clear channelized system with two well locations, one is drilled and another one is considered as a prospect location. First well has tested one gas saturated sandy reservoir at the top, and it gives clear AVO response. However, same well has tested another deep interval which is represented by high amplitude reflections at the seismic, and it does not give a class III AVO response. Similarly, braided looking channelize system gives high amplitude zone at the south which is also considered as a prospect area, and it does not give a clear class III AVO response. Therefore, high amplitude zones in this particular prospect location are interpreted as lithology related amplitude anomalies rather than fluid.

4.2.3 Seismic Inversion Results

Seismic impedance inversion of pre-stack seismic data allows discrimination of hydrocarbon-bearing lithology. The main goal is to predict sand percentage and fluid content within the reservoir from the inversion results. During the study, commercial software (Hampson-Russell version 10.0) has been used to generate impedance inversion cubes. The simultaneous inversion has been done in order to invert pre-stack CDP gathers which can help to determine compression impedance, shear impedance and density. There are five major steps each of which are equally

important and needs to be done. These are data precondition, wavelets estimation, low-frequency model building, inversion parameters analysis, and quality control of results.

NMO-corrected pre-stack time-migrated offset gathers are obtained. Preconditioning process steps should be applied on the data set in order to increase signal to noise ratio. The noise reduction was done by band pass filtering, parabolic radon transform and trim static. After these applications, data quality is considered to be at the satisfactory level, thus, super-gather application has not been done to the data set.

Higher frequency absorption nature of the earth decreases signal to noise ratio at high frequencies. It is really hard to balance frequency spectrum for each offset. Therefore, it is better to cut higher frequencies rather than keep them in the data. The band-pass filter (2-10-40-48 Hz) has been applied to the seismic data in order to suppress the high frequencies.

The parabolic radon filter performs random noise suppression. The model parameters are set to identify the random noise within the data. After modeling the random noise, it is subtracted from the data. Results of the parabolic radon filter do not only show a data set which has a nature of reduced random noise and optimized traces, but also the waveform is better preserved at both near and far offset traces (figure 44).

The trim static process can fix migration move-out problems on pre-stack data. Therefore, trim static corrects residual move-out errors in order to align the events on the gathers. The trim statics process attempts to determine an optimal shift to apply for each trace in a gather. The shift is determined by cross-correlating each trace within a pre-defined gate to make the input trace better match.

Applying gradient analysis after radon and trim static applications, the amplitude vs. angle graphs are produced which shows reasonable results (figure 45). After the substantial noise is removed, the pre-stack time migrated offset gathers are converted into angle gather with stacking velocity values (Figure 46).

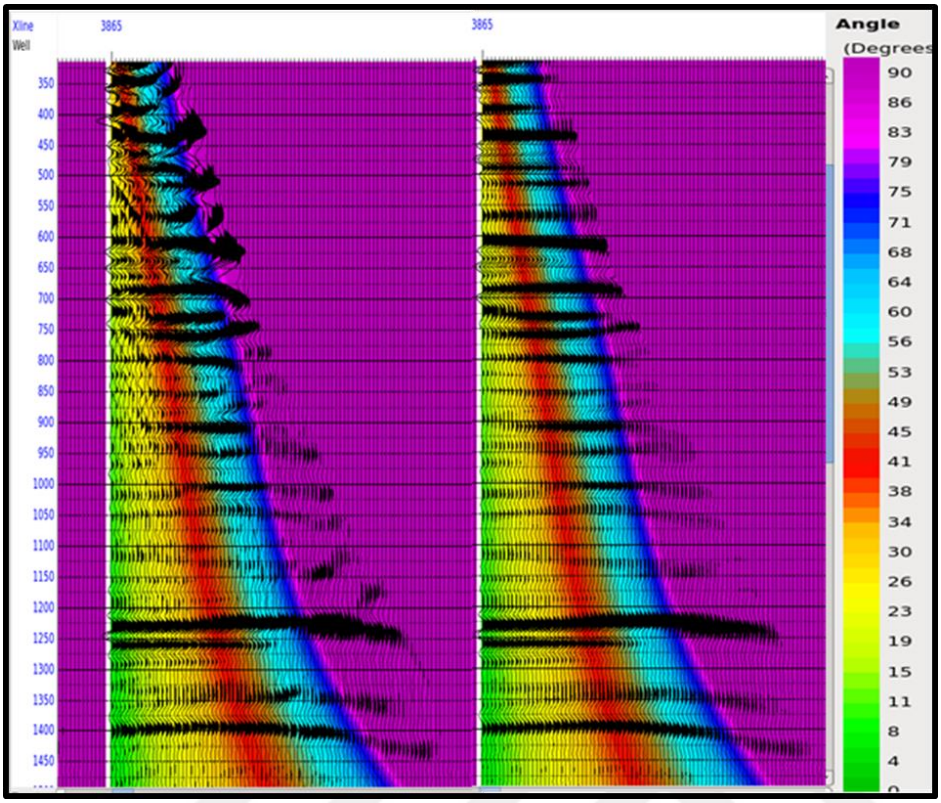


Figure 50 : A CDP gather before preconditioning and after band pass filter, radon and trim static applied. Angles are overlaid on to the gather as color coded.

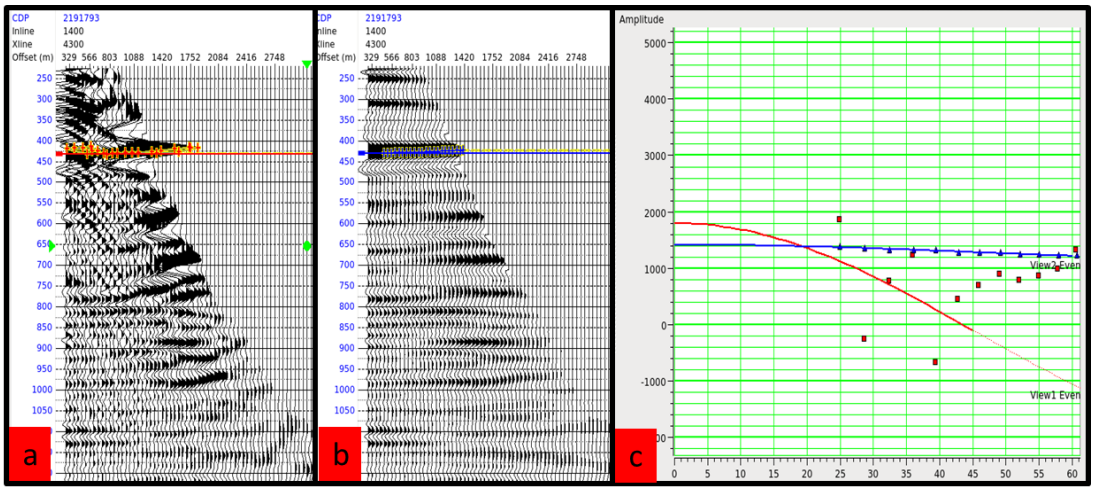


Figure 51 : Gradient analysis. a. a CDP gather before pre-conditioning. b. a CDP gather after band pass filter, radon filter and trim static applications. c. Gradient curves, amplitude vs. angles. Red line is plotted by using cdp gather before pre-conditioning and blue line is plotted by using cdp gather after conditioning.

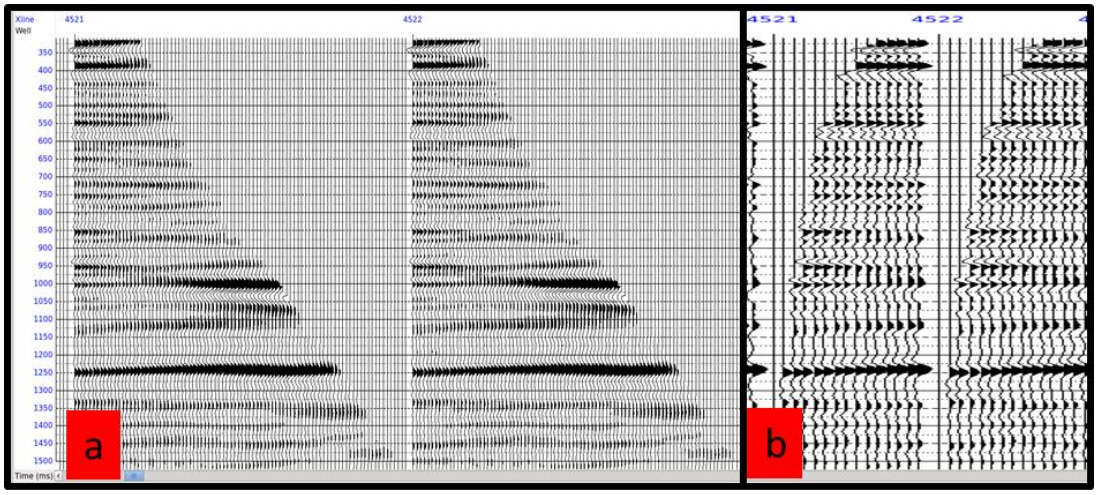


Figure 52 : CDP gathers. a. Pre-conditioned offset gathers. b. Pre-conditioned angle gathers.

Well logs are correlated with the seismic data for getting the same time alignment of the events. Reasonable time-depth relationship should be established to convert the log data in depth domain into that in time domain. First, statistical wavelet is extracted which only depends on seismic (figure 47a). After obtaining good seismic to well correlation, the reasonable wavelet is estimated depending upon the wells for each angle groups. Three set of wavelets are extracted from the seismic volume in order to use at pre-stack inversion. One is from 0 to 10 degrees, averaged at 5 degrees, the other one is from 10 to 20 degrees, averaged at 15 degrees, and last one is from 20-30 degrees, averaged at 25 degrees (Figure 47b).

QC of pre-stack inversion result has been done (figure 49). P wave impedance at a well location colored in blue and inversion result at the same location colored in red. An offset synthetic is generated by inversion results and correlation between synthetic and observed seismic is in satisfactory level (Corr=0.971322).

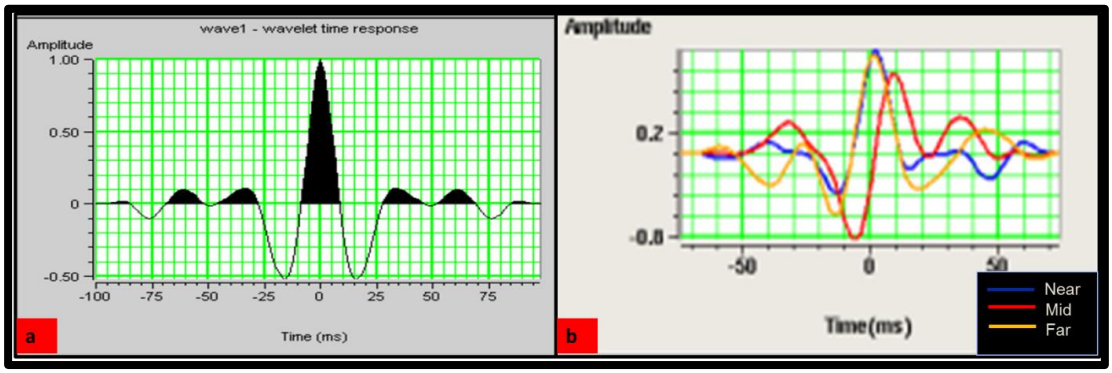


Figure 53: Estimated wavelets a. Statistical wavelet. b. Near, mid and far offset wavelet estimation.

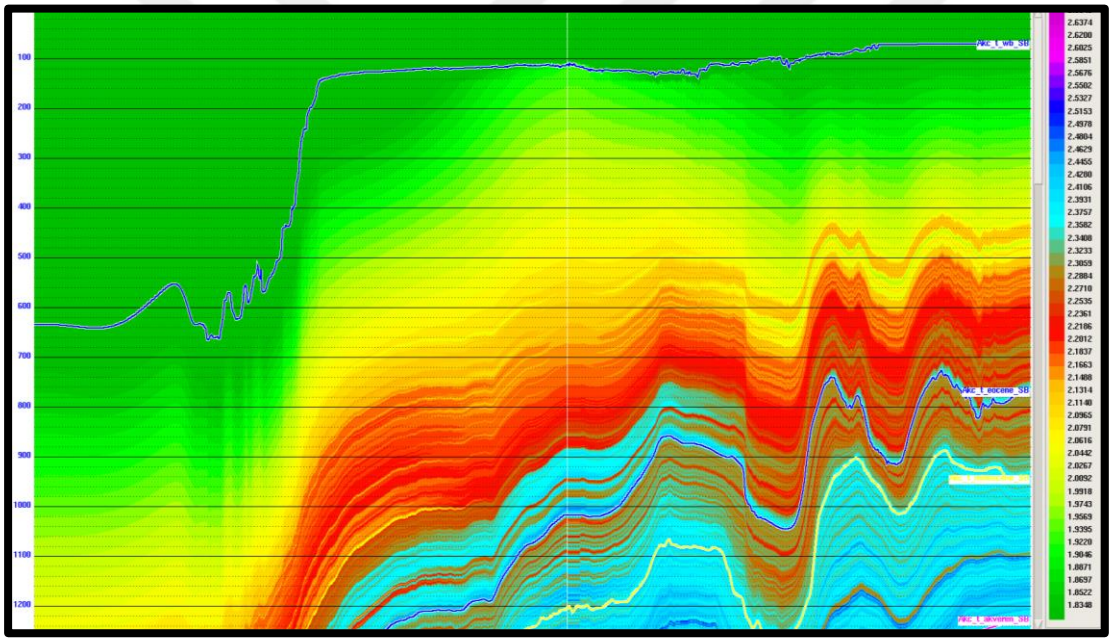


Figure 54 : Initial P-wave impedance model used for post and pre-stack inversions.

Three different post-stack inversion algorithms have been run on the 3D data, and compared with the pre-stack simultaneous inversion results (figure 51). All of the inversion results for P-wave impedance are produced by an initial P-wave impedance model (figure 48).

Model-based and sparke spike post-stack inversions are pretty similar; however, band limited post stack inversion does not look geologically reasonable. Pre-stack inversion obviously has more frequency content compared to post stack inversions which can be seen both in figures 51 and 52 as well. Products of pre-stack inversion are P-wave impedance, S-wave impedance and density volumes. Initial S-wave impedance and density model are generated separately. Moreover, Vp/Vs, Possion's ratio, mu-rho, lambda-rho P-wave reflectivity and S-wave reflectivity volumes are created by using related formulas explained in chapter 3.

Low P impedance values represent high probability of gas-saturated sands within the A Sand interval (Figure 50a). There is no significant anomaly in S-wave impedance which may imply fluid saturation (figure 50b). Vs values do not change due to fluid saturation for reservoir intervals, however Vp values can significantly drop creating an anomaly in Vp/Vs ratio. This can be detected in the Vp/Vs ratio map for A Sand interval (figure 50c). Low Vp/Vs ratio is represented by red color. Gas-saturated reservoirs should be characterized by low density values which are colored in red in figure 50d.

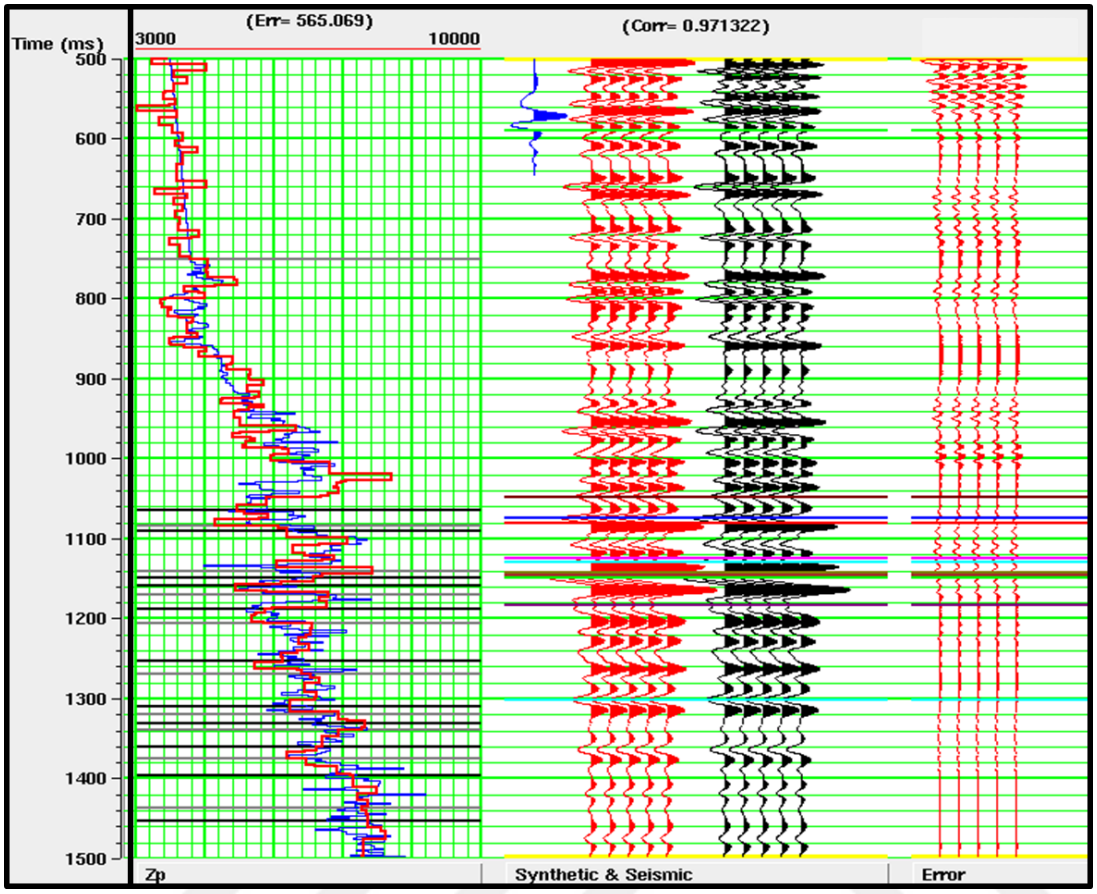


Figure 55 : QC of inversion result. P wave impedance at a well location colored in blue and inversion result at the same location colored in red. An offset synthetic is generated by inversion results and correlation between synthetic and observed seismic is in satisfactory level (Corr=0.971322). Error is plotted in red for further QC.

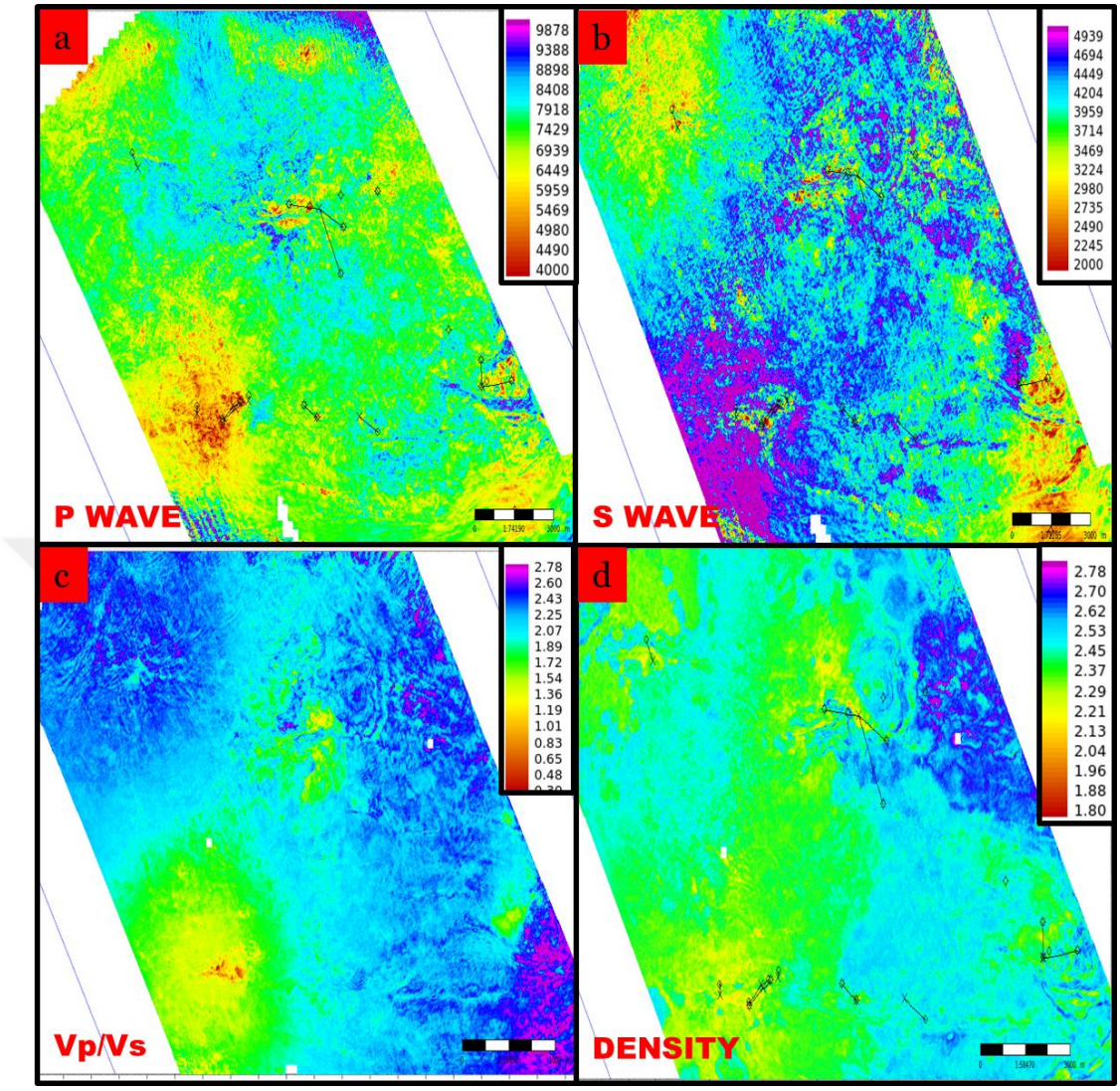


Figure 56 : Pre-stack simultaneous inversion results. a. P wave impedance b. S wave impedance c. Vp/Vs ratio d. Density horizon slice at A Sand.

Figure 52 specifically shows that any derivative of the pre-stack inversion results (lambda-rho, mu-rho) have more frequency content than the acoustic impedance. Simplified representation of the initial model, post stack and pre-stack inversions are seen in figure 52b. Initial model fills the low frequency gap which, in general, seismic does not. Pre-stack inversion offers more high frequency content than post-stack inversion. Thus, pre-stack inversion is superior to the post stack inversion.

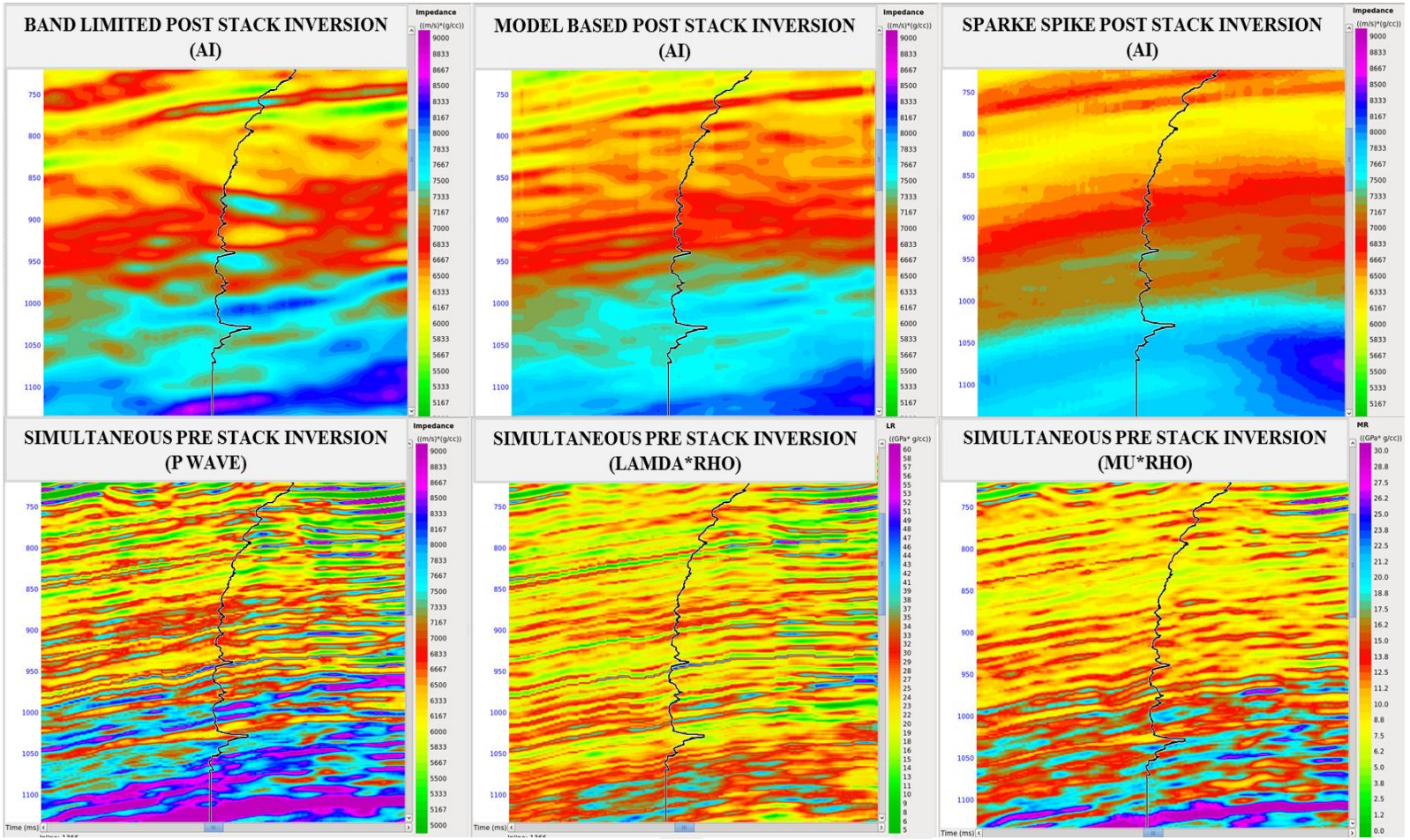


Figure 57 : Band limited, model based and spark spike post stack inversions at the top row and simultaneous P-wave, lambda-rho and mu-rho pre-stack inversion results are at the bottom row.

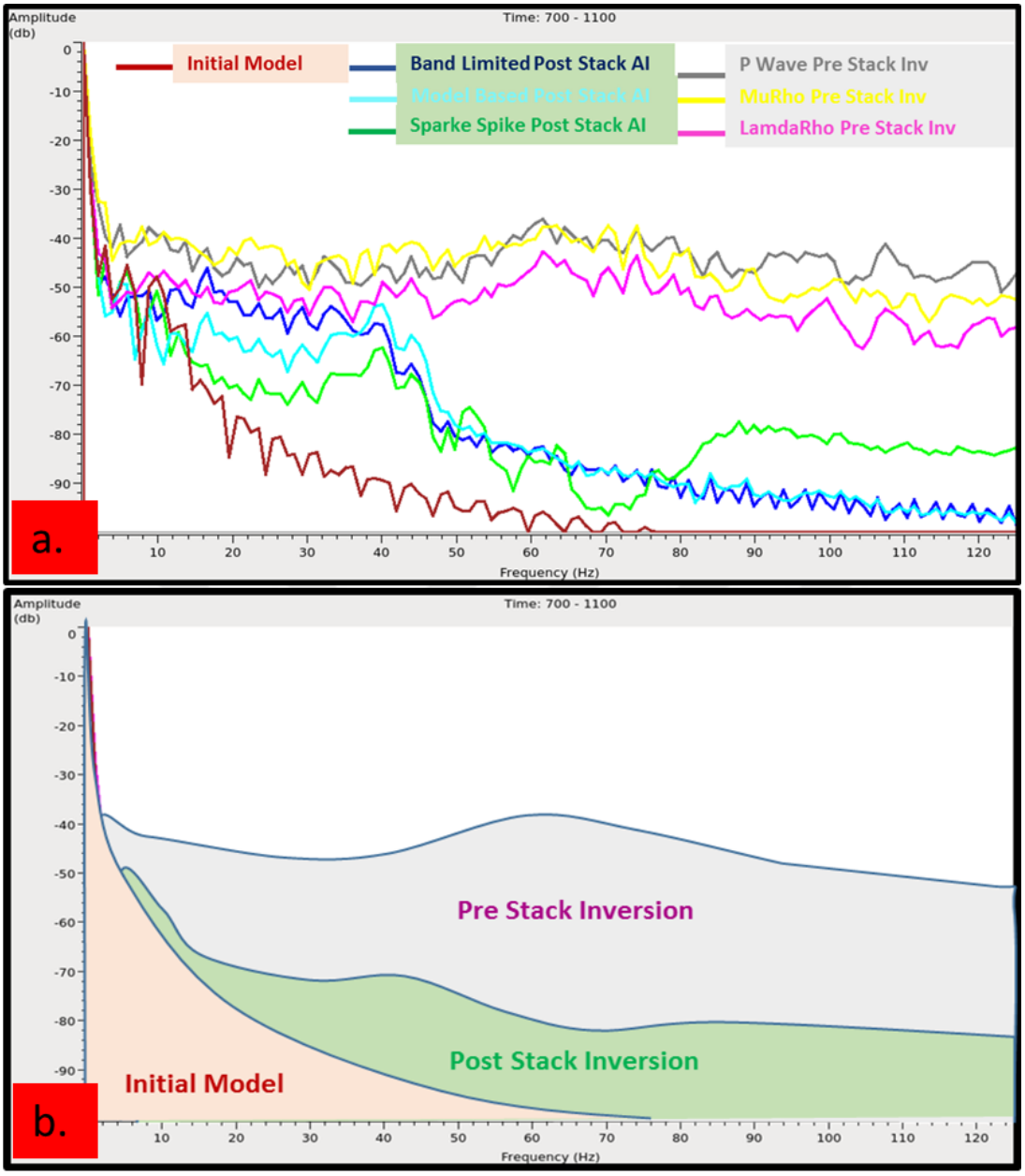


Figure 59 : Frequency spectrum of the initial model, post stack and pre-stack inversion impedance results. a. Comparison of the different inversion algorithms b. Simplified representation of the initial model, post stack and pre-stack inversions. Initial model fits the low frequency gap which seismic in general does not have. Pre-stack inversion offers more high frequency content than post stack inversion. Thus, Pre-stack inversion is superior to the post stack inversion.

4.2.4 Forward Modeling for the Blind Test Well Location

Convolution base forward model has been applied to the blind test well location at Field-4 in order to understand sensitivity of models produced by inversion or simulation. The procedure requires velocity and density information which are derived from inversion results.

Figure 53 shows the P-wave, S-wave, density, AI logs and their simulated versions. Upper part of the simulated P-wave log slightly diverges from the realization of the P-wave log although the lower part fits pretty well. This is explained by fluid effect, since all the simulations that have been run on the survey area are calibrated with the facies model which is not sensitive to the fluid itself. Similar interpretation is true for the density log as well. Simulated density log shows higher density values for upper part of the reservoir at the well location. It is already known that the upper part of the reservoir for blind well tested a gas bearing sandstone which is not represented very well with the simulation results.

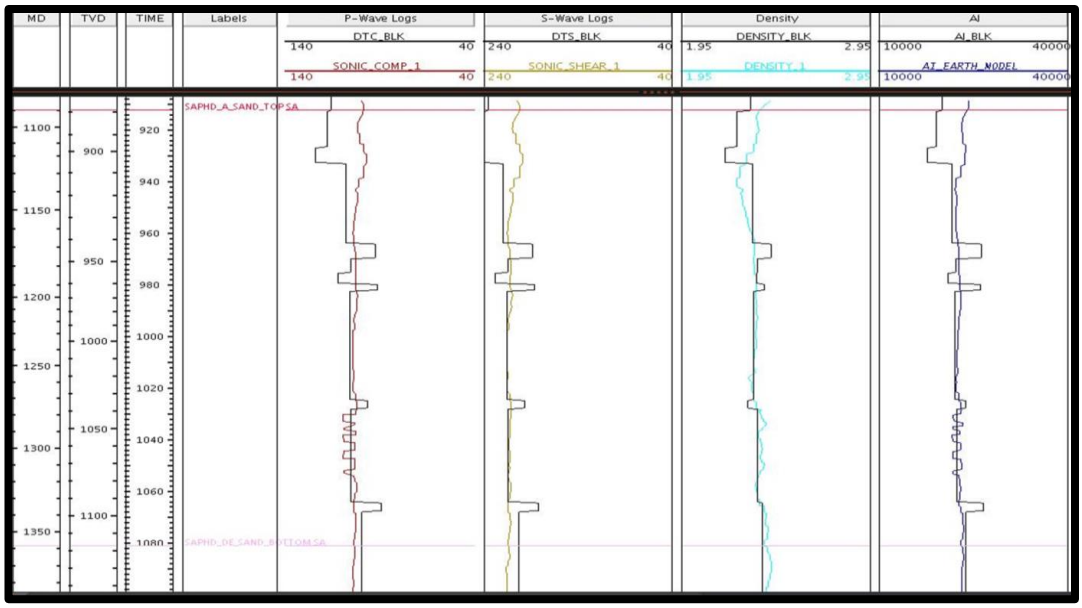


Figure 60 : Logs of the blind-well vs. simulated well log results between A sand top and DE sand bottom. P-wave, S-wave, density and calculated AI are colored in black for input logs. SGS reservoir property results are in red for P wave, yellow for sonic, cyan for density and blue for AI respectively. Simulation results show quite good fit to the input curves even though the well and its logs were not got into the simulation.

Rock physics, AVO and inversion have been applied to the data set. Results from the rock physics application at the study area can be concluded that the data follows the empirical boundaries, gives a good response to the fluid substitution which may help to recognize gas-saturated reservoirs far from the tested locations and distribute this information along the 3D survey area.

AVO practice in the study area shows how clearly the reservoir levels are correlated with the classified data. Moreover, it helps downgrade prospective locations which do not show any clear AVO response. Distributing any trend from the AVO results is possible along the 3D survey area but it is really important to highlight that there might be several other trends which give similar acoustic responses with the response that are observed in the data.

Post and pre-stack inversion have been run on the seismic data and the results reveal that pre-stack inversion is superior to the post-stack inversion in terms of frequency content and reliability.

Simultaneous Inversion results are the process of inverting pre-stack CDP gathers for P impedance, S impedance, and density at the same time. Pre-stack inversion has been run on the input which is noise-reduced angle gather data. Processing window has been chosen as Sand A to Sand F which are ultimate top and bottom of the multi-reservoir packages, respectively models of P impedance, S impedance and density are used to constraint the inversion results. Angle dependent wavelets are used.

Each of the applied quantitative methods has produced an intermediate result, but overall, this products are constrains of the final earth model. For example, a density volume for the 3D survey area already exists, but it is in seismic scale, and there are several other solutions, which might give the same seismic response. This phenomenon is called *non-uniqness*. Knowing that our products are not unique, these products with certain amount of correlation to the solid data are used as constraints to the final earth model which is close to the well log scale.

4.3 Facies Analysis

Originally, 6 different facies have been identified from cuttings. Their physical properties have been explained in chapter 2. These are basically elements of deep marine turbiditic system. Walker's conceptual model for submarine fans is represented by clean sands, shaly sands, silty shale and shale (figure 54). Generated facies log have been redefined before going any further in modeling. The marl and shale facies have been merged since their physical definitions were pretty close to each other. It may also be considered that sandstone facies is Walker's clean sand, siltstone is shaly sand, claystone is silty shale, and shale is shale. Therefore, a second correction has been needed to transform these definitions to Walker's model. After this correction, a new set of lithotypes has been defined. Figure 55 shows each facies and their percentage in related intervals for the first facies. As it was previously explained, at well correlation section, each sandy interval has been identified and named as Sand AA, A, B, C, D, DE, E, F. Statistical representation of the samples seen in figure 55 shows that sand intervals have more than 50 percent sand, and only first two intervals have tuff facies with a small amount. Each interval between sandy reservoirs consists of more than 70 percent shale and clay contents.

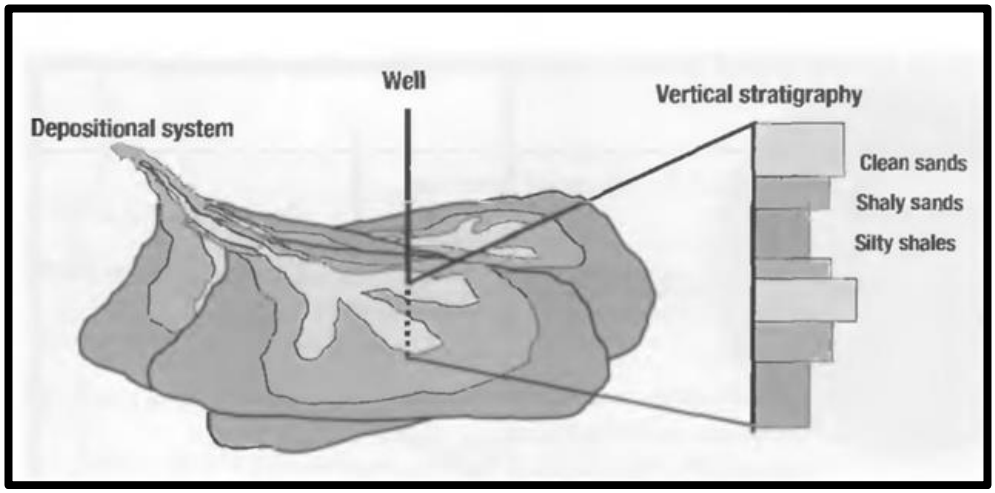


Figure 61 : Walker's (1978) conceptual model for submarine fan.

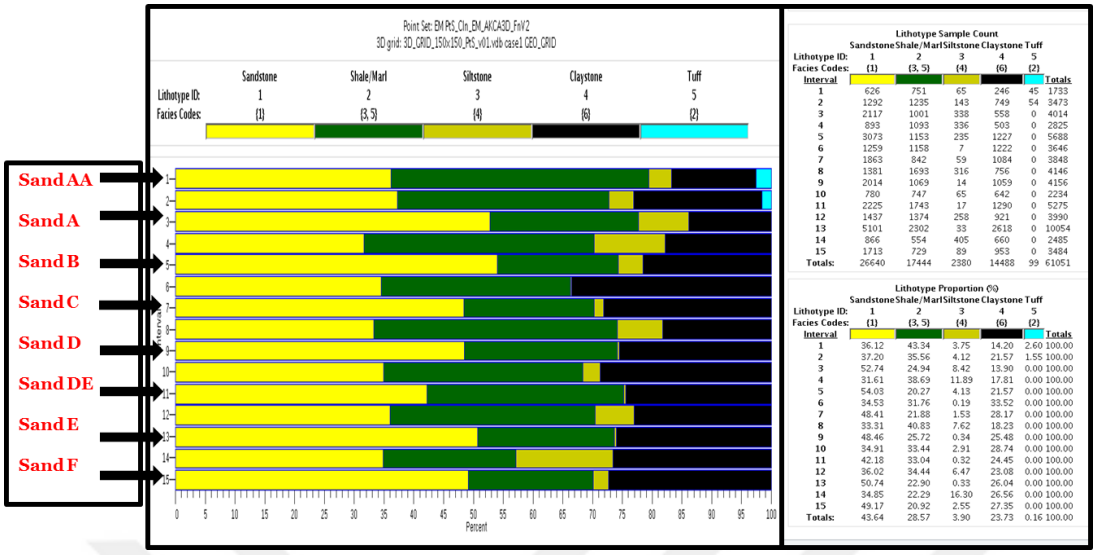


Figure 62 Facies codes with their sample counts and proportions shown for each interval.

4.4 Geostatistical Modeling

A 3D geostatistical reservoir model has been built for the Akçakoca Production Field with 20 wells plus a 3D seismic survey data and its derivatives using commercial software (DecisionSpace Geosciences 10).

Earth modeling strategy is summarized in figure 56. So far, seismic interpretation and quantitative seismic interpretation techniques have been discussed, and several products have been generated. One of the generated products is a 3D grid which consists of interpreted horizons, faults and fluid contacts. Grid dimension is 150 m in both horizontal directions and 2 m in vertical direction. This 3D grid is the skeleton of the earth model (figure 57). Since the reservoirs in the study area are shaped by compressional deformation, thrust faults should be nicely represented in the 3D grid. Figure 57a shows that 3D grid handles thrust faults very well. In order to build a proper Earth model, at first, data conditioning should be done before any facies or petrophysical simulation is run.

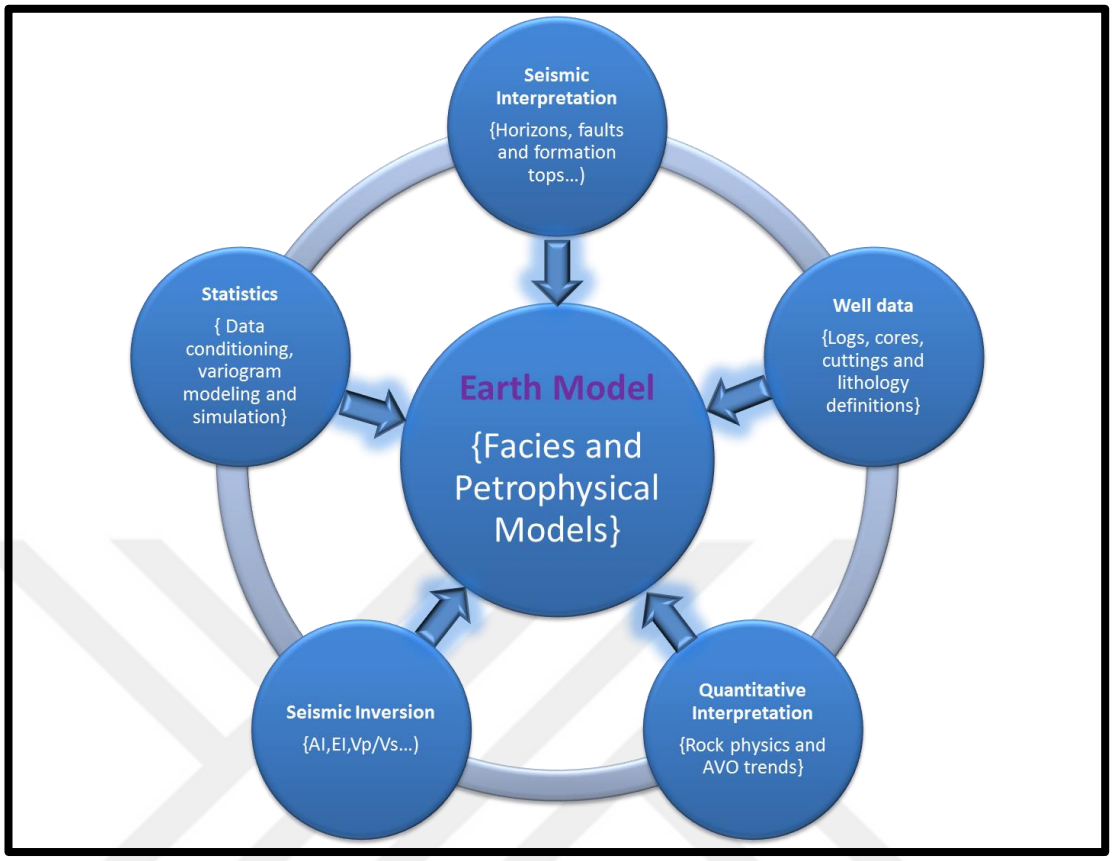


Figure 63 : Earth modeling work flow.

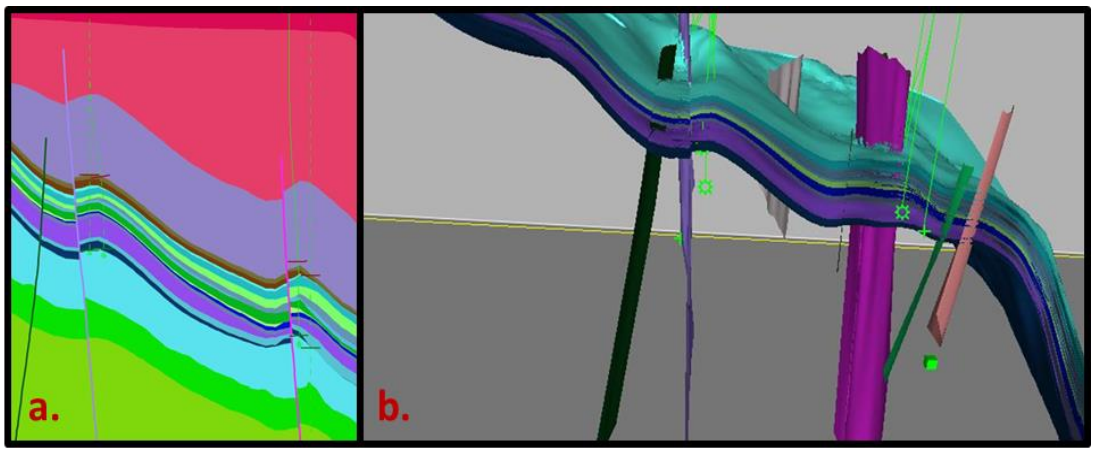


Figure 64 : a. A section view of 3D grid and b. A 3D view of 3D grid which indicates related faults and reservoir surfaces.

4.4.1 Data conditioning

Data conditioning starts with editing the existing logs such as gamma ray, compressional sonic or shear sonic. For example, gamma ray editing has been done at the beginning of the modeling. Since the wells are drilled in different times and with various tools, their gamma ray responses are in a wide range (figure 58).

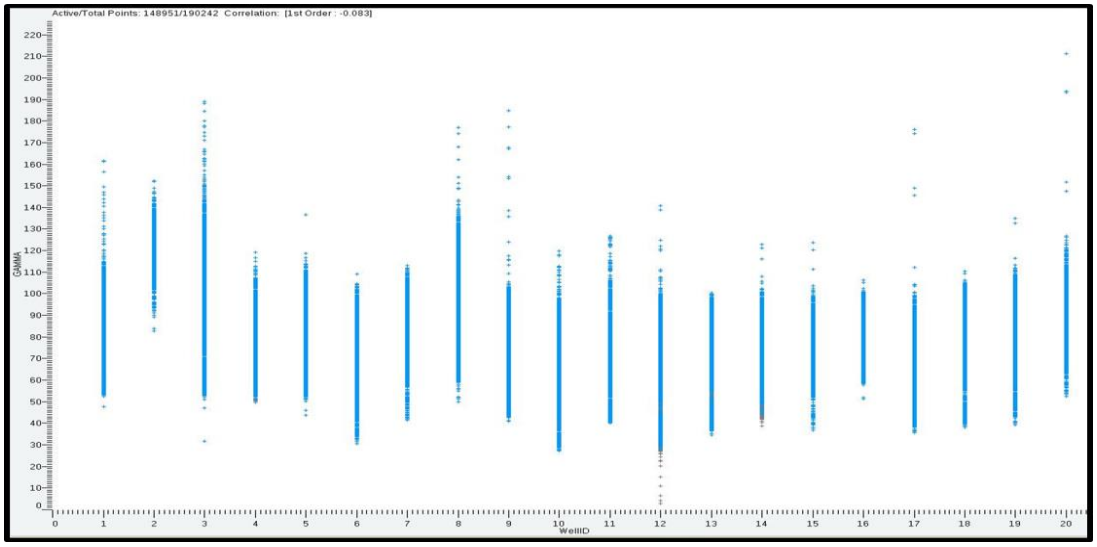


Figure 65 : Gamma values versus wells. Variety of gamma log responses indicates that it is hard to be drawn a common constant shale line on these logs.

Gamma values versus wells indicate that an editing is needed. Editing strategy can be summarized as first filtering out the gamma log responses with the parameter of 200 m minimum thickness, which indicates that if anything thinner than 200 m is considered as residual, then the rest of the gamma ray values belong to the main radioactivity trend. Second, filtered log is subtracted from the original log values, and the results show that the residual is only sensitive to lithology thinner than 200 m (figure 59).

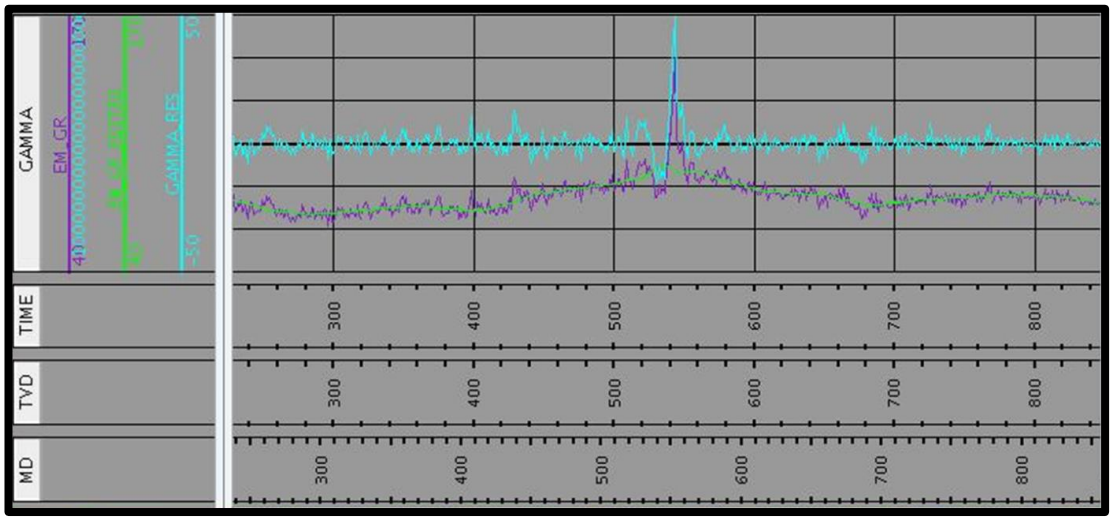


Figure 66 : Gamma values versus MD, TVD and TIME function. Purple line shows original gamma log and green line indicates highly smoothed or filtered gamma log and finally cyan line shows subtracted values of gamma logs.

As soon as residual values are generated, it can be scaled such that minimum values are located at zero and maximum values located at 100. Later on, lines which are the indicators of grouping pure sand, shaly sand and pure shale values are generated. In order to crosscheck these newly generated residual gamma ray logs, they are plotted together with effective porosity curves and any zone which has high porosity and low gamma ray values is colored in yellow, indicating sandy lithology. These yellow zones are then overlain onto the composite log. Consistency between composite log and residual gamma ray values are recognized easily, and it is in acceptable range (Figure 60).

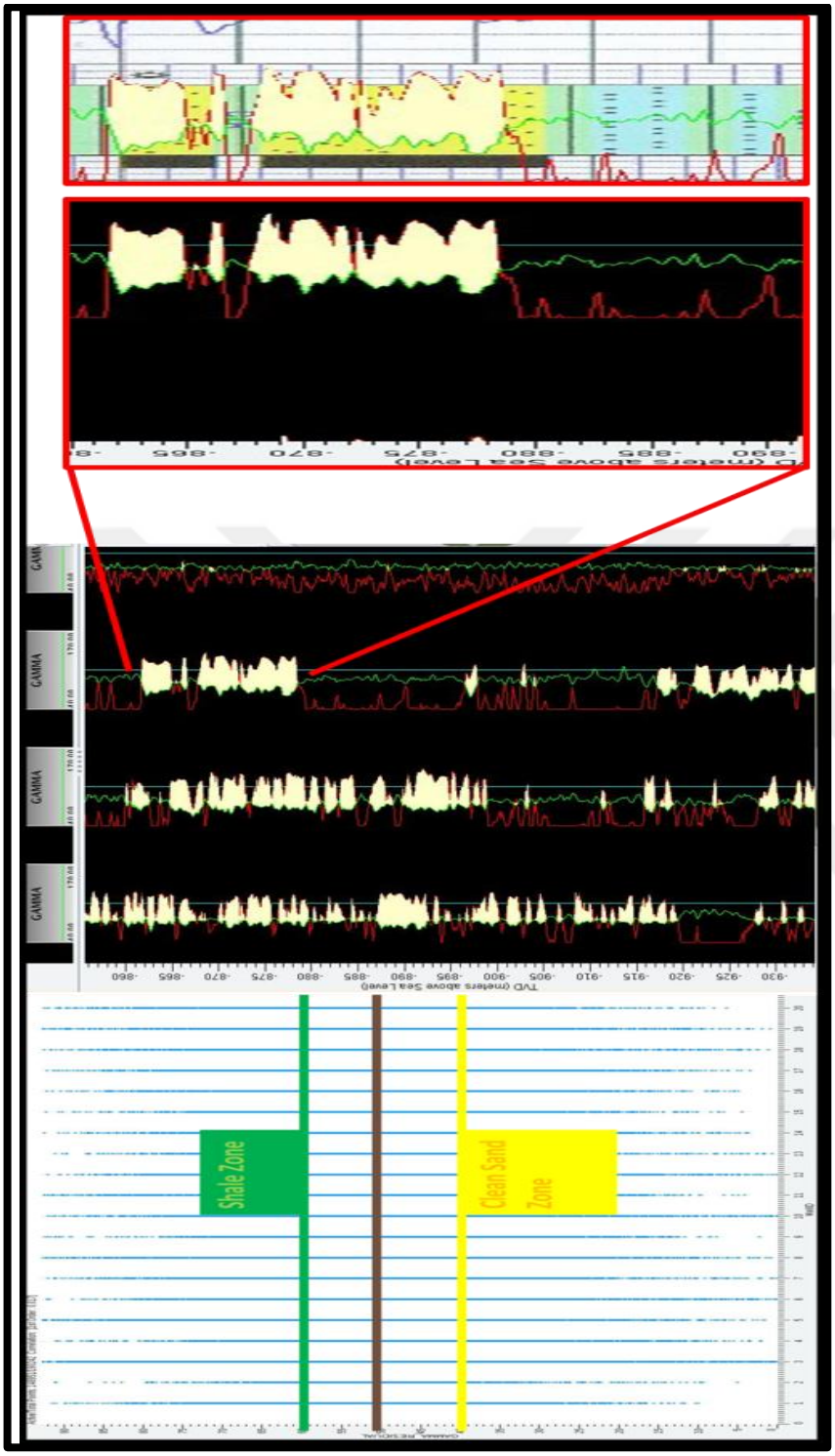


Figure 67 : Residual gamma values versus wells. Scaled gamma ray values are between values of zero to 100. Any value smaller than 40 represents pure sand lithology and any value bigger than 60 represents pure shale lithology. In order to crosscheck these newly generated residual gamma ray logs, they are plotted together with effective porosity curves and any zone which has high porosity and low gamma ray values colored as yellow. Yellow zone indicates sandy lithology. These yellow zones overlay onto the composite log in order to compare them at close up view.

Histograms indicate how frequently our data occurs within a certain range for the data set. The log responses are cross-plotted with lithology or facies logs due to discriminate log values for a given lithology. Figure 61 shows the density log values cross-plotted with facies log, and result gives the each group of density values for given lithology such as sand, shale or marl. Figure 61h shows two distinctive apexes in density histogram of siltstone lithology which might be interpreted as fluid effect unless siltstone reservoirs are fed by two mineralogically different sources.

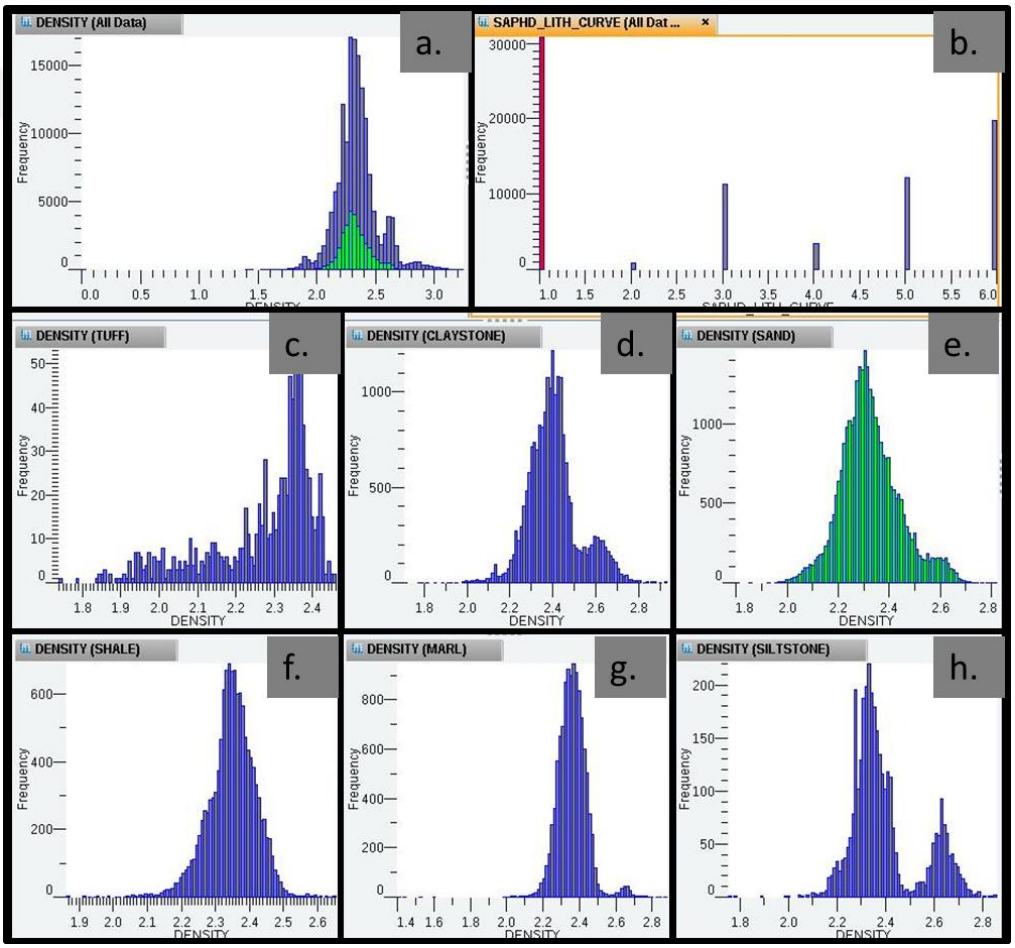


Figure 69 : a. Histogram of density log values at all zones and wells. Green bars indicate sandstone density values b. Histogram of facies log values which simply sand=1, tuff=2, siltstone=3, claystone=4, marl=5, and shale=6. c. Histogram of density values for tuff only. d. Histogram of density values for claystone only. e. Histogram of density values for sand only. f. Histogram of density values for shale only. g. Histogram of density values for marl only. h. Histogram of density values for siltstone only.

The outlier box plot is a graphical summary of the distribution of data. The ends of the box represent the 75th and 25th quartiles which are also expressed as the 3rd and 1st quartile respectively. The difference between the 1st and 3rd quartiles is called the *interquartile range*. Outlier analysis is the way that log values are cleaned up from the outliers (figure 62). Figure 62c shows density distribution for each well. Except the first well, wells align on the 2.3-2.4 gr/cm^3

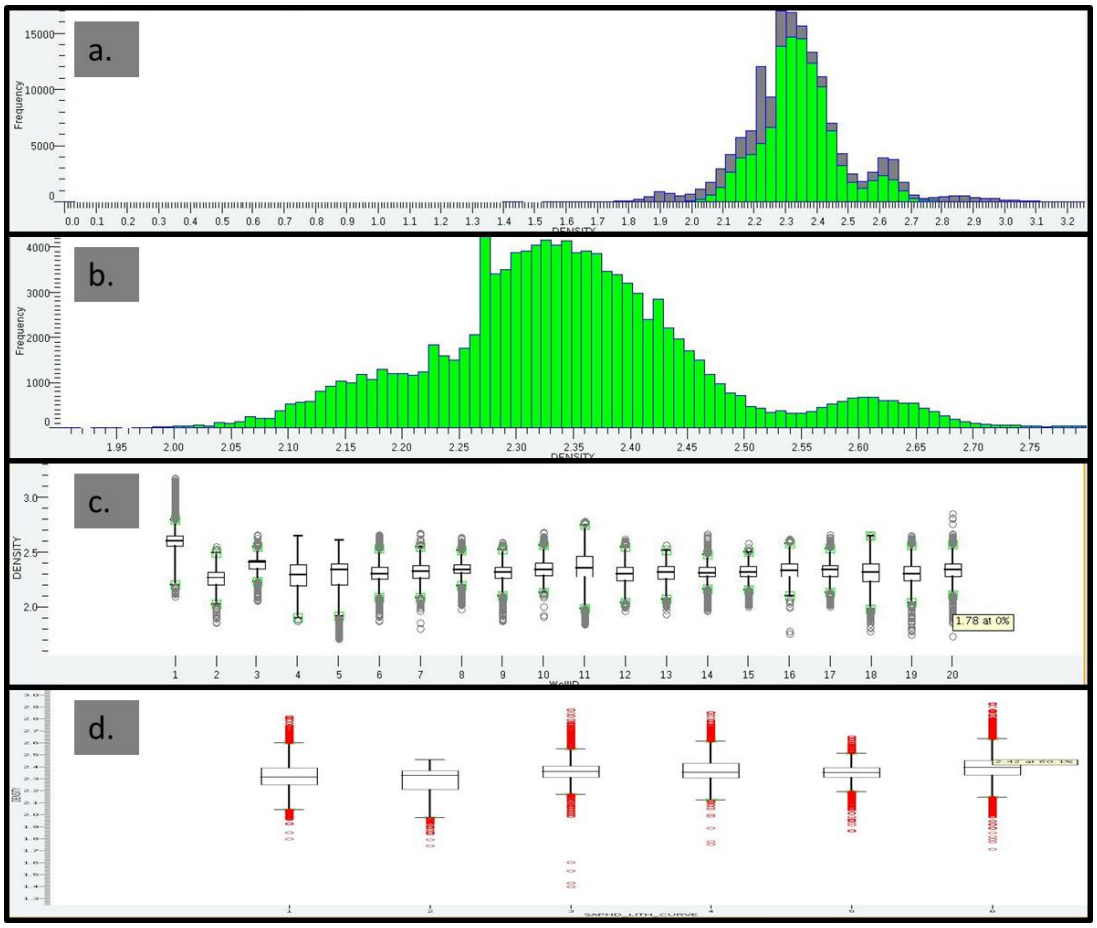


Figure 70 : a. Density histogram of all logs before outlier analysis. b. Density histogram of all logs after outlier analysis. c. Multi-well outlier analysis of density. d. Multi facies outlier analysis of density.

Plotting log values with their own normal distribution values is called Q-Q plot, and chi test indicates if the values are normally distributed or not. Figure 63 shows Q-Q plot of porosity values. Figure 63a for all facies, figure 63b for only sandstone facies, and figure 63c for sandstone facies after editing, and their chi test results indicate that none of them are normally distributed.

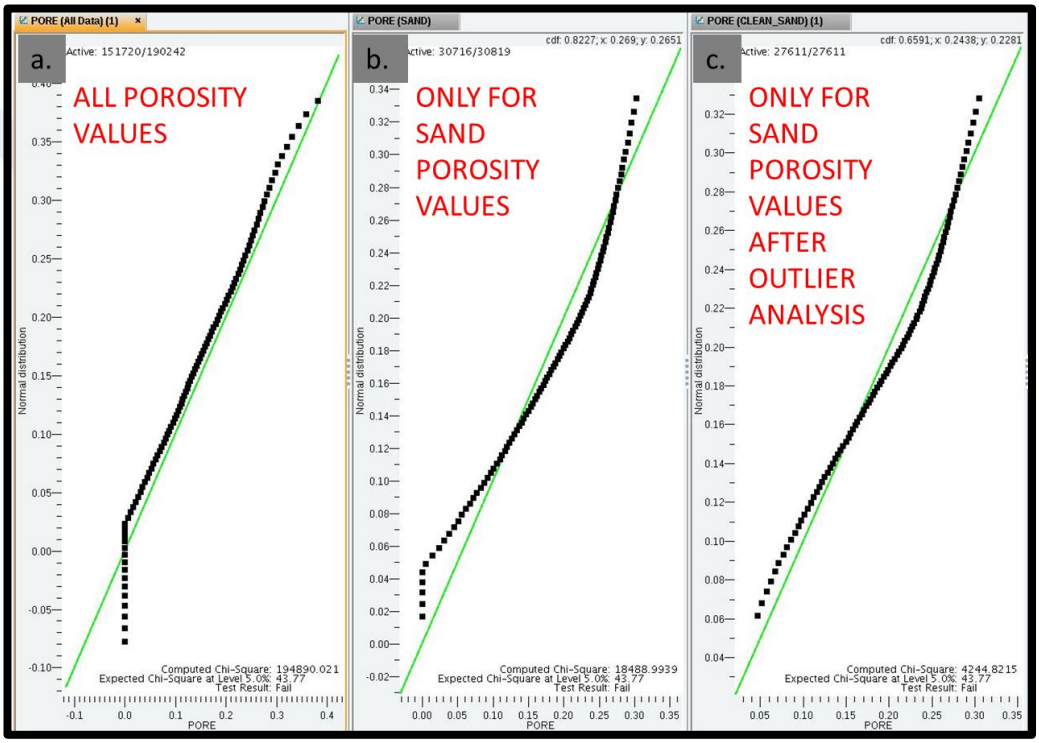


Figure 71 : a. Q-Q plot for all porosity values. b. Q-Q plot only for porosity values of sandstone reservoirs. c. Q-Q plot only for porosity values of sandstone reservoirs after outlier analysis. Each plot has its own chi test results, and none of them passes the chi test which simply indicates that porosity values are not normally distributed.

The semivariogram depicts the spatial autocorrelation and distance of two measured sample points. Once each pair of locations is plotted, a model which is fit through them is called variogram modeling. Variogram modeling for facies and petrophysical properties has been done vertically and horizontally. Parameters of each variogram models are used during the simulation. Figure 64 shows variogram

modeling of sandstone facies. Figure 64a shows 5 m range and sill at 0.25 with zero nugget. The 5 m range indicates that our sandstone facies at each well can only be correlated up to 5 m and any pair which has more than 5 m distance is considered as uncorrelated. Figure 64b shows 5500 m range and sill at 0.24 with zero nugget. The 5500 m range indicates that the sandstone facies can only be correlated horizontally up to 5500 m and any pair which has more than 5500 m horizontal distance is considered as uncorrelated. Areal correlation shows a significant grouping in sandstone facies (figure 64c).

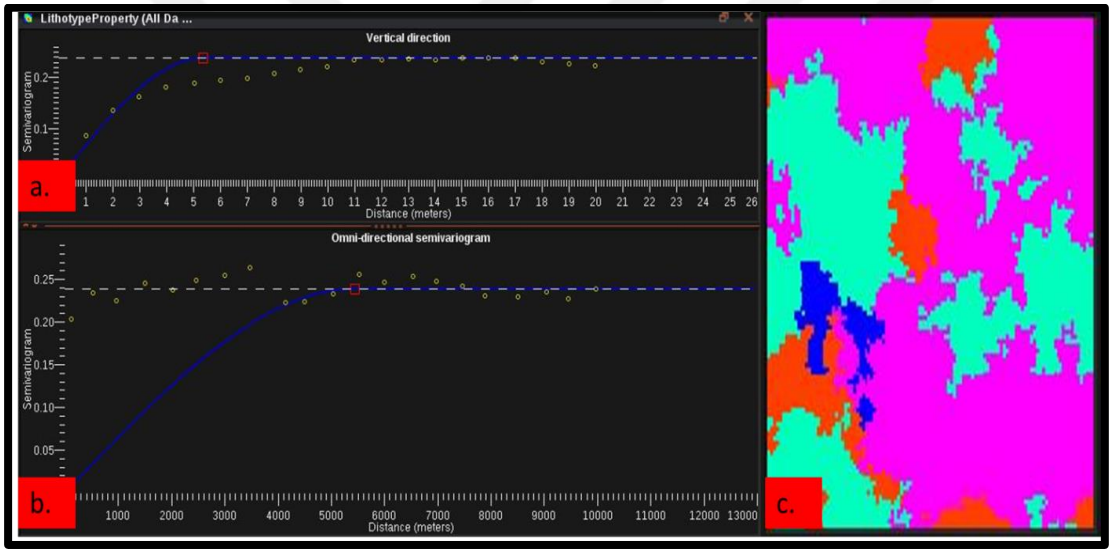


Figure 72 : a. Vertical variogram modeling of facies. It is an exponential model and red square shows the position of sill and range. Yellow circles are the log values in vertical direction and blue line is the vertical semi variogram model. b. Horizontal variogram modeling. It is an exponential model and red square shows the position of sill and range. Yellow circles are the log values in horizontal direction and blue line is the semi variogram model. c. Areal correlation of sandstone facies.

Figure 65 shows variogram modeling of sandstone porosities. Figure 65a shows 3 m range and sill at 0.8 with zero nugget. The 3 m range shows that the sandstone porosities in each well can only be correlated up to 3 m and any pair which

has more than 3 m distance is considered as uncorrelated. Figure 65b shows 4500 m range and sill at 0.8 with zero nugget. The 4500 m range indicates that the sandstone facies can only be correlated horizontally up to 4500 m and any pair which has more than 4500 m horizontal distance is considered as uncorrelated. Areal correlation shows a significant grouping in sandstone porosities (figure 65c).

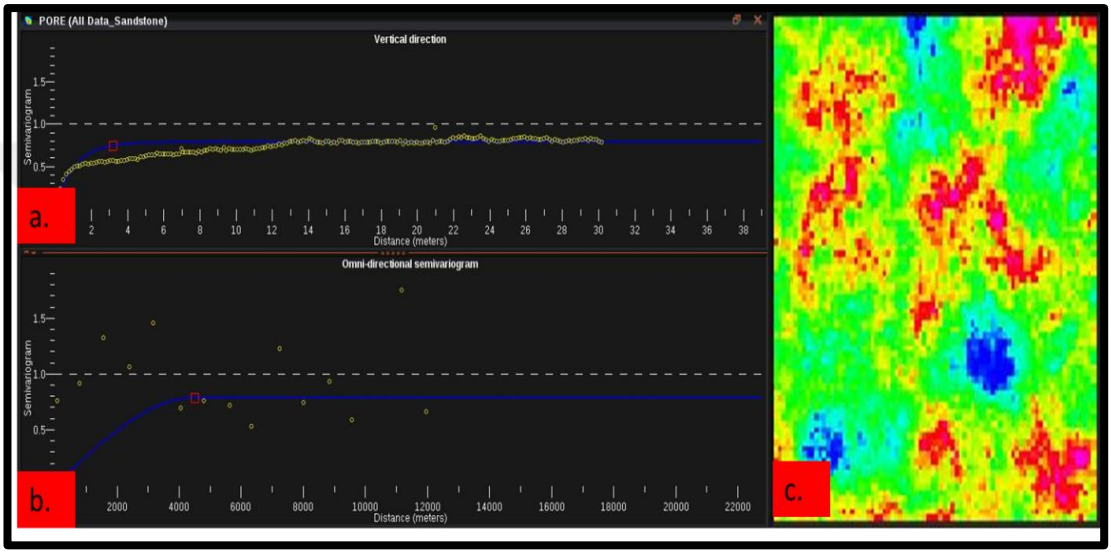


Figure 73 : Vertical variogram modeling of porosity. It is an exponential model and red square shows the position of sill and range. Yellow circles are the porosity values in vertical direction and blue line is the vertical semi variogram model. b. Horizontal variogram modeling of porosity. It is an exponential model and red square shows the position of sill and range. Yellow circles are the porosity values in horizontal direction and blue line is the semi variogram model. c. Areal correlation of sandstone porosities.

4.4.2 Facies Modeling

Sequential Indicator Simulation (SIS) is the main algorithm that has been used in this facies modeling study. There are three basic simulations, one of which is SIS with the background trend, other one is constrained with inversion products, and finally simulation updated with lithology proportion maps (figure 69). Background model uses facies logs and the only constraint is the skeleton of the model, which is the 3D grid. It is the distribution of defined facies along the interpreted surfaces with

sequential indicator algorithm. The basic idea behind running multiple simulations is if there is any correlation between the seismic inversion products, then it can be considered as a useful constraint during the simulation to compare them with the less constrained model. Same is true if any sedimentological model is positively correlated with the data as it is in lithology proportion map.

Defining seismic-related constraint is controlled by the cross-correlation between primary and secondary data. Probability plot for secondary data is another way of checking and choosing proper secondary data for simulation. Before SIS has been run with inversion constrains, several probability plots have been generated (figure 66) in order to see which one of the inversion products had more discrimination in facies. Figure 66a shows high lambda-rho values indicating either shale with 80% probability or shaly sand with 20 percent probability which is a good discriminant for such facies. On the other hand, lambda-rho values ranging from 15 to 35 are interpreted as sand facies with 60% probability. While low value of mu-rho gives 30 percent of sand probability, higher values represent 100 percent shale, which is clear discriminant in figure 66b. Figure 66c shows that at the lower and higher density values of high probability, there are two different shale trends in the reservoir. Again, figure 66c shows 60% probability of sands at around 2.15 g/cm3 and 2.36 g/cm3 which are interpreted as gas saturated and non-saturated sandstone reservoirs respectively. Figure 66d shows high Vp/Vs ratio representing 50% tuff facies. Low values of Vp/Vs ratio is dominated by shaly sand with 75% probability. Facies are simplified to the sand, shale and shaly sand in order to increase the sensitivity of the inversion products. As a result, increase in number of facies decrease discrimination sensitivity of the inversion products.

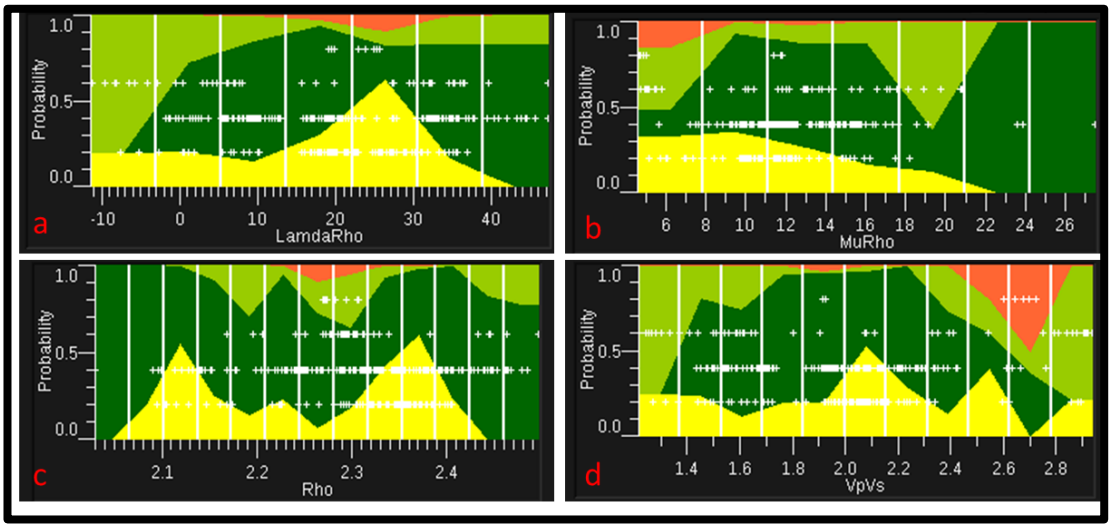


Figure 74 : Correlation of the secondary data which has been used at simulations. Yellow color represents sand facies, green color is shale, light green is shaly sand and orange is tuff. a. Probability of colored facies for a range of lambda-rho values at AA sand interval. b. Probability of colored facies for a range of mu-rho values at AA sand interval. c. Probability of colored facies for a range of Rho values at AA sand. d. Probability of colored facies for a range of Vp/Vs values at AA sand interval.

SIS updated with LPM requires special definition of lithology which is expected for the whole interval. The best way to have a lithology proportion map is to distribute known lithologies through seismic amplitude maps (Figure 67).

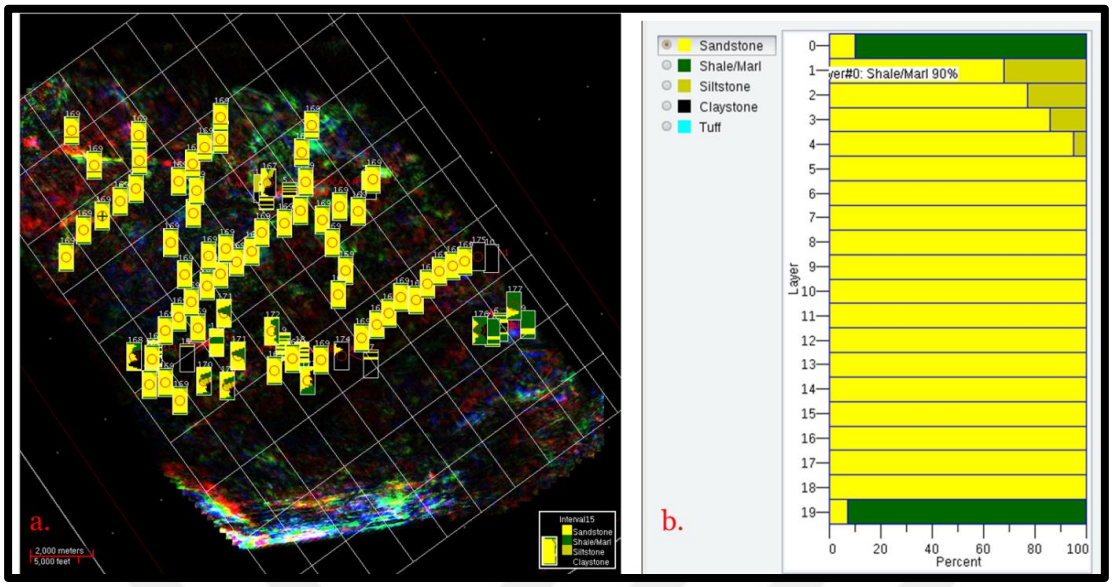


Figure 75 : a. Known channelized proportion curves are copied and distributed through the amplitude map which clearly indicates channel geometries and pre-define grid is in white. b. one of the proportion curve at well location.

Channelized system is seen on the amplitude map guiding the interpreter to set its lithology proportion curves spatially. If any of the wells tested channelized system at the proper location, then the interpreter simply follows the geometries seen on the amplitude map and sets the similar lithologies for predefined grid. Grid size is quite important. If it is chosen too small, then the whole process can suffer from the computation time. On the other hand, large grid size can cause the domination of the selected lithology curves for bigger area on the reservoir which might exaggerate the simulated results after lithology proportion map update.

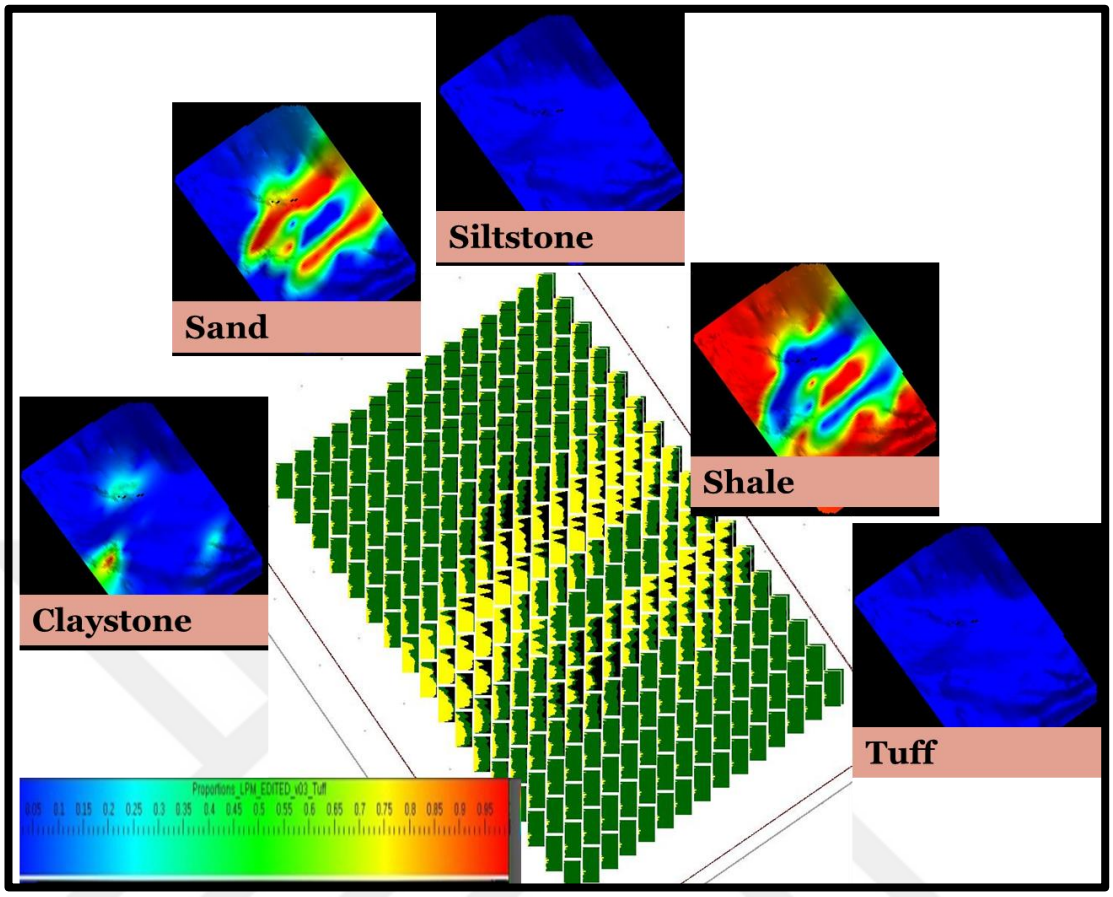


Figure 76 : Lithology proportion map (LPM) and related proportion maps for each facies color bar shows red for 100 percent and blue for none.

Figure 68 shows an example of lithology proportion map and related proportion maps for each facies. The LPM grid is defined as 15 blocks vs. 17 blocks. Each block is 600 m x 1200 m in size. It seems that the selected grid size is little bit larger than the channelized system that is seen in the amplitude maps. This will cause partial domination of the lithology that is seen on the lithology proportion curve. Since the channelized system is mostly sand dominated, LPM updated simulations exaggerates sand facies (Figure 69).

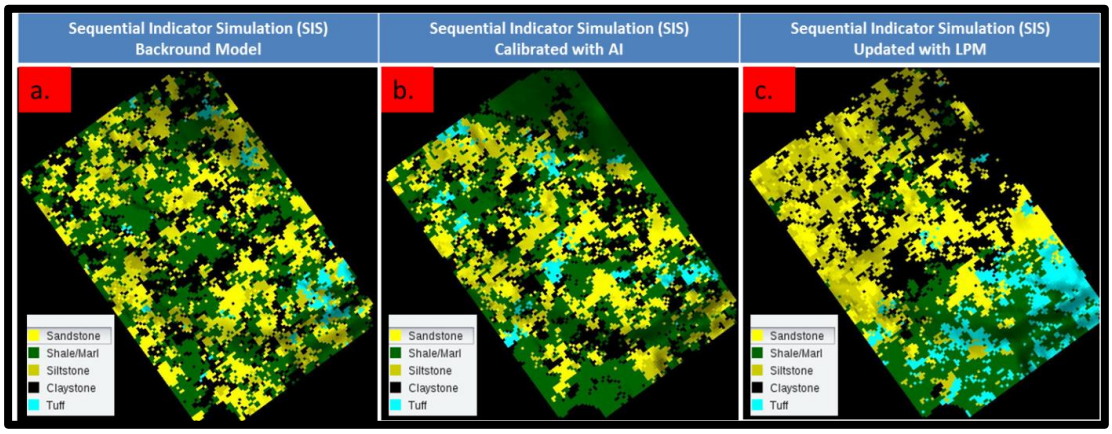


Figure 77 : a. Sequential indicator simulation background model at AA Sand, b. Sequential indicator simulation calibrated with acoustic impedance at AA Sand and c. Sequential indicator simulation updated with lithology proportion map at AA Sand.

Multi histogram plot for facies (figure 70) shows how accurately facies are simulated and what is the common occurrence of each facies at different simulations. Sand occurrence is at around %38 for the SIS calibrated with inversion which is the highest between any of the run simulation. Likewise, all of the simulations suggest over %50 occurrence for shale facies. SIS updated with LPM gives the highest shaly-sandstone facies with %20 occurrence. Rest of the simulations shows at around %10 occurrence for shaly-sandstone. All of the simulations consider existing of tuff facies under %5 within the reservoir.

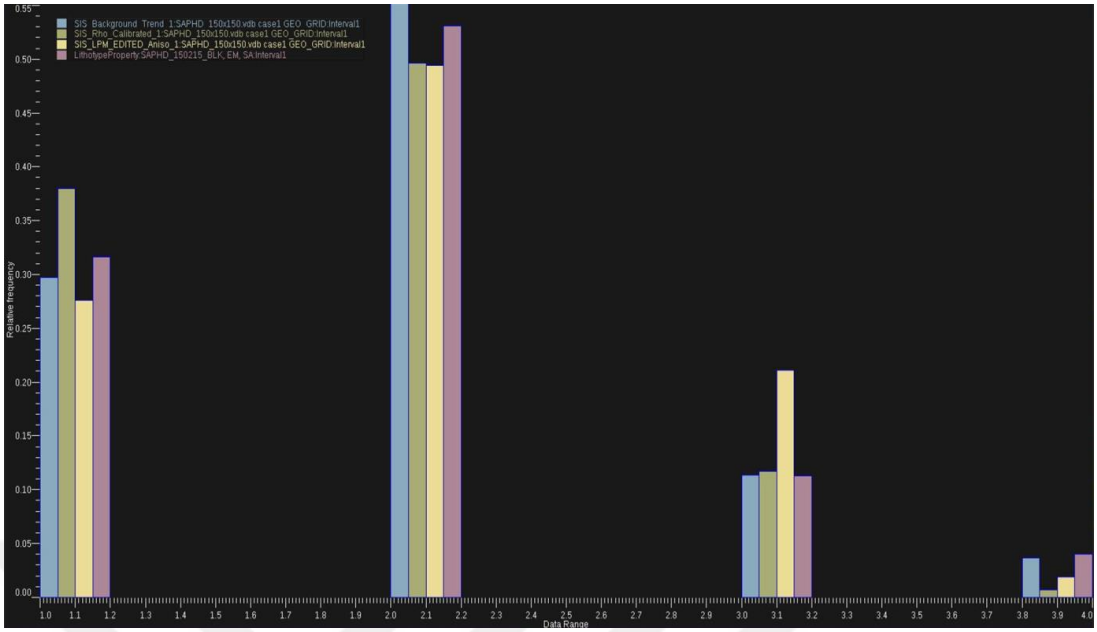


Figure 78 : Multi-histogram plot for facies. Blue for SIS background model, green for SIS calibrated with inversion, yellow for SIS updated with LPM and purple for input blocked lithotype log. Data range "1" is represents sandstone facies, "2" is shale, "3" is shaly sandstone, "4" is tuff.

4.4.3 Petrophysical Modeling

Sequential Gaussian Simulation (SGS) is the main algorithm that has been used for continuous variables like porosity, permeability etc. Simple krigging is the core of SGS. The mean of the property values, and its standard deviation at each grid node are estimated by simple krigging which means the variable at each grid node is represented as a random variable following a Gaussian distribution. However, SGS algorithm picks a random deviate from the normal distribution. In general, sequential methods use previously simulated values as data in the local conditional probability distribution (lcdp) in order to preserve the proper covariance structure between simulated values. Simulation starts with the normal score transform of the data in order to have a normal distribution, and it is followed by estimation of cumulative density function (cdf). Spatial continuity is controlled by variogram modeling of the data, and secondary data can be used to constrain the simulation. Correlation between the primary and the secondary data controls the strength of the relationship. In order to have comparable products, all petrophysical simulations have been constrained by facies which are

based on previously calculated three facies simulations (SIS Background Model, SIS Calibrated Model, SIS Updated with LPM). Several petrophysical properties have been simulated, one of which is porosity. Porosity values are the primary data which have been simulated by SGS constrained with background facies model (Figure 71a), constrained by impedance facies model (Figure 71b), and constrained by LPM updated facies model (Figure 71c).

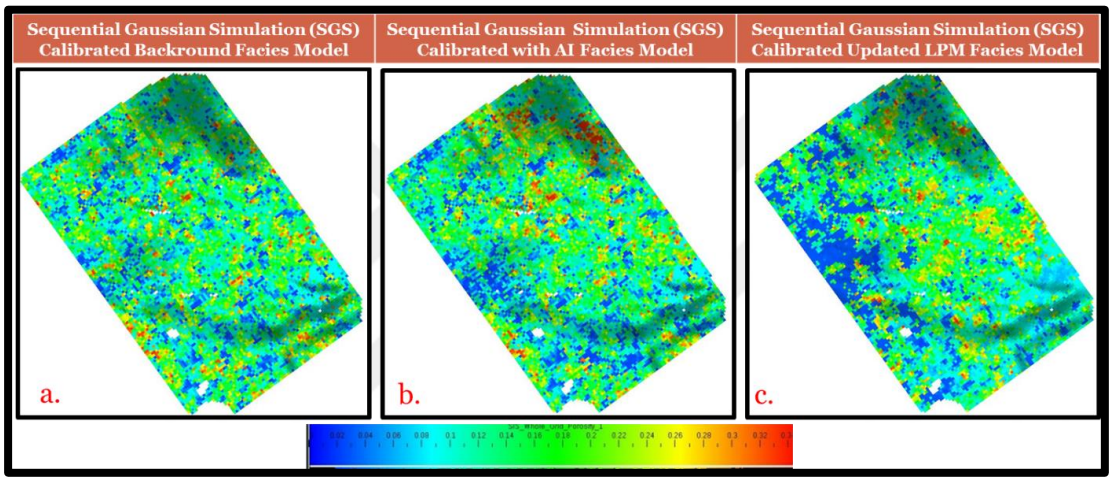


Figure 79 : a. Sequential Gaussian Simulation (SGS) porosity model calibrated background facies model at AA Sand, b. SGS porosity model calibrated with impedance facies model at AA Sand and c. SGS porosity model calibrated updated with lithology proportion map facies model at AA Sand.

Simulation results are analyzed in different forms one of which is cross-plotting the reservoir properties at a reservoir interval in order to see the correlation. Figure 72 shows porosity vs. permeability cross-plot which is produced by petrophysical simulation results. Facies are color-coded and yellow color indicates sandstone facies which shows a distinctive porosity-permeability trend for the reservoir interval.

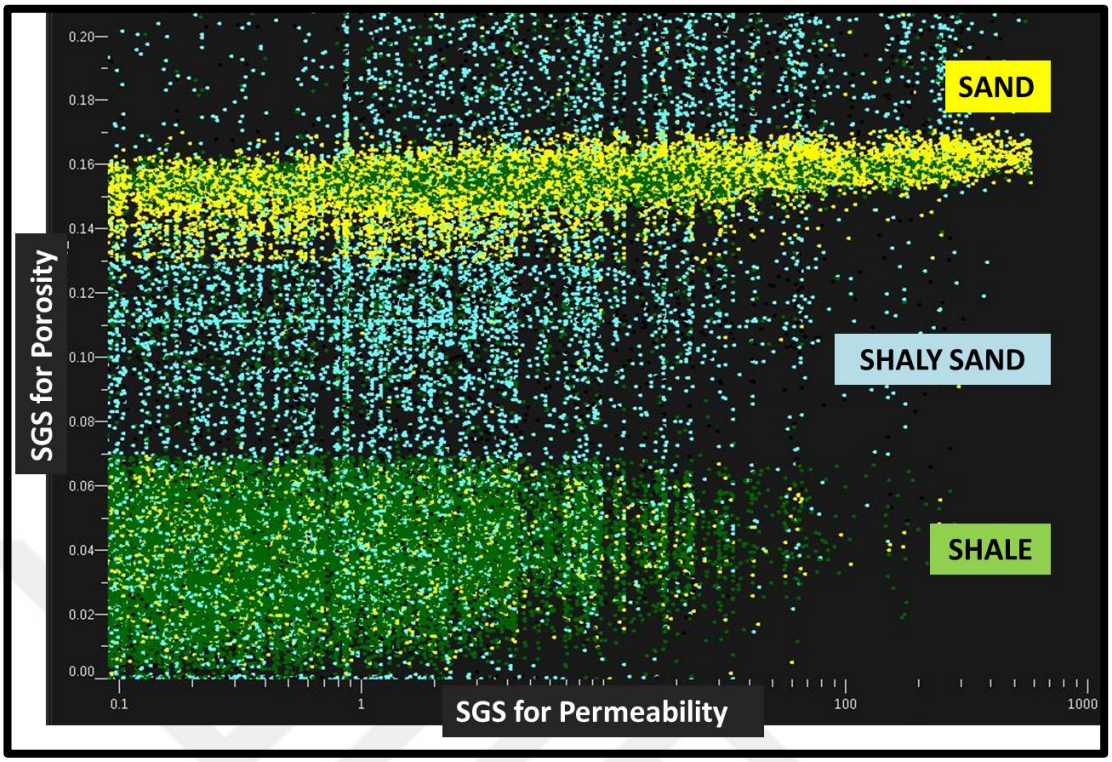


Figure 80 : Cross-plot of reservoir property simulation results (Porosity vs. Permeability). Samples are color-coded to facies and for the simplicity; it is divided into three facies type. Sandstone is in yellow, shale in green and shaly sand in cyan.

Without applying complicated simulation algorithm to the data, correlated well log interpolation is the way of distributing reservoir-related information such as lithology, permeability and density which are shown in figure 73a, 73c, and 73e, respectively. Figure 73b shows SIS of facies calibrated with impedance. Figure 73d shows SGS of permeability calibrated with impedance. Figure 73f shows SGS of density calibrated with impedance. In order to compare previous interpretation and simulation results, a line of section has been generated with the projected wells. Figure 73g shows the location of the line of section and projected wells along the line.

Results show the continuity of the facies. Especially faults and facies relations are represented very well. It is already known that faults are the results of post depositional deformation. Moreover, reservoir is interpreted as thin, highly permeable multiple layers within a thick low permeability zone. However, simulation result

shows that the upper part of the reservoir is highly permeable, and as it gets into the deeper part, permeability gets lower and lower proportionally. Figure 73f shows the simulation result of the density for the reservoir interval. It shows that low density values are restricted to the upper part of the reservoir and as soon as the burial depth of the reservoir increases, density values also increase which is pretty consistent with the well log analysis which has been done earlier.

One way of checking simulation results is outputting them as a set of logs at the blind well location, which is preserved and not included to the simulation process. In this way, how successfully the required information is estimated can be determined without any information from the selected well location. This determination is called *blind test* for a selected well location. Facies results run by several SIS show how accurately the selected information is simulated away from the known location (figure 74).

Lithology curves for the pre-defined blind test well have been plotted for each simulation at figure 74. Observed lithology from cuttings and log interpretation are compared to simulated lithology from SIS background trend, SIS calibrated with seismic pre-stack inversion (Rho), SIS calibrated with seismic pre-stack inversion (Vp/Vs), SIS calibrated with seismic pre-stack inversion (mu-rho) and SIS updated with LPM. Location of the blind test well is Field 4 which is the only existing well in that location (figure 28). Results show that without any well data involved into the simulation for the blind test location, lithologies are well presented at the simulation.

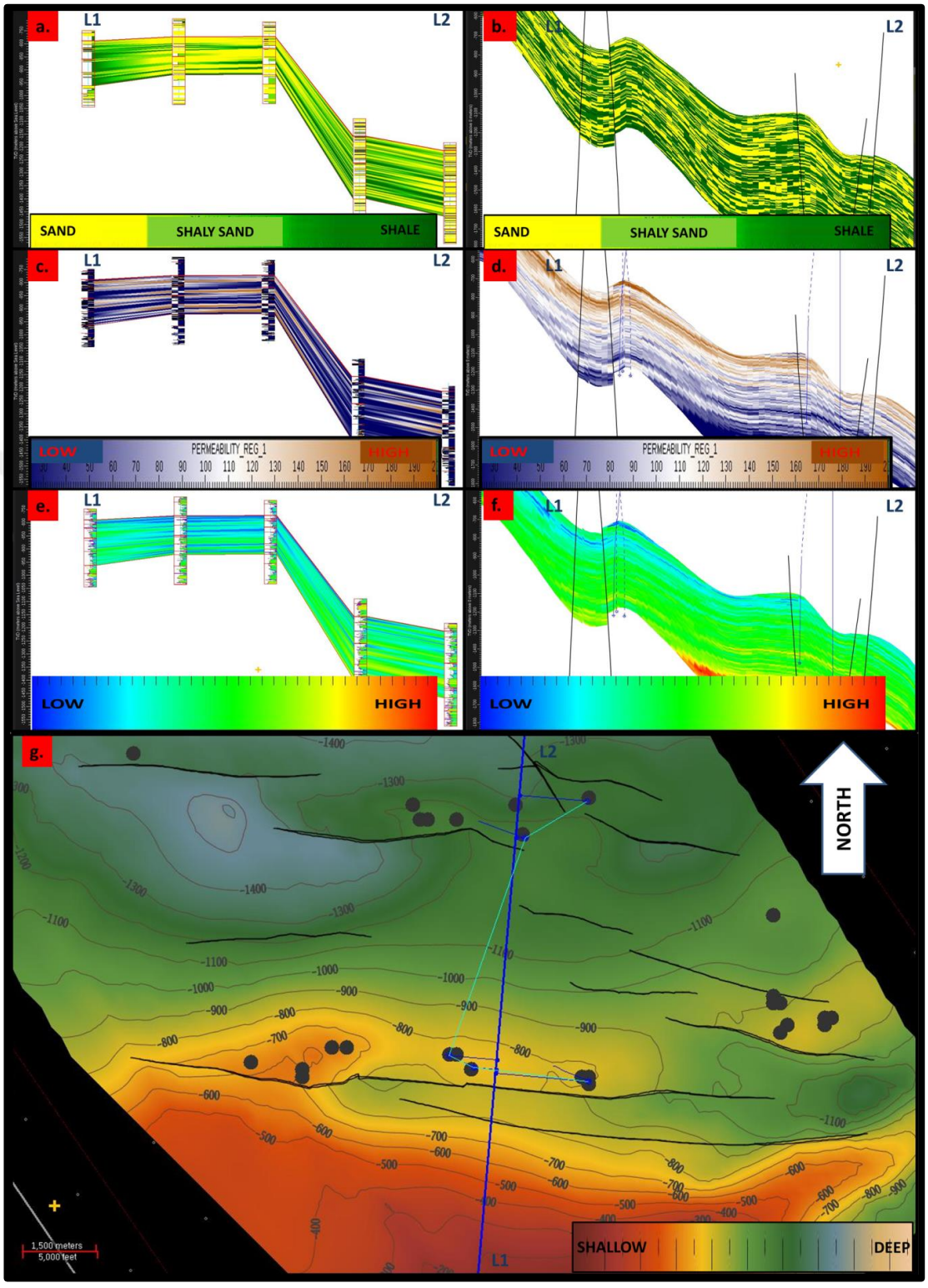


Figure 81 : Well log correlation vs. simulation results a. Facies log correlation b. SIS facies model calibrated with impedance c. Permeability log correlation. d. SGS permeability model calibrated with impedance e. Density log correlation. f. SGS density model calibrated with impedance. g. Basemap of top reservoir. Blue line indicates the line of section and the position of projected wells.

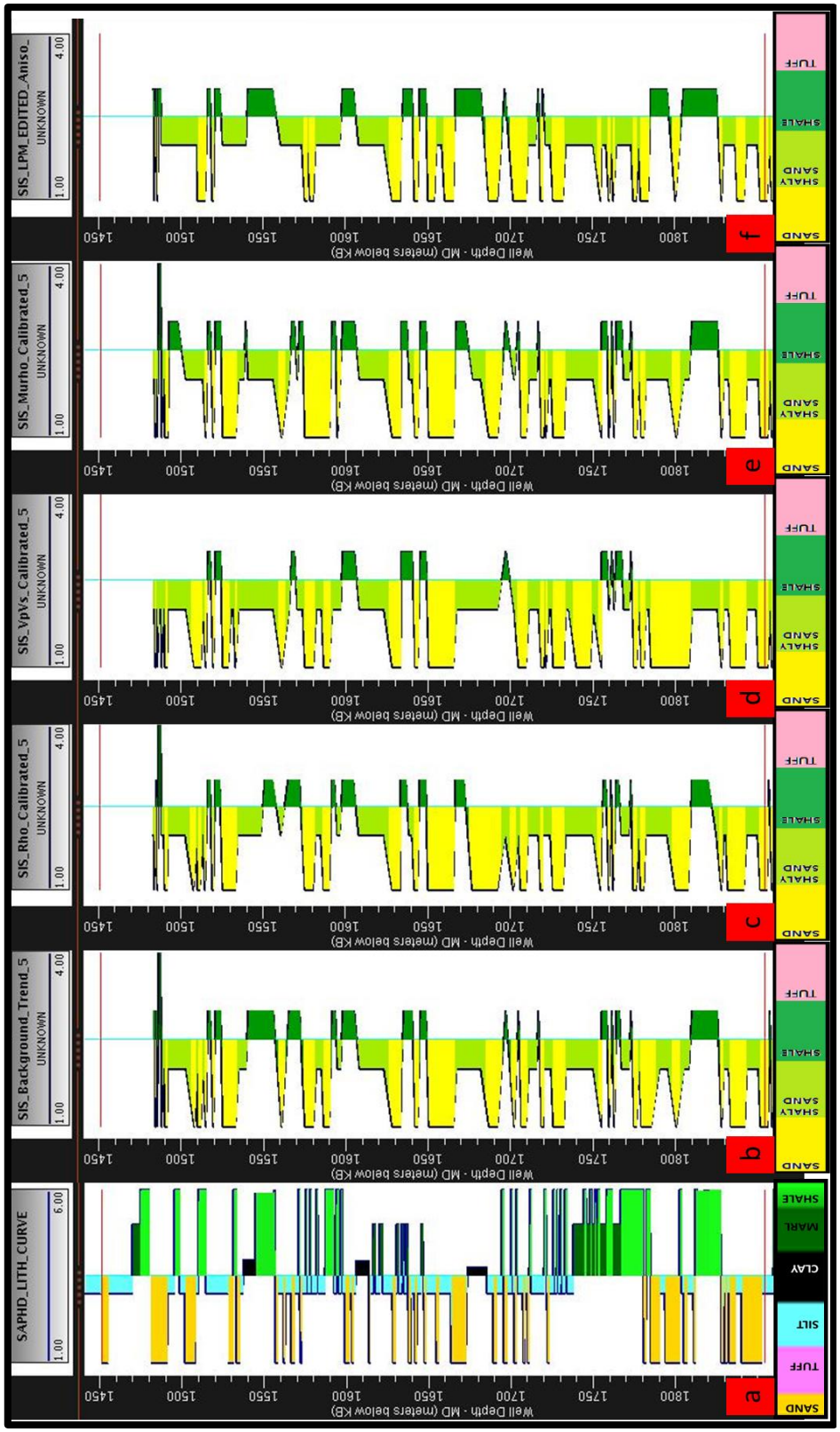


Figure 82 : Lithology curves for pre-defined blind test well. a. Observed lithology from cuttings and log interpretation b. Simulated lithology from SIS background trend c. SIS calibrated with seismic pre-stack inversion (Rho) d. SIS calibrated with seismic pre-stack inversion (Vp/Vs) e. SIS calibrated with seismic pre-stack inversion (MuRho) f. SIS updated with LPM. Location of the blind test well is at Field 4. It is a single well in that location (figure 27).

In summary, data conditioning is the important part of the process and after completing proper cleaning on the data, simulations have been run on the selected subset of the data. There are several simulation algorithms which are tested on the data set. Input data is divided into two groups one of which is categorical data, such as facies, and second one is continuous data, such as porosity, density etc. Simulation algorithm has been selected by whether the data type was categorical or continuous. Sequential Indicator Simulation (SIS) algorithm has been used for facies simulation, and Sequential Gaussian Simulation (SGS) algorithm has been used for reservoir properties. Simulations have been constrained by two types of secondary data. One is any selected product of inversion results and other one is lithology proportion map. Spatial distribution of simulation results has been modeled by pre-defined variogram models. Both vertical and omnidirectional variogram models have been supplied to the simulation algorithms.

Facies simulation has been done with three types of SIS simulation on the 3D grid. Basically, the same simulation algorithm has been applied to the data and only difference is the secondary data which gets into the process. These three simulations can be summarized as without secondary data, with secondary data which is based on seismic inversion results and with secondary data scaled by lithology proportion map (LPM). LPM updated SIS simulation is aggressively diverging from the other two simulation results which increase the uncertainty of the facies definition for this simulation. It is concluded that the large grid size of the LPM is responsible from this uncertainty.

Reservoir simulations have been successfully applied to the data set. There is not a large outlier at the well locations which might be an indicator of excessive level of uncertainty for simulations. Simulation results are pretty satisfactory and can be used for further studies such as detail volumetric calculations and dynamic fluid simulation.

CHAPTER 5

CONCLUSIONS AND DISCUSSION

Geologic structures, stratigraphy and reservoir architecture from seismic have been identified in detail via mapping the geometrical expression of seismic reflectors in travel time and space. Results of the conventional interpretation within this study reveal several vital points which may highlight final conclusions of this study in geological perspective. Findings can be listed as;

- Post-rift Eocene compression and its timing are the main components which shape the Akçakoca reservoirs.
- Timing of the compressional deformation differs depending upon the depositional environment. At the south margin of the Akçakoca basin where the gas production field located, the Akçakoca member of Kusuri Formation has already been deposited when the deformation occurred whose supporting evidence can be seen in isopachous, concordant reflection geometries and amplitude maps. Specifically, amplitude maps of Akçakoca reservoirs show highly sinusoidal, NE-SW oriented channel geometries which are the main indication of the low energy turbidite channel. These geometries are not disrupted by E-W oriented compressional deformation related faulting proving that the timing of compressional deformation can only be right after the deposition of the Akçakoca member. However, at the more distal part of the Akçakoca basin which can only be interpreted by 2D seismic lines, the 2D seismic interpretation reveals that even Oligocene shows some supporting evidence of which compressional deformation formed after Early Oligocene started to deposition.
- 2D/3D seismic interpretation results show that Oligocene reflections pinch-out to the southern margin of the Black Sea before they reach to the 3D survey area (Figure 5 and 75). Obviously, there are no Oligocene deposits

within the Akçakoca 3D survey area which is also supported by drilled wells as well.

- 2D seismic reflection geometries of Erikli member of Akveren Formation show undulating geometries due to compressional deformation. Erikli member has been interpreted as a displacement surface between underlying Yemişliçay volkanics and overlying Akveren limestones (Figure 5 and 75).
- Foreland propagated displacement generates a series of foretrusts which are getting younger (as young as Early Oligocene) towards the basin (Figure 5 and 75).
- Yemişliçay has been interpreted as foreland dipping backstop that is unconformably overlain by the basin infill (Figure 5 and 75).
- Regional 2D seismic lines carry valuable information which suggests a NW-SE elongated strike slip fault (Figure 5 and 75) along with southern margin uplift.
- Qualitatively, the amount of uplift at eastern block is considerably higher than the uplift that is seen at western block of the strike slip fault plane.
- Akçakoca basin is considered as an inverted half graben which was initiated during the Middle Baremian rifting and inverted by Late Eocene compressional deformation.
- Even though the Akçakoca reservoir is considered to be a biogenic gas reservoir, south-vergent thrust fault-related thermogenic gas charge from the basin is theoretically possible.
- Seismic interpretation and well data analysis suggest that Akçakoca member is deep water turbite system and its reservoir levels consist of sand rich channels, sand dominated point bars, and lobes with sheet sands. Shaly intervals of Kusuri Formation constitute the seal rocks in Akçakoca Field. Main reservoir levels are sand-filled, high to moderate sinusoidal submarine channels which are capped by either shaly floodplain deposits or shale dominated levees of the system.
- Akçakoca reservoirs show meandering geometries which contain laterally and vertically stacked sand-rich point bar deposits. In some places, these point bars are sealed by clay plugs as well.

- 3D seismic interpretation results show that trap mechanism of Akçakoca reservoirs is mainly structural and controlled by south-vergent thrust fault.
- Figure 17a and 17b show depth and time structure maps of Sürmeli member, respectively which indicate that major deformation is in east-west direction. Also Figure 17h shows the south-vergent thrust faults are significant and basically this deformation gives the final shape to the reservoirs.
- The most of the Sürmeli member at the southern boundary of the survey area is deformed and eroded due to uplifting of Late Eocene compression. Time to time, this erosional deformation can be so deep that it reaches down to top of Akçakoca reservoirs.
- Folding at the hanging wall of the thrust faults is in maximum when the fault plane is close to the shoreline. Maximum folding is related to the shortening, and it shows the maximum increase of thickness at the southern boundary. Thickness of bottom reservoirs of Akçakoca between the fault planes is almost constant in the east-west direction which may imply the sediment fairway is in southwest-northeast direction. Supporting evidence can be seen at amplitude maps of bottom reservoirs of Akçakoca. However, amplitude maps of top of Akçakoca reservoirs suggest that the sediment fairway is in east-west direction which is parallel to the fault planes.
- Spectrally decomposed amplitude maps at different frequency bands (Figure 25) indicate the facies distribution along the geometries that have been identified on the seismic might vary and can be detected in great detail.
- Sinusoidal, subaqueous, channel geometries within the bottom part of the Akçakoca reservoirs (figure 26e and 26f) are interpreted as having low to moderate energy and deposited proximal to the southern shoreline. However, at further stages the channelized geometries (figure 26c and 26d) laterally migrate to the north due to uplifting of the southern margin of the basin. Deformation rate is interpreted to have been controlling the sediment influx at this stage. At the bottom part of the Akçakoca reservoirs, sinusoidal channel geometries do not change their orientation or shape

while crossing the east-west oriented faults. This may imply that faults are postdated by Eocene aged turbidite channels.

- Moreover, at the last stage (figure 26a and 26b), there is not distinctive and steady channel geometry at the southern margin. During this period, within top part of the Akçakoca reservoirs, sediment input is clearly in east to west direction which shows that faults are recently generated and started to lead sediments through the basin. This sudden change in sediment direction is due to a higher rate of uplift of the southern margin.
- Sand box model of the Gomes et al., 2010 suggests that basinward propagated thrust can also generate back-thrusts which have similar faulting patterns that are seen at Akçakoca field (Figure 75). This similarity has been interpreted as a supporting evidence of the conceptual faulting model interpretation at Akçakoca field.

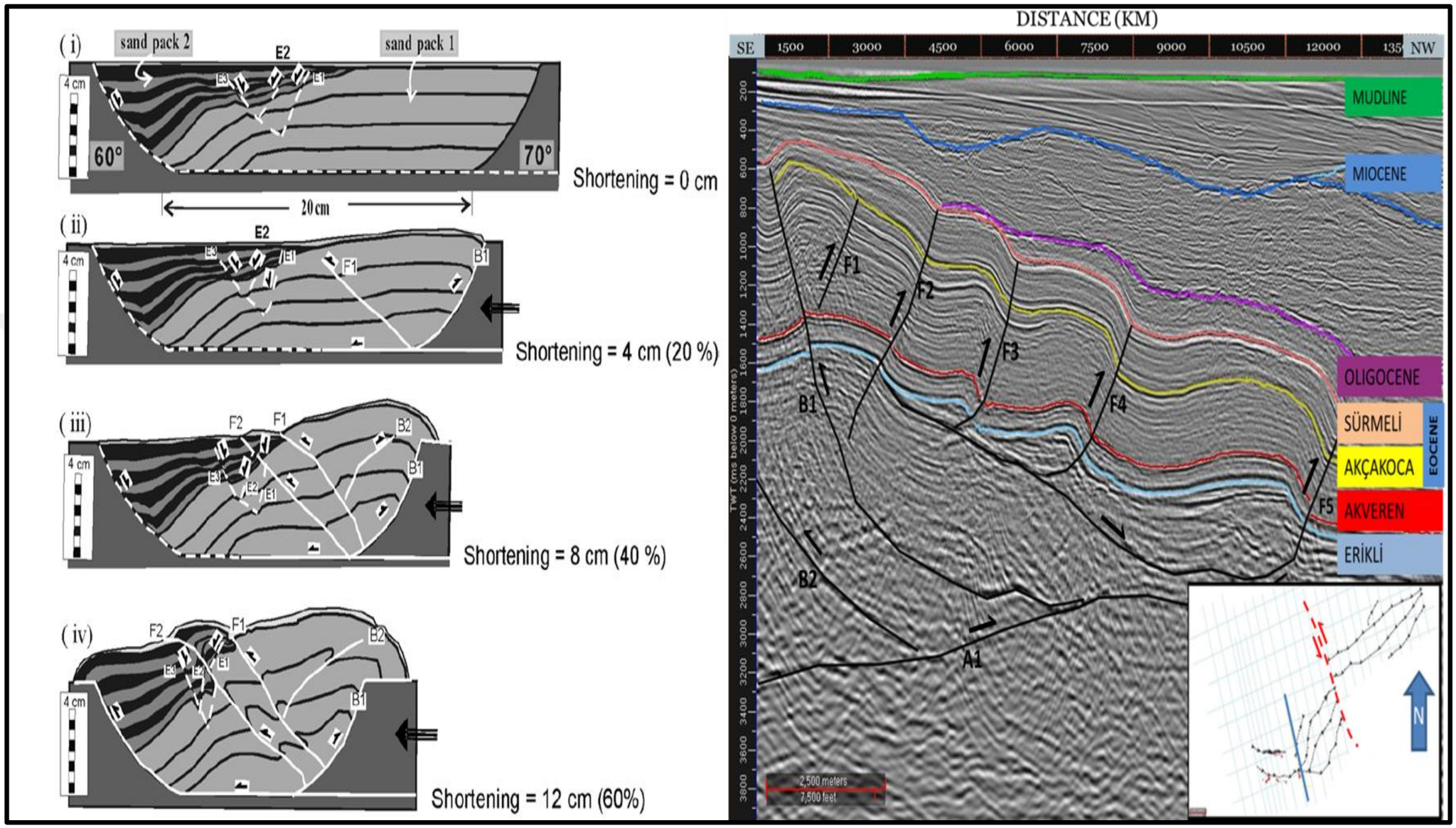


Figure 84: Left is the (i-iv) sequential line drawings of inversion steps which were taken through the transparent sidewalls of sand box model generated by (Gomes et al., 2010). E1-E3 are structures formed during extensional steps; F1 and F2 are forethrusts, and B1 and B2, backthrusts. Dashed and continuous lines represent extensional and contractional structures, respectively. Right is an Akçakoca field 2D seismic section in time perpendicular to the shoreline with interpretation and its base map (time slice at 2100 ms). Black lines show the interpreted thrust faults and associated antithetic faults. Green horizon is water bottom. Blue horizon is top of Miocene. Purple horizon is top of Oligocene. Orange horizon is top of Sürmeli member of Kusuri Formation, yellow horizon is top of Akçakoca member of Kusuri Formation, red horizon is top of Akveren Formation and light blue horizon is top of Erikli member of Akveren Formation. Reflection geometries of the Erikli look undulating due to compressional deformation. Undulation intensifies and thickens towards the basin. These are interpreted as a series of thrust faulting with a basinward increasing throw amount. Results of the sand box model of Gomes et al., 2010 (specifically, 40% shortening case iii) and the 2D interpretation at Akçakoca are conformable and support each other. Faults within Akçakoca are named as F1, F2, F3, F4, and F5 for the trust faults which are at the same direction with the compressional forces. Back-trust faults are named B1 and B2. Finally, A1 is low angle compressional deformation related trust fault. Red dash line on the base map indicates the major strike slip fault.

Further effort has been done for understanding the seismic amplitude, magnitude of amplitude and its variations along the reflection surface by quantifying seismic interpretations. Post-stack amplitude analysis, offset-dependent amplitude analysis, impedance inversion (pre-stack, post-stack), and forward seismic modeling results reveal that it is possible to validate existence of hydrocarbons. Extra information has been gained and used during reservoir characterization such as density porosity or porosity permeability trend within reservoir intervals. Moreover, distributing any lithological or petrophysical property along the 3D survey area was possible by these quantitative methods. Followings are the results;

- The rock physics analysis in the study area show that the most of the data obeys the empirical boundaries. Outliers are edited and not included to the study.
- The fluid substitution results helped to recognize gas saturated reservoirs. Water saturated sand and shale trend is close to the Castagna's mud rock line.
- AVO practice in the study area has revealed how clearly the gas saturated reservoir levels were correlated with the class III AVO.
- The Akçakoca reservoir sands are accounted as soft sands which capped by shale facies.
- Moreover, AVO has helped to downgrade prospective locations, which did not show any clear AVO response. Distributing fluid related trends from the AVO results have been possible along the 3D survey area but final conclusion in this matter is that there might be several other trends, which give similar amplitude response that are observed in the data.
- Both post-stack and pre-stack inversions are the results which are vertically constrained by top of AA sand to bottom of F sand. These have been interpreted as the top and bottom of the multi-reservoir packages. Initial models of P impedance, S impedance and density have been used to constraint the inversion results.
- Inversion results indicate that pre-stack inversion is superior to the post-stack inversion and geologically reliable as well. Furthermore, pre-stack inversion has more frequency content. However, each inversion products

are in seismic scale instead of well scale, and these inversion products are unable to delineate sub-seismic events such as this bedded gas saturated sand or small scale changes at density.

Contrasts in elastic properties for an interface are the source of seismic amplitude which help interpreter to understand lithology, porosity, pore-fluid type and saturation behavior spatially. Integration of conventional interpretation, the quantitative methods and statistical simulation methods give the spatial probability maps of reservoir fluids, facies and also stochastic realization of the reservoir properties. Well logs which are considered as point sources cannot provide a spatial information about the reservoirs. 3D seismic can help to compensate this lack of spatial information within the reservoir. However, resolution is the major limitation of the seismic data. Sub-seismic events need better estimation techniques. Variogram modeling based kriging or simulations provide well log scale information. The obtained results of goestatistical reservoir characterization within the study area can be listed as;

- Simulation algorithms have been selected by whether the data type was categorical (facies) or continuous (porosity or permeability). Sequential Indicator Simulation (SIS) algorithm has been run for facies simulation, and Sequential Gaussian Simulation (SGS) algorithm has been run for reservoir properties which are considered one of the ultimate products in this study.
- Permeability estimation took place and determined the best possible relation between the four different sources of porosity and permeability relations.
- Simulations have been constrained by secondary data which were either inversion results or lithology proportion maps. Best results are obtained by simulations which are constrained by inversion results.
- Lambda represents the incompressibility. High lambda-rho values imply highly incompressible fluid such as water. Relatively high lambda-rho values ranging from 15 to 35 are interpreted as water saturated sand facies with 60% probability. On the other hand, high end values of lambda-rho

suggest shale with 80% probability which is a good discriminant for such facies.

- Mu represents the rigidity. Low value of mu-rho gives 30 percent of sand probability, and higher values represent 100 percent shale, which is clear discriminant for shale. Moreover this observation is conformable with the soft sand approach.
- Figure 66c shows that the lower and higher density values with the high probability which may imply there are two different shale trends in the reservoir.
- Again, figure 66c shows 60% probability of sands at around 2.15 g/cm3 and 2.36 g/cm3 which are interpreted as gas saturated and water saturated sandstone reservoirs respectively.
- Figure 66d shows high Vp/Vs ratio representing 50% tuff facies. Low values of Vp/Vs ratio is dominated by shaly sand with 75% probability.
- Facies are simplified to the sand, shale and shaly sand in order to increase the sensitivity of the inversion products. Increase in number of facies decrease discrimination sensitivity of the inversion products.
- Simulation results show the continuity of the facies. Especially faults and facies relations are represented very well. It is already known that faults are the results of post depositional deformation. Moreover, reservoir is interpreted as thin, highly permeable multiple layers within a thick low permeability zone. However, simulation result shows that the upper part of the reservoir is highly permeable, and as it gets into the deeper part, permeability gets lower and lower proportionally.
- Figure 73f shows the simulation result of the density for the reservoir interval. It reveals that low density values are restricted to the upper part of the reservoir and as soon as the burial depth of the reservoir increases, density values also increase which is pretty consistent with the well log analysis which has been done earlier in this study.
- Spatial distribution of each simulation has been modeled by using variogram models. Both vertical and omnidirectional variogram models have been supplied to the simulation algorithms. Sandstone facies

vertically correlated up to 5 meters and laterally correlated more than 5km. Porosity values can only be correlated vertically at 3 meters and laterally at 4km.

Geostatistical modeling of reservoirs helps to delineate spatially correlated and stochastically constrained gas bearing sandstone facies from surroundings. Simulation results have been checked by blind test analysis, which has revealed that the data set was successfully modeled with several simulation algorithms, and all the available geological and geophysical data sets have been integrated into these models.

Detailed seismic reservoir characterization constrained by well log rock physics, AVO and impedance inversion have been conducted and applied to Akçakoca 3D within the Akçakoca Field. The most likely distribution of facies and petrophysical properties have been mapped in a deep water turbidite system at Akçakoca 3D.

These maps are ultimate products in the process of geologically characterizing reservoirs from seismic data. Products can be used as inputs for various decision and risk analyses during exploration and development or as constraints for reservoir modeling and fluid flow simulation during production and reservoir forecasting.

Characterization of the Akçakoca 3D gas field has been done successfully but limitation of the applied methodologies has to be underlined as well. One big limitation is all the facies have been defined by composite log which is based on cuttings and e-log responses. The composite log itself may contain facies definition error. This may cause mismatch between defined facies and the log responses. Thin bed effect is another limitation that is observed during the study. Definition of claystone and siltstone is pretty similar except the color. *''Claystones are defined as white, light grey colored soft-hardy, soft carbonaceous. Siltstones are described as light grey, off-white colored soft carbonaceous, claystone interbedded.''* This suggests that seismic contrast between claystone and siltstone is weak. The interbedded sand and shale sequences in the studied turbidite system consist of thin bedded sands which also have weak contrasts in seismic properties compared with the intercalating shales. From the log interpretation, the thin bedded sand with limited clay content and thin bedded shale with limited silt content have been interpreted as sand and shale mixture which has similar elastic properties. Therefore, tuning effect is ignored during the study. Tuning

can lead to a severe error at parameter estimation. Furthermore, the classification and prediction of facies can directly be affected by tuning as well.

Another source of error is a linear approximation of the Zeoppritz equations which has been based for inversion algorithms. This linear approximation is only true for angles of incidence up to approximately 30 degree (Shuey 1985). Angles of incidence for the studied reservoir level do not exceed this range (Figure 44). Therefore, inversion errors in this application will be limited.

Furthermore, the way of processing 3D seismic affects AVO and inversion products directly. Available seismic data set and its processing flows (Figure 2 and 3) is assumed to be a true amplitude processing.

Conventional interpretation brings certain amount of error as well. Specifically, horizon interpretation for each reservoir level contains an uncertainty. Starting from the amplitude extraction to AVO and inversion products can be affected by the incorrect picking of the reservoirs. On the other hand, all the pickings have been checked by the well data. High consistency between picking surfaces and well data are observed during the study.

Statistic of the entire reservoir may not be represented by the well log data that we used in this study. Vertically stack facies are used to generate laterally extending facies prediction maps. Likewise, facies that have not been observed in the wells may exist in any part of the untested reservoir. Moreover, it is important to note that reservoir sands are accounted as soft sands which capped by shale facies. This assumption may not be true everywhere. However, the well log observation shows that almost all of the reservoirs are overlain by shaly facies which has higher density values than sand facies.

Source of petrophysical properties are mainly calculated logs which include certain amounts of error as well. Petrophysical log calculations and corrections are checked and observed within an acceptable error range.

SIS and SGS Simulation algorithms have been run in this study but there are other simulation algorithms such as Plurry Gaussian Simulation (PGS) and Truncated Gaussian Simulation (TGS) which may give and additional information about the reservoirs. However, Akçakoca 3D is at around 223 km^2 and the survey area represents only the small part of the system which means by using amplitude in order to define

complicated relations between facies might cause other problems and bring more uncertainties into the reservoir characterization.

With all these potential limitations and uncertainties that have been considered in this case study, uncertainties relating to variability in facies and petrophysical properties strengthen the validity of the seismic reservoir characterization of the Akçakoca Production Field.

The blind testing of the well located at field-4 represents a means of validating applied methodology. The match between predicted facies and well log observations is not perfect, but that is not initially expected. Well logs are considered as one dimensional point source, however seismic data contain information from a relatively large area that is why blind test location is defined within a relatively remote area. As a result, blind test simulation results indicate that the facies simulations are reliable but not unique.

REFERENCES

Aki, K., and Richards, P. G., 1980, Quantitative seismology: Theory and methods: W. H. Freeman and Co.

Avseth, P., Mukerji, T., and Mavko, G., 2005, Quantitative seismic interpretation, applying rock physics to reduce interpretation risk: Cambridge University Press.

Belousov, V. V., and Volvovsky, B. S., 1988, Structure and evolution of the Earth's crust and upper mantle of the Black Sea: Bollettino di Geofisica Teorica ed Applicata, v. 30, no. 117–118, p. 109–196.

Bouma, A. H., 1962, Sedimentology of Some Flysch Deposits: A Graphic Approach to Facies Interpretation. Elsevier, Amsterdam, 168 pp.

Brown, L. F., and Fisher, W. L., 1980, Seismic stratigraphic interpretation and petroleum exploration. American Association of Petroleum Geologists continuing education course note series. no: 16.

Castagna, J. P., and Backus, M. M., 1993, Offset dependent reflectivity—Theory and practice of AVO analysis, Soc. Expl. Geophys.

Castagna, J. P., Batzle, M. L., and Eastwood, R. L., 1985, Relationships between compressional wave and shear wave velocities in clastic silicate rocks: Geophysics, 50, 571–581.

Castagna, J. P., Batzle, M. L., and Kan, T. K., 1993, Rock physics—The link between rock properties and AVO response, in Castagna, J. P., and Backus,M. M., Eds.,

Offset-dependent reflectivity—Theory and practice of AVO analysis: Soc. Expl. Geophys., 135–171.

Dagbert, M. and Dimitrkopoulos, R., 1992, Sequential modelling of relative indicator variables: dealing with multiple lithology types. Geostatistics Troia .92, Soares, A. Editor.

DecisionSpace Geosciences 10, Halliburton Landmark software, 2015, available at https:/www.landmarksoftware.com/Pages/DecisionSpaceGeosciences10.aspx

Deutsch, C. V., 1996, Hierarchical Object Based Stochastic Modeling of Fluvial Reservoirs. Mathematical Geology, v.28, no.7, 857-880 pp.

Deutsch, C. V., and Journel, A. G., 1998, GSLIB Geostatistical Software Library and User's Guide. Oxford University Press, New York, 338 pp.

Doyen, P. M., 1988, Porosity from seismic data: A geostatistical approach: Geophysics, 53, pp 1263-1275.

Fatti, J. L., Vail, P. J., Smith, G. C., Strauss, P. J., and Levitt, P. R., 1994, Detection of gas in sandstone reservoirs using AVO analysis: A 3-D seismic case history using the geostack technique: Geophysics, 59, 1362-1376.

Feng, H., Russell, B. H., Bancroft, J. C., 2007, A comparison of hydrocarbon indicators derived from AVO analysis. CREWES Research Report — Volume 19 (2007).

Finetti, I., Bricchi, G., Del Ben, A., Pipan, M., and Xuan, Z., 1988, Geophysical study of the Black Sea: Bollettino di Geofisica Teorica ed Applicata, v. 30, p. 197–324.

Foster, D. J., Keys, R. G., and Lane, F. D., 2010, Interpretation of AVO anomalies, Geophysics, vol. 75, no. 5 SEPTEMBER-OCTOBER 2010 ; P. 75A3–75A13, 16 FIGS. 10.1190/1.3467825

Gassmann, F., 1951, Uber die elastizitat poroser medien: Verteljahrsschrift der Naturforschenden Gesellschaft in Zurich, 96, 1–23.

Gidlow, P. M., Smith, G. C., and Vail, P. J., 1992, Hydrocarbon detection using fluid factor traces: A case history: how useful is AVO analysis?: Joint Summer Research Workshop, SEG/EAGE, Expanded Abstracts, 78-89.

Gomez-Hernandez, J. and Srivastava, R.M., 1990, ISIM3D: an ANSI-C three dimensional multiple indicator conditional simulation program. Computers and Geosciences, v.16, no.4, p395-440

Goodway, W. N., Chen, T., and Downton, J., 1997, Improved AVO fluid detection and lithology discrimination using Lamé petrophysical parameters; "LambdaRho", " MuRho" and "Lambda/Mu fluid stack," from P and S inversions: 67th Annual International Meeting, SEG, Expanded Abstracts, 183–186.

Goovaerts, P., 1997, Geostatistics for Natural Resources Exploration. Oxford University Press, New York.

Gomes, C. J. S., Filho, A. D., Posada, A. M. A., and Da Silva, A. C., 2010, The role of backstop shape during inversion tectonics physical models: Annals of the Brazilian Academy of Sciences, 82(4): 997-1012.

Görür, N., 1988, Timing of opening of the Black Sea Basin: Tectonophysics, v. 147, p. 247–262.

Görür, N., Tüysüz, O., Aykol, A., Sakinç, M., Yiğitbaş, E., and Akkök, R., 1993, Cretaceous red pelagic carbonates of northern Turkey: their place in the opening history of the Black Sea: Eclogae Geologicae Helvetiae, v. 86/3, p. 819–838.

Görür, N., and Tüysüz, O., 1997, Petroleum geology of the southern continental margin of the Black Sea, in A.G. Robinson, ed., Regional and petroleum geology of the Black Sea and surrounding region: AAPG Memoir 68, p. 241–254.

Görür, N., 1997, Cretaceous syn- to postrift sedimentation on the southern continental margin of the Western Black Sea Basin, in A.G. Robinson, ed., Regional and petroleum geology of the Black Sea and surrounding region: AAPG Memoir 68, p. 227–240.

Greenberg, M. L., and Castagna, J. P., 1992, Shear-wave velocity estimation in porous rocks: Theoretical formulation, preliminary verification and applications: Geophys. Prosp., 40, 195–209.

Hampson, D., Russell, B., and Bankhead, B., 2005, Simultaneous inversion of pre-stack seismic data: Ann. Mtg. Abstracts, Society of Exploration Geophysicists.

Hampson-Russell version 10.4, Software CGG, 2015, available at http://www.cgg.com/hampson-russell.aspx?cid=3609&lang=1

Heezen, B. C., Ewing, M. H., 1952, Turbidity currents and submarine slumps, and the 1929 Grand Banks earthquake. Amer. J. Sci., 250, 849–873.

Isaaks, E. H. 1984, Indicator simulation: application to the simulation of a high grade mineralisation. Geostatistic for natural resources, Part2, D. Reidel Publishing Company, 1057-1069.

Journel, A. G., 1983, Nonparametric estimation of spatial distributions, Mathematical Geology, 15(3) p445-468

Journel, A. G., Xu, W., and Tran, T., 1992, Integrating seismic data in reservoir modeling: The collocated cokriging alternative: Stanford Center for Reservoir Forecasting 1992 Report.

Koefoed, O., 1955, On the effect of Poisson's ratios of rock strata on the reflection coefficients of plane waves: Geophys. Prosp., 3, 381-387.

Krige, D. G., 1951, A statistical approach to some basic mine valuation problems on the Witwatersrand. Journal of the Chem., Metal and Mining Soc. of South Africa 52 (6): 119-139.

Kuenen, Ph. D., Migliorini, C. I., 1950, Turbidity currents as a cause of graded bedding. J. Geol., 58, 91–127.

Lantuejoul, C., 2002, Conditional simulation of spatial stochastic models. Retrieved on 14th March 2006 from http://www.cmis.csiro.au/ismm2002/proceedings/PDF/29 lantuejoul.pdf.

Letouzey, J., Biju-Duval, B., Dorkel, A., Gonnard, R., Kristchev, K., Montadert, L., and Sungurlu, O., 1977, The Black Sea: a marginal basin; geophysical and geological data, in B. Biju-Duval and L. Montadert, eds., International symposium on the structural history of the Mediterranean basins: Paris, Editions Technip, p. 363–376.

Li, W., and Zhang, C., 2007, Comparing a fixed-path markov chain geostatistical algorithm with sequential indicator simulation in categorical variable simulation from regular samples. Web of Science, 44(3) 251-266

Lindseth, R. O., 1979, Synthetic sonic logs - A process of stratigraphic interpretation, in Lines, L. R., Ed., Inversion of geophysical data: Soc. of Expl. Geophys., 195-218. (* Reprinted from Geophysics, 44, 3-26).

Lloyd, C. D., and Atkinson, P. M., 2001, Assessing uncertainty in estimates with ordinary and indicator kriging. Computers and Geosciences, 27(8), 929-937.

Lucet, N., and Mavko, G., 1991, Rock properties interpretation of a cross-well seismic image: Stanford Seismic Tomography Project 1991 Report.

Manetti, P., Peccerillo, A., Poli, G., and Corsini, F., 1983, Petrochemical constraints on the models of Cretaceous–Eocene tectonic evolution of the EasternPontide chain (Turkey): Cretaceous Research,v. 4, p. 159–172.

Mavko, G., Mukerji, T., and Dvorkin, J., 1998, The rock physics handbook: Tools for seismic analysis in porous media: Cambridge Univ. Press.

Mitchum Jr. R. M., 1985, Seismic stratigraphic expression of sub-marine fans. American Association of Petroleum Geologists Memoir, 39, 117-136.

Mitchum Jr. R. M., Vail, P.R. and Thompson, S., 1977, Seismic Stratigraphy and Global Changes of Sea Level: Part 11. Glossary of terms used in seismic stratigraphy: Section 2. Application of seismic reflection configuration to stratigraphic interpretation: American Association of Petroleum Geologists Memoir 26, p. 205-212.

Munteanu, I., Matenco, L., Dinu, C., Cloetingh, S., 2011, Kinematics of back-arc inversion of the Western Black Sea Basin. Tectonics 30 (5), TC5004.

Munteanu, I., Willingshofer, E., Sokoutis D., Matenco, L., Dinu, C., and Cloetingh, S., 2013, Transfer of deformation in back-arc basins with a laterally variable

rheology: Constraints from analogue modelling of the Balkanides–Western Black Sea inversion. Tectonophysics 602 (2013) 223–236.

Mutti, E., 1985, Turbidite systems and their relations to depositional sequences. In: G.G. Zuffa (Ed.), Provenance of Arenites, Reidel, Dordrecht, pp. 65–93.

Mutti, E., Ricci Lucchi, F., 1972, Le torbiditi de Appennino settenrionale: introduzioni all'analisi de facies. Memorie della Societa Geologia Italiana, 11, 161–199.

Mutti, E., Bernoulli, D., Ricci Lucchi, F., and Tinterri, R., 2009, Turbidites and turbidity currents from Alpine 'flysch' to the exploration of continental margins. Sedimentology, 56, 267–318.

Nikishin, A. M., Korotaev, M. V., Ershov, A. V., and Brunet, M. F., 2003, The Black Sea basin: tectonic history and NeogeneeQuaternary rapid subsidence modeling. Sedimentary Geology 156 (9), 119e148.

Normark, W. R., 1970, Growth patterns of deep-sea fans. AAPG Bull., 54, 2170–2195.

Normark, W. R., 1978, Fan valleys, channels, and depositional lobes on modern submarine fans: Characters for recognition of sandy turbidite environments. Amer. Assoc. Petrol. Geol. Bull., 62, 912–931.

Okay, A. I., Şengör, A. M. C., Görür, N., 1994. Kinematic history of the opening of the Black Sea and its effect on the surrounding regions. Geology 22, 267e270.

Pickett, G. R., 1963, Acoustic character logs and their application in formation evaluation: J. Petr. Tech., 15, 659-667.

Reuss, A., 1929, Berechnung der fliessgrense von mischkristallen auf grund der plastizitatbedingung fur einkristalle: Zeitschrift fur Angewandte Mathematik aus Mechnik, 9, 49–58.

Robinson, A. G., 1997, Introduction: tectonic elements of the Black Sea Region, in A.G. Robinson, ed., Regional and petroleum geology of the Black Sea and surrounding region: AAPG Memoir 68, p. 1–6.

Ross, D. A., Uchupi, E., Prada, K. E., and MacIlvaine, J. C., 1974, Bathymetry and microtopography of Black Sea, in D.A. Ross and E.T. Egens, eds., The Black Sea—geology, chemistry, and biology: AAPG Memoir 20, p. 1–10.

Russell, B., and Hampson, D., 1991, A comparison of post-stack seismic inversion methods: Ann. Mtg. Abstracts, Society of Exploration Geophysicists, 876-878.

Russell, B. H., Gray, D., and Hampson, D. P., 2011, Linearized AVO and poroelasticity: Geophysics, 76, C19-C29.

Rutherford, S. R., and Williams, R. H., 1989, Amplitude-versus offset variations in gas sands: Geophysics, 54, 680--688.

Sarg, J. F., and Skjold, L. J., 1982, Stratigraphic traps in Paleocene sands in the Balder area, North Sea. American Association of Petroleum Geologists Memoir, 32, 197-206.

Smith, G. C. and Gidlow, P. M., 1987, weighted stacking for rock property estimation and detection of gas: Geophys. Prosp., 35, no. 09, 993-1014.

Smith, G. C., and Gidlow, P. M., 2000, A comparison of the fluid factor with lambda and mu in AVO analysis: 70th Annual International Meeting, SEG, Expanded Abstracts, 122–125.

Shanmugam, G., 2000, 50 years of the turbidite paradigm (1950s-1990s): deep-water processes and facies models - a critical perspective

Sheriff, R. E., 2002, Encyclopedic dictionary of applied geophysics. IV. Edition. SEG, 429 p.

Slatt, R. M., 2006, Stratigraphic Reservoir Characterization For Petroleum Geologists, Geophysicists, And Engineers. Elsevier.

Spadini, G., Robinson, A. G., and Cloetingh, S. A. P. L., 1997, Thermomechanical modeling of Black Sea Basin formation, subsidence, and sedimentation, in A.G. Robinson, ed., Regional and petroleum geology of the Black Sea and surrounding region: AAPG Memoir 68, p. 19–38.

Srivastava, R. M., 1994, Thoughts and comments on conditional simulation algorithms. Geostatistics, V.7, no. 2, p9-10.

Stephenson, R. A., Marty, Y., Okay, A., Roberson, A. H. F., Saintot, A., Stovba, S., and Khriachtchevskaia, O., 2004, TRANSMED section VIII; East-European Craton–Crimea– Black Sea–Anatolia–Cyprus–Levant Sea–Sinai–Red Sea. In: Cavazza, W., Roure, F., Spakman, W., Stampfli, G.M., Ziegler, P.A. (Eds.), The TRANSMED Atlas: The Mediterranean Region from Crust to Mantle. Springer, Berlin.

Stuart, C. J., Nemcok, M., Vangelov, D., Higgins, E. R., Welker, C., and Meaux, D., 2011, Structural and depositional evolution of the East Balkan thrust belt, Bulgaria. AAPG Bulletin 95 (4), 649–673.

Torskaya, T., Jin, G., and Torres-Verdin, C., 2007, Pore-Level Analysis of the Relationship Between Porosity, Irreducible Water Saturation, and Permeability of Clastic Rocks. SPE Annual Technical Conference and Exhibition held in Anaheim, California, USA., 11-14 November 2007.

Tatham, R. H., 1982, Vp=Vs and lithology: Geophysics, 47, 336–344.

Tonn, R., 1992, Statistical approach to correlate reservoir parameters and 3-D seismic attributes: 1992 SEG Annual Meeting Expanded Abstract, pp 272-274.

Vann, J., Bertoli, O., and Jackson, S., 2002, An Overview of Geostastical Simulation for Quantifying Risk. Paper published at a Geostatistical Association of Australasia symposium "Quantifying Risk and Error". March 2002.

Voigt, W., 1928, Lehrbuch der Kristallphysik: Teubner.

Walker, R. G., 1978, Deep-water sandstone facies and ancient submarine fans: Models for exploration for stratigraphic traps. Amer. Assoc. Petrol. Geol. Bull., 62, 932–966.

Walker, R. G., 1992, Facies, facies models, and modern stratigraphic concepts. In: R.G. Walker, N.P. James, Response to Sea Level Change, Geol. Assoc. Can., pp. 1–14.

Yılmaz, Y., Tuysuz, O., Yiğitbaş, E., Genç, Ş. G., and Şengör, A. M. C., 1997, Geology and tectonic evolution of the Pontides, in A.G. Robinson, ed., Regional and petroleum geology of the Black Sea and surrounding region: AAPG Memoir 68, p. 183.226.

Ziolkowsk, A., Underhill, J. R., and Johnston, R. G. K., 1998, Wavelets, well ties, and the search for subtle stratigraphic traps, Geophysics, Vol. 63, No. 1; P. 297–313.

Zoeppritz, K., 1919, Erdbebenwellen VIII B, Über die Reflexion and Durchgang seismischer Wellen durch Unstetigkeitsflächen: Gottinger Nachr, 1, 66-84.

Zonenshain, L. P., and LePichon, X., 1986, Deep basins of the Black Sea and Caspian Sea as remnants of Mesozoic back-arc basins: Tectonophysics, v. 123, p. 181–212.

Zong, Z., Yin, X., and Wu, G., 2012, AVO inversion and poroelasticity with P- and S-wave moduli: Geophysics, 77, N29-N36.

VITA

SUAT AKTEPE
Address :
Work Phone :
Cell Phone :
Email :

EDUCATION

Doctor of Philosophy
Department of Geological Engineering, Middle East Technical University, Turkey, June, 2015.

Master of Science
Department of Geosciences, University of Houston, USA, August 2007.

Language Education
English education at University of Texas at Austin, USA, 2005.

Bachelor of Science
Ankara University, Department of Geophysical Engineering,
Turkey, June, 2002.

WORK EXPERIENCE

06/2010 - Present
Turkish Petroleum Corp. (TPAO), Project Geophysicist
06/2014 – 07/2014
Shell, Project Geophysicist as a secondee.
10/2007 – 06/2010
Turkish Petroleum Corp. (TPAO), Geophysicist, Seismic data processing.
0**5/2006 – 10/2007**
PGS, Geophysicist. Seismic data processing
07/2002 – 08/2002
Turkish Petroleum Corp. (TPAO), Intern Geophysicist.

PUBLICATIONS

Aktepe, S., Depth Imaging of Basement Control of Shallow Deformation; Application to Fort Worth Basin and Teapot Dome Data Sets. University of Houston, M.Sc. Thesis, 2007.

Aktepe, S., Marfurt, K.J. Imaging of basement control of shallow deformation: Application to Forth Worth Basin. SEG Expanded Abstracts 26, 2432 (2007).

Aktepe, S., Marfurt, K.J. Attribute expression of basement faulting: Time versus depth migration. The Leading Edge 27, 360 (2008).

Sipahioğlu, Ö., Korucu, Ö., **Aktepe, S**., Bengü, E. Westerly-sourced Late Oligocene-Middle Miocene axial sediment dispersal system in Turkish Western Black Sea: myth or reality? 19th International Petroleum and Natural Gas Congress and Exhibition of Turkey, Ankara, 15-17 May 2013.

Korucu, Ö., Sipahioğlu, Ö., **Aktepe, S**., Bengü, E. Correlation of Neogene sequence in western-central part of Turkish Black Sea based on ultra-deep well data. 19th International Petroleum and Natural Gas Congress and Exhibition of Turkey, Ankara, 15-17 May 2013.

Aktepe, S., Korucu, Ö., Sipahioğlu, Ö., Bengü, E. How much can we learn from 1D seismic forward model? An Example of Turkish Western Black Sea. 19th International Petroleum and Natural Gas Congress and Exhibition of Turkey, Ankara, 15-17 May 2013.

Aktepe, S., Korucu, Ö., Sipahioğlu, Ö., Bengü, E. Seismic Forward Modeling of Late Oligocene Submarine Fan Complexes in Turkish Western Black Sea. AAPG, Petroleum systems of the Paratethys Exploring the Pathway from Europe to Asia, Georgia, Tbilisi, 26-27 September 2013.

Sipahioğlu, Ö., Korucu, Ö., **Aktepe, S**., Bengü, E. The late Oligocene-Middle Miocene Sediment Fairway in Turkish Western Black Sea. AAPG, Petroleum systems of the Paratethys Exploring the Pathway from Europe to Asia, Georgia, Tbilisi, 26-27 September 2013.

HONORS AND ACTIVITIES

- Offering a course to the summer interns.
- The member of TPAO's Scholarship Advising Committee (2013-Present).
- The congress executive committee member at "The 19th International Geophysical Congress and Exhibition of Turkey", 23-26 November 2010.
- Full scholarship for graduate education in the U.S awarded by Turkish Petroleum Company, and Turkish Government, 2004-2007.

PROFESSIONAL AFFILIATIONS

- Society of Exploration Geophysicists.
- Chamber of Geophysical Engineers of Turkey.
- Turkish Association of Petroleum Geologists.
- Turkish Association of Petroleum Geophysicist.